University of Alberta

Determination of Near-Surface Variability Using Rayleigh Waves

by

Kristen Beaty ©

A thesis submitted to the Faculty of Graduate Studies and Research in partial fulfillment of the requirements for the degree of Master of Science

in

Geophysics

Department of Physics

Edmonton, Alberta

Fall 2000

National Library of Canada
Acquisitions and Bibliographic Services
395 Wellington Street
Ottawa ON K1A 0N4
Canada

Bibliothèque nationale du Canada
Acquisitions et services bibliographiques
395, rue Wellington
Ottawa ON K1A 0N4
Canada

Your file Votre référence

Our file Notre référence

The author has granted a non-exclusive licence allowing the National Library of Canada to reproduce, loan, distribute or sell copies of this thesis in microform, paper or electronic formats.

L'auteur a accordé une licence non exclusive permettant à la Bibliothèque nationale du Canada de reproduire, prêter, distribuer ou vendre des copies de cette thèse sous la forme de microfiche/film, de reproduction sur papier ou sur format électronique.

The author retains ownership of the copyright in this thesis. Neither the thesis nor substantial extracts from it may be printed or otherwise reproduced without the author's permission.

L'auteur conserve la propriété du droit d'auteur qui protège cette thèse. Ni la thèse ni des extraits substantiels de celle-ci ne doivent être imprimés ou autrement reproduits sans son autorisation.

0-612-59778-4

Canada

University of Alberta

Library Release Form

NAME OF AUTHOR:	Kristen Beaty
TITLE OF THESIS:	Determination of Near-Surface Variability Using Rayleigh Waves
DEGREE:	Master of Science
YEAR THIS DEGREE GRANTED:	2000

Permission is hereby granted to the University of Alberta Library to reproduce single copies of this thesis and to lend or sell such copies for private, scholarly or scientific research purposes only.

The author reserves all other publication and other rights in association with the copyright in the thesis, and except as hereinbefore provided neither the thesis nor any substantial portion thereof may be printed or otherwise reproduced in any material form whatever without the author's prior written permission.

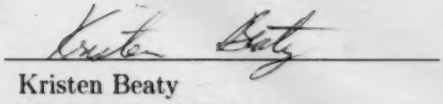

Kristen Beaty
Department of Physics
University of Alberta
Edmonton, Alberta
T6G 2J1

August 22, 2000

Abstract

Rayleigh wave dispersion was used to examine seasonal variability of the near-surface (up to approximately 15 m depth) elastic properties. Seismic surface waves were generated using a sledgehammer source and collected using an array of three-component geophones at 0.5 m spacing with offsets ranging from 7 to 38 m. Multiple data sets were obtained at the Edmonton Research Station over the course of the summer and early fall of 1999 at 2 to 3 week intervals. Dispersion analysis of the vertical component data indicates that there are three strong Rayleigh modes present, the phase velocities of which change very little between survey dates. There are, however, indications that the attenuation properties of the top 1 to 2 m do change over the study period. Inversion of the three Rayleigh mode dispersion curves using a fast simulated annealing algorithm (Sen and Stoffa, 1995) coupled with a matrix propagator forward modelling technique (Menke, 1979) yields *S*-wave velocity profiles that agree well with geological information and vertical seismic profile results. Resolution of the inverted velocity profiles is excellent down to a depth of about 8 m after which the uncertainty increases.

University of Alberta

Faculty of Graduate Studies and Research

The undersigned certify that they have read, and recommend to the Faculty of Graduate Studies and Research for acceptance, a thesis entitled **Determination of Near-Surface Variability Using Rayleigh Waves** submitted by **Kristen Beaty** in partial fulfillment of the requirements for the degree of Master of Science in Geophysics.

Dr. D. Schmitt (Supervisor)

Dr. B. Sutherland (External)

Dr. M. Sacchi

Dr. F. Hegmann

DATE: August 23, 2000

To

my parents, Ken and Marlene Beaty, who encouraged me in my education.

Preface

It was the hope of Dobrin (1951) that seismic surface waves might one day be made a "useful by-product rather than a waste product of seismic exploration". Advances in computational physics and theoretical seismology have made the use of surface wave dispersion for exploration purposes increasingly attractive. In earthquake seismology, surface wave dispersion continues to be used as a tool to map out elastic properties of the crust and upper mantle. Techniques originally developed for earthquake seismology applications have been adapted and improved for shallow exploration projects. The use of seismic techniques including surface wave dispersion for studying near-surface environmental and geotechnical engineering problems is becoming increasingly common but there is a deficit of information on the seismic properties of near-surface materials. Part of the reason for this is that laboratory studies on unconsolidated materials are extremely difficult to perform. The aim of this study is to use surface wave dispersion as a technique to determine the seasonal variability of the seismic properties of the near-surface and to improve the understanding of the role that near-surface materials play in seismic wave propagation.

Acknowledgements

I would like to thank Dr. Schmitt for supervising me and Dr. Sacchi who provided many useful explanations of signal processing and inversion techniques I encountered. This work was sponsored by NSERC and the Seismic Heavy Oil Consortium (SHOC) and I would also like to acknowledge the support of an NSERC PGS-A scholarship. Technicians Len Tober and Michael Lazorek aided in data acquisition as did numerous post doctoral, graduate and undergraduate students - Rik Brooymans, Saeed Jafarian-Oshtbin, Kevin Fox, Ulrich Theune, Christine Ryder and Uli Zimmer. I would also like to thank Dr. M. Heimpel and Dr. J.M. Maillol for assistance in performing a DC resistivity survey and Dr. Yinbin Liu for many helpful discussions on matrix propagator techniques. Also, Dr. I. Meglis provided an orientation to the laboratory and help with some ultrasonic measurements that have not been included in this thesis. I would like to thank David Shaw and for help with the occasional mathematical problem and for providing me with the most recent version of the U of A thesis template for LaTeX and Marko Mah for proofreading several sections of my thesis. Last but not least I would like to acknowledge Norm Buchanan for many insightful discussions and for moral support throughout my degree.

Table of Contents

Abstract

Preface

Acknowledgements

Table of Contents

List of Tables

List of Figures

1 Introduction 1

2 Motivation and Background 4

2.1 Motivation and background 4

2.2 Surface waves as an exploration tool 6

2.2.1 Spectral analysis of surface waves (SASW) 8

2.2.2 Multichannel surface wave techniques 10

2.2.3 Surface waves in earthquake seismology 16

2.2.4 Near-surface seasonal variation study 28

3 Experimental Set-up 31

3.1 Frequency limitations of equipment 44
3.2 Trigger test 45

4 Study Site **49**
4.1 Site characterization 51
4.1.1 Soil coring 51
4.1.2 Borehole seismic measurements 55
4.1.3 Seismic refraction analysis 65
4.1.4 DC Resistivity 68
4.1.5 Ground penetrating radar 73

5 Dispersion Analysis **77**
5.1 Obtaining dispersion curves experimentally 77
5.1.1 Phase comparison methods for determining dispersion curves 78
5.1.2 Multi-channel methods for obtaining dispersion curves . . 81
5.1.3 Obtaining the $f-p$ section 86
5.2 Application of multichannel methods to the data 91
5.2.1 Comparison of the windowing methods 92
5.2.2 Comparison of the $f-p$ and $f-k$ methods 95
5.3 Vertical component dispersion analysis 102
5.4 Horizontal component dispersion analysis 113
5.4.1 Longitudinal horizontal component 113
5.4.2 Transverse horizontal component 113
5.5 Seasonal changes in dispersion curves 121

6 Inversion and Interpretation **125**
6.1 Forward modelling and inverse theory 125
6.1.1 Rayleigh waves in a homogeneous half-space 126
6.1.2 Rayleigh waves in a layered medium 130

6.1.3 The inversion of Rayleigh wave dispersion curves 142
6.1.4 Uncertainty estimation 148
6.1.5 Testing the algorithms 151
6.2 Inversion results 155
6.2.1 Synthetic example 157
6.2.2 Inversion of experimental data 158

7 Conclusions **179**

References **184**

Appendices **194**

A Chebyshev Polynomials **194**

B Generating Random Numbers with a Cauchy Distribution **197**

C Code **198**
C.1 Forward modelling code 198
C.2 Simulated annealing algorithm 206
C.3 Chebyshev polynomials 209

List of Tables

3.1 Summary of seismic surveys where 3-C and V indicate that three component geophones or that the 14 Hz vertical geophones were used, respectively. 37

3.2 Summary acquisition parameters where f_{Ny} is the Nyquist frequency. In the case of the May 20 data, the data were zero padded out to 8192 points before decimating in order to simplify processing. 38

3.3 Specifications for geophones used in this study where f is natural frequency, and L is impedance. 46

3.4 Results of the trigger test (June 11, 1999) showing the mean and standard deviation of pick times, in samples, for three different trigger types as compared to the results for the small piezo trigger. 47

4.1 Geology of the study site as determined from core samples. . . . 54

4.2 Acquisition parameters for the GPR survey. 73

List of Figures

2.1 Identically scaled seismic records obtained under varying soil moisture conditions at a site near Lawrence, Kansas. The water content values given are the average values found from samples taken from the top 0.15 m of the subsurface expressed in terms of % water content by mass (after Jefferson et al., 1998). 6

2.2 Schematic of the particle motion of a Love wave (after Bolt, 1976). 7

2.3 Composite profile at a flexible pavement site found using SASW (after Nazarian and Stokoe, 1986). 9

2.4 Comparison of inversion results to true profile for a synthetic example; a) Profiles at different stages of inversion; b) Associated theoretical dispersion curves (after Ganji et al., 1998). 11

2.5 Time-offset record for 288 traces from vertical geophones spaced 1 m apart (offset: 40-327 m). Traces have been corrected for geometrical spreading and field amplification. The fundamental mode (sometimes referred to as the primary mode) Rayleigh wave, marked on the seismogram, are propagating at a slower velocity than the higher modes (after Gabriels et al., 1987). 12

2.6 Display of $f - k$ amplitude spectrum for 256 traces with offsets of 72-327 m. The superimposed curves represent the dispersion curves calculated for the final shear-wave velocity profile obtained from these data (after Gabriels et al., 1987). 13

2.7 Example of the wavefield decomposition technique used by Park et al. (1998). Three Rayleigh wave modes are imaged clearly as coherent dark bands. The fundamental mode appears at th lowest frequencies and the second and third modes can be seen starting at slightly higher frequencies. For a given frequency, each mode has a progressively higher phase velocity starting from the fundamental mode (after Park et al., 1998). 14

2.8 Inversion results carried out on real MASW dispersion curve data starting from two different initial models. Initial model B was chosen using the simple inversion algorithm while A was chosen to be uniformly greater than borehole measurements. a) Dispersion curves for the various velocity models along with the measured dispersion curve; b) S-wave velocity models used as initial values in the inversion, resulting from inversion of the dispersion data and determined from borehole measurements (after Xia et al., 1999b). 17

2.9 The final model for the shear-wave velocity profile obtained from the surface wave data in figure 2.5 (solid line) with its standard deviation (dashed line) (after Gabriels et al., 1987). 18

2.10 Inverted S-wave velocities and borehole measurements taken at four different locations in the Fraser River Delta. For d) no borehole information is available (after Xia al., 1999a). 18

2.11 Observed composite-path Love wave data and the extracted pure-path dispersion curves (after Toksöz and Anderson, 1966). 20

2.12 Shear velocity distributions for the CIT-11 (New Guinea-Pasadena path) and CIT-12 (Mongolia-Pasadena path) models (after Toksöz and Anderson, 1966). 21

2.13 Rayleigh wave dispersion curve for the CIT-12 mixed-path model and the observed data over Mongolia and Assam-Pasadena paths which are quite close together (after Toksöz and Anderson, 1966). 22

2.14 Phase velocity maps for Love (left) and Rayleigh waves (right) at 5,10 and 15 mHz. These maps show percentage phase velocity perturbation after the mean has been taken out. The amplitudes in the maps increase with frequency but never exceeds 7%. The white dots mark hotspot locations (after Laske and Masters, 1996). . . 23

2.15 Idealized diagram illustrating the preferred model for the oceanic upper mantle in the Pacific. The upper mantle appears to be transversely isotropic if averaging over a number of azimuthal paths is performed. This averages out any azimuthal velocity dependence. The amplitude of the transverse isotropic effect under the mid-ocean ridge system is expected to be low due to the contribution of both horizontal and vertical flow in this region (after Nishimura and Forsyth, 1989). 24

2.16 Transversely isotropic upper mantle structure found from Rayleigh wave and Love wave dispersion curves. The two parameters shown, β_V and $\xi = (\beta_V/\beta_H)^2$ which represent the S-wave velocity in the vertical direction and the shear wave anisotropy term respectively, are the parameters that could be resolved the most reliably from the data (after Nishimura and Forsyth, 1989). 25

2.17 a) Great circle paths crossing the MELT study area. The white line marks the spreading center while the locations of ocean bottom 3 component seismograms are marked by open triangles and pressure readings by open circles. At a period of 25 s, 703 paths from 23 earthquakes to 39 stations were used in the tomographic inversion (Forsyth et al., 1998); b) Bathymetry of the MELT study area with symbols for seismometers the same as in a) and seismometers that returned no data marked as inverted, filled triangles. The arrays were oriented at an angle to the ridge such that they would lie along the great-circle path that includes the seismically active regions bordering the southwest Pacific (The MELT Seismic Team, 1998). 29

2.18 Results of tomographic inversions of Rayleigh wave phase velocities at a period of 25 s. Comparison of the two models shows that resolution is poorer near the edges but that there are features closer to the ridge that are imaged by both models. The black bars indicate the direction and degree of azimuthal anisotropy. a) Inversion with a strong smoothing constraint using a starting model that is symmetric about the ridge axis; b) Inversion with a weak minimum length constraint with the same starting model as used in a). (Forsyth et al., 1998). 30

3.1 Simple model of a velocity geophone of the type typically used in seismic exploration. When a seismic wave passes the case and magnet move but the mass suspended from the spring tends to remain stationary. An output voltage is generated proportional to the velocity of the relative motion between the conductor and the magnetic field (Kearney and Brooks, 1995). 33

3.2 Plan view of the layout used for this experiment. Each time the study was repeated, the line was surveyed out using the fire hydrant and the gate posts, which were always in the same position, as reference points. The 3-component geophones were oriented so that the two arrows on the case pointed towards the north and towards the shot point. A bubble on the corner of the case allows the geophones to be levelled. 34

3.3 Seismic recording truck next to the receiver line at the Edmonton Research Station. 35

3.4 Geometry of the survey performed at the Edmonton Research Station indicating the geophone locations used in the surface wave analysis (not to scale). A sledge hammer source was used. The solid line illustrated the propagation of a surface wave. The equilibrium position of the free surface is indicated by the dotted line. 35

3.5 Vibroseis field data acquired by Park et al. (1999b). The first trace in each seismogram represents the sweep used. The data in a) show coherency in the ground roll indicating good data quality (minimum offset 27 m). The seismogram in b) demonstrates near-field effects which can be identified by the reduced coherency and fragmentation of the energy packets (minimum offset 1.8 m). In c) the far-offset effects are identifiable by the decrease in ground roll slope (increase in apparent phase velocity) for the same frequencies at closer offsets (not shown) and by the reduced coherency (after Park et al., 1999b). 36

3.6 Stacked data recorded on September 9, 1999, vertical component. 40

3.7 Stacked data recorded on September 9, 1999, horizontal transverse (HT) component. 41

3.8 Stacked data recorded on September 9, 1999, horizontal longitudinal (HL) component. 42

3.9 This figure shows the different types of waves found in a typical seismic shot gather. 43

3.10 Phase (top) and amplitude (bottom) response of the OYO data acquisition system for a sampling rate of 2 ms (private communication, OYO Instruments, Inc., 9777 Gulf Bank Suite 10, Houston, Texas 77040). The low frequency response is due to the 3 Hz low-cut analog filter and the high frequency response is due to a digital anti-aliasing filter that is applied before storing the data. 45

3.11 Results of the trigger test. Top - surface wave first break picks for each trace (three records per trigger type, one shot per record); bottom - difference between picks, in number of samples, with the results from the small piezo trigger used as a baseline. Mean values are displayed as flat lines. The legend applies to both plots where O.I. stands for 'optical isolater'. 48

4.1 Aerial photograph of the University of Alberta Edmonton Research Station (courtesy of the Department of Agriculture, University of Alberta). This experiment was carried out on the west side of the farm, as marked. 50

4.2 An auger drill rig was used to obtain soil cores at the University of Alberta Edmonton Research Station (drilling done by Mobil Augers). 52

4.3 A soil core taken using a split spoon sampler. 53

4.4 Soil moisture content and bulk density measurements from a soil core obtained on October 6, 1999. 55

4.5 Geometry of the VSP survey performed at the Edmonton Research Station. A sledge hammer impacting on an aluminum plate was used as a source. 56

4.6 Component H1 of October 6, 1999 VSP survey at the Edmonton Research Station. *P*-wave picks are marked by circles and *S*-wave picks by triangles. 58

4.7 Component H2 of October 6, 1999 VSP survey at the Edmonton Research Station. Coherent *P*- and *S*-wave arrivals are much harder to pick out indicating that the majority of the horizontally propagating energy has been recorded on component H1. 59

4.8 Vertical component of October 6, 1999 VSP survey at the Edmonton Research Station. Low frequency noise dominates the seismogram. 60

4.9 Regression analysis of the P- (top) and *S*-wave (bottom) first break picks from the October 6, 1999 VSP, component H1. . . . 61

4.10 Inversion analysis (solid line) of the *P*- (left) and *S*-wave (right) first break picks from the October 6, 1999 VSP, component H1. The results from regression analysis on the VSP data are represented by the dotted lines. 63

4.11 A comparison of traveltime picks with those estimated from the inversion results. 64

4.12 Refraction analysis on vertical component of September 9, 1999 data. The picks represent the onset of first energy. 66

4.13 Comparison of *P*-wave velocities as determined by the VSP survey using regression analysis and inversion with those found by refraction analysis. 67

4.14 Apparent resistivity versus half the distance between outer electrodes for a Schlumberger DC resistivity survey carried out at the of Edmonton Research Station on August 23, 1999. 70

4.15 Top - a plot of apparent resistivity versus AB/2 showing data gathered August 23, 1999 and a model that fits very well. The resistivity depth profile used to generate this model is shown in the lower plot. 72

4.16 Processed GPR data obtained May 5, 2000 at the Edmonton Research Station. The top and bottom images show data obtained using the 25 MHz and 50 MHz antennae, respectively. 75

4.17 GPR data obtained May 5, 2000 at the Edmonton Research Station with the time scale converted to depth using a velocity of 0.11 m/ns. The top and bottom images show data obtained using the 25 MHz and 50 MHz antennae, respectively. Both use the same depth scale. 76

5.1 Seismograms (top) showing the Rayleigh wave, fundamental mode, for the Charter Towers-Adelaide path (epicentral distances of 8513 km and 10319 km, respectively) generated by the Rat Island event (21:44:17.2 GMT on 29 April 1963). Phase velocities calculated from the phase difference and cross-correlogram methods are shown (bottom). The dashed line represents a reference level (after Dziewonski et al., 1968). 83

5.2 a) A slant-stack of a set of marine surface wave data is transformed into a $p-\omega$ images by taking the Fourier transform along the τ direction of the $\tau-p$ section. The locus of maximum amplitude in b) provides an estimate of the dispersion curve for the fundamental mode present in the data. Higher modes were not observed in this data set (after McMechan and Yedlin, 1981). 84

5.3 Figure comparing the phase velocity versus frequency representations of the same Rayleigh wave dataset using a) frequency domain methods and b) determination of the $\tau-p$ transform in the time domain. Note that interpolation has been performed to transform the data from representation in slowness to phase velocity (after Park et al., 1998). 85

5.4 An arrival of constant velocity in the offset versus time domain will map onto a point in the $\tau-p$ domain given by its slope and zero offset intercept time. 87

5.5 Closeup of $\tau-p$ data of a single frequency showing all of the possible directions of constructive summing within the range of offsets in the data (slopes in the $\tau-p$ domain) indicated by the shaded area. The $\tau-p$ section in a) has a spacing in p that would result in an aliased reconstruction of the data whereas b) has only one constructive summing direction (x_2) available and would result in the correct reconstruction of the data (after Turner, 1990). . . 90

5.6 Typical $f-p$ section showing three Rayleigh wave modes. 91

5.7 $F-k$ representation of data obtained September 9, 1999 before any windowing has been carried out. The brightest mode on the image is the fundamental Rayleigh wave mode. 93

5.8 Dispersion curves obtained from data windowed in the $f-k$ domain taken at various times between May and September, 1999. Only the fundamental mode is shown. 95

5.9 Dispersion curves obtained from data that were windowed in the time domain taken at various times between May and September, 1999. Only the fundamental mode is shown. 96

5.10 Seismic data showing strong surface waves (vertical component of the September 9, 1999 data set). Receiver spacing is 0.5 m and the minimum offset displayed is 7 m. The data have been windowed in the time domain to include only surface wave arrivals. 97

5.11 The time window applied to the September 9 data set (figure 5.10) shown in the offset-time domain (top) as well as in the Fourier domain (bottom). In the top panel, amplitudes range from 0 (white) to 1 (black). The windowing will have very little effect on the data in the frequency range of interest (about 10 to 75 Hz). 98

5.12 Average power spectrum of surface waves recorded September 9, 1999. 99

5.13 a) Seismic data recorded September 9, 1999 windowed in the time domain showing strong surface waves arrivals (vertical component). Receiver spacing is 0.5 m and the minimum offset displayed is 7 m. b) Slant stack of data. c) Map of frequency versus slowness where the dark peaks correspond to Rayleigh wave dispersion curves. d) Reconstruction of the data in the offset-time domain from the slant-stack representation. 100

5.14 $F-k$ representation of data obtained September 9, 1999 which was first windowed in the time domain. Three distinct Rayleigh modes can be seen. 101

5.15 Dispersion curves obtained from surface wave data using the slant stack method on data windowed in the time domain (triangles connected with a solid line), and using the *f-k* method on data windowed in the time domain (circles connected with a dotted line). The fundamental mode is the lower-most, followed by the second and third modes having greater phase velocities. 105

5.16 Frequency versus slowness sections for vertical component data (10 Hz geophones). 106

5.17 Frequency versus slowness sections for vertical component data (10 Hz geophones). In some cases, for example the May 20 fundamental mode, dispersion curve picks may have been influenced by artifacts in the image. 107

5.18 Frequency versus slowness sections for vertical component data (14 Hz geophones). Again there are a few cases, for example the third mode in the Aug. 27 section, where the dispersion curve picks may have been influenced by artifacts in the image or by proximity to another mode (second and third modes from Sept. 9 section). 108

5.19 Phase velocity dispersion curves for Rayleigh waves recorded at the Edmonton Research Station (vertical component of 3-component 10 Hz geophones). Only the fundamental mode is shown. 109

5.20 Phase velocity dispersion curves for Rayleigh waves recorded at the Edmonton Research Station (vertical component of 3-component 10 Hz geophones). All modes that were distinguishable in the data are shown. 110

5.21 Phase velocity dispersion curves for Rayleigh waves recorded at the Edmonton Research Station (vertical 14 Hz geophones). All modes that were distinguishable in the data are shown. 111

5.22 Phase velocity dispersion curves for Rayleigh waves recorded at the Edmonton Research Station (vertical component) showing data recorded on the same dates by both the 10 Hz and 14 Hz geophones. Survey dates were as follows: top left - June 11, 1999; top right - July 27, 1999; bottom left - August 6, 1999; bottom right - August 27, 1999. 112

5.23 Frequency versus slowness sections for longitudinal horizontal component data (10 Hz geophones). The black line superimposed on the image represent the fundamental mode dispersion curve. . . . 115

5.24 Frequency versus slowness sections for longitudinal horizontal component data (10 Hz geophones). The black line superimposed on the image represent the fundamental mode dispersion curve. . . . 116

5.25 Phase velocity dispersion curves for Rayleigh waves recorded at the Edmonton Research Station (horizontal-longitudinal component of 3-component 10 Hz geophones). Only the fundamental mode is shown. 117

5.26 Frequency versus slowness sections for transverse horizontal component data (10 Hz geophones). The black line superimposed on the image represent the fundamental mode dispersion curve. . . . 118

5.27 Frequency versus slowness sections for transverse horizontal component data (10 Hz geophones). The black line superimposed on the image represent the fundamental mode dispersion curve. . . . 119

5.28 Phase velocity dispersion curves recorded at the Edmonton Research Station (horizontal-transverse component of 3-component 10 Hz geophones). Only the fundamental mode is shown. 120

5.29 Interpolated image of the evolution of the fundamental mode Rayleigh wave dispersion curves with time. Phase velocity is represented by the colour of the image. The phase velocities at frequencies for which there was no dispersion information available have been set to zero for interpolation and display purposes. Note the progressive loss of higher frequency information with time during the summer. 123

5.30 Top - Maximum and minimum daily temperatures; Bottom - Daily precipitation amounts recorded at the Edmonton Research Station. Vertical dotted lines indicate the dates that surface waves were recorded. Dates are labeled according to the first of each month (meteorological data provided by Jeff Thurston, Department of Renewable Resources, University of Alberta, private communication). 124

6.1 Particle motion of a Rayleigh wave with a wavelength of 20 m in an infinite half space for a Poisson solid ($\alpha = \sqrt{3}\beta$; $\lambda = \mu$; $\nu = 0.25$ where ν is Poisson's ratio). Wave propagation is to the right. Particle motion is elliptical with amplitude decreasing exponentially with depth. Asterisks mark displaced particle locations. In all cases the marked particles are moving in the upward direction, resulting in retrograde motion above the dotted line and prograde below. 130

6.2 Diagram showing layered structure with n layers. Layers and interfaces are numbered. Each layer has P- and S-wave velocities (α and β) as well as density (ρ) and thickness (d). 133

6.3 Dispersion function calculated using the matrix method of Menke (1979). White and gray bands represent positive and negative values of the dispersion function, respectively. The black circles, connected by a cubic spline, represent the dispersion curve for the fundamental Rayleigh mode found using the method of Haskell (1953) for the same set of model parameters. 141

6.4 Flow chart of the operations carried out at each temperature for the Metropolis simulated annealing algorithm. 144

6.5 Diagram showing the shape of a Cauchy-like probability distribution for temperatures of 0.1, 1, 10, and 100. 146

6.6 Simple example function defined in equation (6.68) used to test simulated annealing routine. 152

6.7 Misfit curves for 16 simulated annealing inversions of the example function using different random seeds. The starting temperature used was $T_0 = 20$. 153

6.8 Histograms created using the Metropolis SA method for estimating uncertainty. The number of iterations used is shown in the top right corner of each plot. 154

6.9 Mean (solid line) plus or minus one standard deviation (dotted lines) for the inversion results for the example function versus number of iterations of Metropolis SA used in estimating the mean and standard deviation. 155

6.10 The shear-wave velocity profile (solid line) shown in the left panel is the result of an inversion where 21 independent layers were used to represent the profile. The heavy dotted line represents the shear-wave profile used to generate the synthetic data. The dash-dot curve and the dotted lines represent the mean and one standard deviation from the mean, respectively. The *P*-wave (middle) and density (right) profiles were held constant. 164

6.11 Inversion results using 21 independent layers to represent the theoretical shear-wave velocity profile of figure 6.10. White and gray bands represent positive and negative values of the dispersion function, respectively, with roots representing the various modes at the change in colour. The solid lines represent the roots of the dispersion function and the data are plotted as asterisks. The numbers on the image to the left of each mode indicate the mode order. 165

6.12 Theoretical dispersion curves corresponding to the initial model parameters used in the inversions. White and gray bands represent positive and negative values, respectively. The solid lines represent the roots of the dispersion function and the observed dispersion curves are plotted as asterisks. 166

6.13 The *S*-wave velocity (left), *P*-wave velocity (middle) and density (right) profiles used as the initial model in the inversions. 167

6.14 Misfit curve for the inversion performed using 5 Chebyshev polynomials to represent the shear-wave velocity profile. 168

6.15 Inversion results using 5 Chebyshev polynomials to represent the shear-wave velocity profile. White and gray bands represent positive and negative values, respectively. The solid lines represent the roots of the dispersion function and the data are plotted as asterisks. 169

6.16 The shear-wave velocity profile shown in the left panel is the result of an inversion where 5 Chebyshev polynomials were used to represent the profile (solid line). The dash-dot curve and the dotted lines represent the mean and one standard deviation from the mean, respectively, found through the importance sampling technique. The *P*-wave (middle) and density (right) profiles were held constant. 170

6.17 Misfit curve for the inversion performed using 7 Chebyshev polynomials to represent the shear-wave velocity profile and a multiplicative factor to represent the *P*-wave profile. 171

6.18 Inversion results using 7 Chebyshev polynomials to represent the shear-wave velocity profile and a multiplicative factor to represent the *P*-wave profile. White and gray bands represent positive and negative values, respectively. The solid lines represent the roots of the dispersion function and the data are plotted as asterisks. . 172

6.19 The shear-wave velocity profile shown in the left panel is the result of an inversion where 7 Chebyshev polynomials were used to represent the profile. The dash-dot curve and the dotted lines represent the mean and one standard deviation from the mean, respectively, found through the importance sampling technique. The *P*-wave profile (middle) was represented by a multiplicative factor and the density profile (right) was held constant. 173

6.20 Inversion results using 21 independent layers to represent the shear-wave velocity profile. White and gray bands represent positive and negative values, respectively. The solid lines represent the roots of the dispersion function and the data are plotted as asterisks. . 174

6.21 The shear-wave velocity profile shown in the left panel is the result of an inversion where 21 independent layers were used to represent the profile. The dash-dot curve and the dotted lines represent the mean and one standard deviation from the mean, respectively, found through the importance sampling technique. The *P*-wave (middle) and density (right) profiles were held constant. 175

6.22 This figure shows the match of the theoretical data to the observed data when the shear-wave velocities below 8 m were perturbed in order to determine if the low velocity structure shown in figure 6.21 is required to achieve a good fit to the data. Notice that this figure looks virtually identical to figure 6.20. White and gray bands represent positive and negative values, respectively. The solid lines represent the roots of the dispersion function and the observed data are plotted as asterisks. 176

6.23 The shear-wave velocity profile shown in the left panel is the result of an inversion where 21 independent layers were used to represent the profile. The *P*-wave and density profiles were held constant. The shear-wave velocities have been perturbed at depths of greater than 8 m in order to determine if the structure found in this region by the inversion is real. 177

6.24 The shear-wave velocity profile shown in the left panel is the result of an inversion where 21 independent layers were used to represent the profile (previously shown in figure 6.21). The dash-dot curve and the dotted lines represent the mean and one standard deviation from the mean, respectively, found through the importance sampling technique. The profile on the right has the uncertainty analysis performed using only fundamental mode phase velocities above 30 Hz. 178

A.1 Shifted Chebyshev polynomials (type I) with $n = 1$ to 4. 196

Chapter 1

Introduction

Rayleigh waves are surface waves that travel along the earth/air interface. Usually, they are considered useless in reflection and refraction seismology because they contain more energy than body waves and they often arrive in the same time interval as reflections on a seismogram. These waves do, however, contain substantial information on the shear wave velocity structure of the near-surface. Consequently, surface waves are used to study the shallow subsurface, usually for environmental (Miller et al., 1999a; Miller et al., 1999b; Miller et al., 1999c; Long et al., 1999) and geotechnical engineering applications (Stokoe and Nazarian, 1985; Nazarian and Stokoe, 1986).

Rayleigh waves are dispersive in nature; their velocity depends on their frequency. Longer wavelengths (lower frequencies) sample greater depths than shorter wavelengths (higher frequencies). The dispersion curve shows the velocity of the wave at each wavelength. Once obtained, this can be inverted for the shear velocity profile of the area (Xia et al., 1999b; Nazarian and Stokoe, 1986). Incorporation of higher modes improves the accuracy of the inversion process (Tokimatsu et al., 1992).

An experiment was set up to gather seismic surface waves using an array

of three-component geophones at 0.5 m spacing with a sledgehammer source. Multiple data sets were obtained at the University of Alberta experimental farm in Edmonton over the course of the summer and early fall of 1999. The goal of this experiment is to search for trends between seismic variability and changes in the soil conditions during the year. Site characterization, which included a refraction survey, downhole velocity measurements, soil coring, DC resistivity and ground penetrating radar was carried out to obtain independent information about the geophysical and geological characteristics of the site.

Obtaining reliable dispersion curves is a vital step in using surface waves to map out a shear-wave velocity profile. Several different methods for obtaining dispersion curves from Rayleigh waves were examined and compared. One method for obtaining dispersion curves involves first a $\tau - p$ transform on the data followed by a one dimensional Fourier transform along the τ direction (McMechan and Yedlin, 1981). The $\tau - p$ transform essentially involves taking the sum of amplitudes along a line in the offset-time domain with intercept time *tau* and slope (also known as the slowness) p and mapping it onto the point (tau, p). Another method, described by Gabriels et al. (1987), requires picking the peaks associated with surface wave energy in the frequency-wavenumber $(f - k)$ domain. Both methods were applied to the data and compared.

Once reliable dispersion curves have been obtained, they must be inverted to determine the shear-wave velocity profile for the study site and to evaluate the sensitivity of this method to seasonal near-surface changes. A matrix propagator technique (Menke, 1979) was used for forward modelling to obtain theoretical dispersion curves in a layered elastic media. A fast simulated annealing algorithm (Sen and Stoffa, 1995) was used to perform the inversions. The velocity profile was parameterized using Chebyshev polynomials to reduce the number of parameters needed to represent a smooth velocity profile in the inversion.

A better understanding of seismic properties of the near surface will benefit to environmental and geotechnical studies. It is also important for exploration seismology where knowing the effects of the near surface on the seismic waves would make it possible to filter out its effects and obtain an improved image of the deeper subsurface. This research will also help to ensure the validity of time-lapse seismic studies.

Chapter 2

Motivation and Background

2.1 Motivation and background

The conditions of saturation in the near surface of the earth change over the course of the summer and throughout the rest of the year. The soil moisture levels, temperature, compaction, and the water table depth all change. Very little is known about the elastic properties of these near-surface materials and how they evolve as a result of these changes. However, it is crucial that we improve our understanding of the behaviour of seismic waves passing through such materials as such waves have the potential to provide important diagnostic information about saturation and contamination. These factors are crucial to environmental scientists and geotechnical engineers when they must make informed evaluations as to the conditions at a site.

There are actually very few studies of seismic wave propagation in the near surface. There are many reasons for this. Instrumentation, until recently, did not allow detailed high resolution studies. Most applied geophysicists are further focussed on deeper, economic exploration targets and normally consider the weakly consolidated materials near the surface as not much more than a nui-

sance. Finally, the surface waves studied here do not provide detailed structural information. It is important to review what literature there is on near surface seismic studies.

Bachrach and Nur (1998) employed seismic refraction and reflection techniques to monitor the depth of the water table as the tide goes in and out with a maximum depth of investigation of approximately 2 m. This experiment showed that the saturation profile had more of an impact on the seismic profile than the depth of the water table. *P*-wave velocities of as low as 40 m/s were observed.

Jefferson et al. (1998) examined the effects of moisture content on near-surface seismic reflection data. Their results indicated that moisture content has a significant effect on the amplitude and character of the data that is both site and source dependent. A total of 5 surveys were carried out between May and September at a site in Lawrence, Kansas. Moisture content measurements were made at depth intervals between 0.025 m and 0.91 m on each survey date. When the soil in the top 0.15 m was very moist to the point where the liquid limit of the soil had been exceeded, the observed amplitudes were high but the arrivals were ringy in character. Drier soils lead to higher attenuation of the seismic signal. Seismic sections recorded in soils with moderate moisture content tended to show lower attenuation without the ringy character seen in the sections recorded in very moist soils. Figure 2.1 illustrates these effects.

Other in-situ studies of near surface properties have been carried out using vertical or crosshole seismic studies for geotechnical engineering and more recently surface wave dispersion has been employed (Stokoe and Nazarian, 1985; Nazarian and Stokoe, 1986; Gabriels et al., 1987; Park et al., 1999b). Surface wave dispersion is employed in this study to examine the seasonal variability of near-surface seismic properties at the Edmonton Research Station in Edmonton, Alberta.

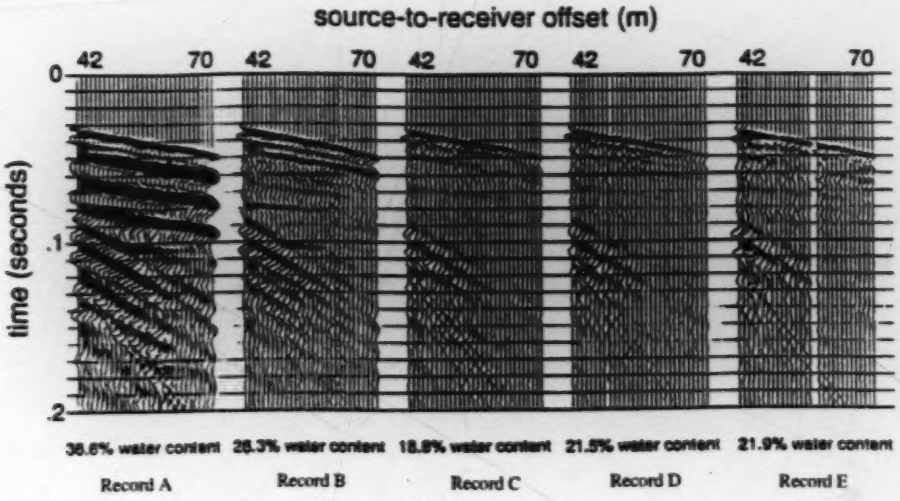

Figure 2.1: Identically scaled seismic records obtained under varying soil moisture conditions at a site near Lawrence, Kansas. The water content values given are the average values found from samples taken from the top 0.15 m of the subsurface expressed in terms of % water content by mass (after Jefferson et al., 1998).

2.2 Surface waves as an exploration tool

There are two kinds of surface waves commonly observed in seismology: Rayleigh waves and Love waves. In the case of Rayleigh waves, the particle motion is confined to the vertical plane containing direction of propagation. Near the surface of a uniform half space, particle motion is elliptical and retrograde. The amplitude drops off exponentially with depth. Rayleigh waves essentially result from the interaction of P-waves (compressional waves, also known as primary waves) and vertically polarized S-waves (transverse waves, also known as secondary or shear waves) with the free surface. Love waves (figure 2.2 (Bolt, 1976)) occur when there is a general increase in S-wave velocity with depth. They propa-

gate by multiple internal reflections of horizontally polarized S-waves (similar to the effect of a waveguide) with particle motion that is transverse and horizontal (Fowler, 1990).

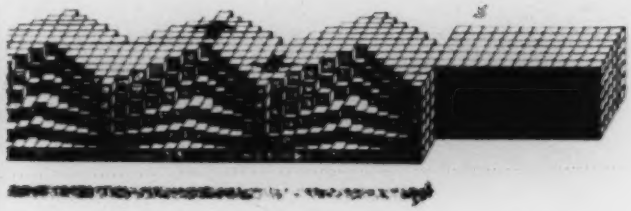

Figure 2.2: Schematic of the particle motion of a Love wave (after Bolt, 1976).

Surface waves are, in general, dispersive meaning that different frequency components of a wave pulse propagate at different velocities. Longer wavelengths contain more information about deeper structure while the shorter wavelengths are confined to a much shallower region. The rule of thumb for Rayleigh waves is that the peak sensitivity is to the shear-wave velocity at a depth of approximately one-third of a wavelength. The penetration depth is on the order of one wavelength. Rayleigh waves are sensitive primarily to shear wave velocity profile but also weakly depend on the density and the compressional wave velocity (Fowler, 1990).

Dispersion curves relate the velocity of the wave at each wavelength or frequency. In principle, the Rayleigh waves over a given layered structure will have a number of branches to the dispersion curve, that is, there can be a number of different velocities for a given frequency. Once obtained these may then be inverted for the shear velocity profile of the area (Xia et al., 1999b; Nazarian and Stokoe, 1986). These multiple branches, or modes, arise because of fortuitous superposition of the various P and SV-waves. This will later be apparent in the solution of the wave equation for the case of Rayleigh waves as an eigenvalue

problem (Aki and Richards, 1980).

2.2.1 Spectral analysis of surface waves (SASW)

Spectral Analysis of Surface Waves (SASW) is a technique developed by the engineering community that uses surface wave dispersion for geotechnical purposes and for nondestructive testing of both flexible (figure 2.3) and rigid pavement (Nazarian and Stokoe, 1986; Nazarian et al., 1983; Nazarian and Stokoe, 1985). This method is attractive because it provides a nondestructive method for estimating the in-situ shear-wave velocities at low cost. The shear modulus is an important parameter used in characterizing the mechanical behaviour of geomaterials under loading and in the evaluation of dynamic soil performance and liquefaction potential during an earthquake (Stokoe et al., 1994; Stokoe and Nazarian, 1985). It is also important for assessing the proper maintenance and rehabilitation of pavement (Ganji et al., 1998). An extensive set of references pertaining to SASW can be found in the annotated bibliography prepared by Hiltunen and Gucunski (1994).

The experimental setup for SASW uses two geophones in most cases, although the use of multiple geophones when possible is recommended by Gucunski and Woods (1991). Each shot is recorded in a common receiver midpoint configuration. Often the experiment is repeated several times, increasing the distance between receivers each time. When multiple receivers are used a common shot configuration is preferred (Gucunski and Woods, 1991).

In pavement studies the depth of investigation is generally about 2.5 m with frequencies of up to 3900 Hz recorded. The use of such high frequencies in principle allows velocities to be determined in an uppermost layer of as little as 2 cm thickness (Nazarian et al., 1983). Studies investigating dynamic soil performance and liquefaction potential are designed with deeper penetration in

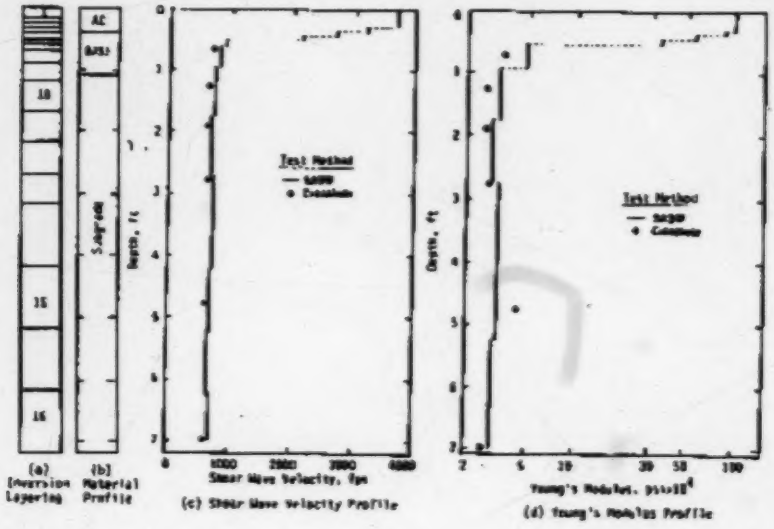

Figure 2.3: Composite profile at a flexible pavement site found using SASW (after Nazarian and Stokoe, 1986).

mind. These types of surveys are often carried out using 4.5 Hz geophones in order to record the low frequencies necessary for deeper investigation (depth of investigation of about 14 m in this case). Several surveys carried out in areas of California where liquefaction had occurred during previous earthquakes showed that in all cases the S-wave velocity of the liquifiable layers was less than 150 m/s (Stokoe and Nazarian, 1985).

A cross-correlation method is used to obtain dispersion curves and forward modelling is generally carried out using various matrix propagator techniques (Thomson, 1950; Haskell, 1953; Knopoff, 1964). Determination of the shear-wave profile has been done by matching forward models to the data manually. In some cases iterative least-squares methods have been used, for example the Newton-Raphson procedure (Rix and Leipski, 1991), to automate the process.

Interactive grid search techniques have also been employed (Nazarian and Stokoe, 1986). Usually only a single apparent dispersion curve is used. Tokimatsu et al. (1992) show that incorporation of higher modes as well as dispersion curves for horizontal particle motion can help to improve the inversion results.

Ganji et al. (1998) describe some recent advances made in inversion of SASW data. They use a linearized stiffness matrix method for forward modelling (Kausel's method) which approximates the elements of a global stiffness matrix (Wolf, 1985; Kausel and Roesset, 1981) using Taylor series up to the second degree (Kausel and Peek, 1982). This method also takes into consideration the source geometry. For the inversion, a linearized method, based on Wiggins (1972), is used in combination with a nonlinear method, the David-Fletcher-Powell technique (McCormick, 1983). Linear methods have the advantage of efficiency but can sometimes fail if there are sharp changes or irregularities in the profile. Coupling a nonlinear algorithm with a linear algorithm combines the advantages of the robustness of the first with the efficiency of the second (Ganji et al., 1998). Figure 2.4 shows a comparison of the results of various inversions carried out using a synthetic fundamental mode dispersion curve. The nonlinear inversion results are much closer to the true profile than the simple inversion or the linear inversion results.

2.2.2 Multichannel surface wave techniques

Dobrin (1951) was amongst the first to attempt to use Rayleigh waves as a tool to determine regional velocity profiles using a controlled source and a full array of geophones. Surface waves were recorded on a large-scale array of receivers set up for a refraction experiment at the Bikini Atoll. The source used was a series of atomic bomb tests carried out in 1946. Comparison with theoretical curves available at the time lead to some useful observations and the identification of

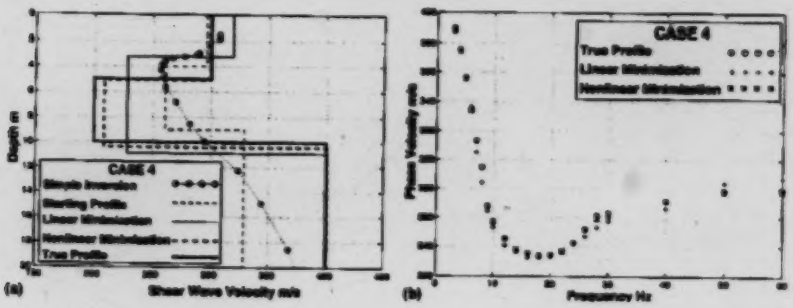

Figure 2.4: Comparison of inversion results to true profile for a synthetic example; a) Profiles at different stages of inversion; b) Associated theoretical dispersion curves (after Ganji et al., 1998).

the need for more information on Rayleigh wave propagation in unconsolidated ocean sediment.

Since then other surface wave studies employing arrays of as many as 288 geophones (Gabriels et al., 1987) have been carried out using both controlled sources (Gabriels et al., 1987; McMechan and Yedlin, 1981) and earthquakes as a source (Nolet and Panza, 1976). Nolet and Panza (1976) and Gabriels et al. (1987) were able to successfully identify a number of higher Rayleigh modes and to determine shear-wave velocities down to depths of 400 m and 50 m, respectively. The Rayleigh wave data set acquired by Gabriels et al. (1987) is displayed in figure 2.5. A total of six modes were identified on the $f-k$ spectrum for these data (figure 2.6). These more recent surveys, unlike many surface wave studies in earthquake seismology and geotechnical engineering, have employed multi-channel processing techniques.

The coupling of multi-channel processing techniques with smaller scale geotechnical engineering surveys has lead to the development of a new surveying technique. Multi-channel analysis of surface waves (MASW) is a technique developed

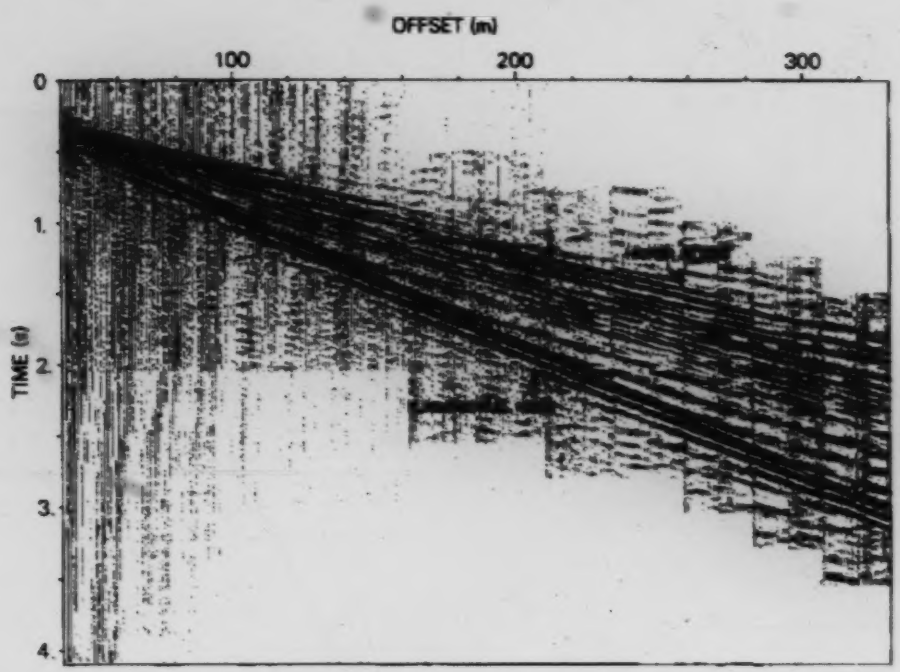

Figure 2.5: Time-offset record for 288 traces from vertical geophones spaced 1 m apart (offset: 40-327 m). Traces have been corrected for geometrical spreading and field amplification. The fundamental mode (sometimes referred to as the primary mode) Rayleigh wave, marked on the seismogram, are propagating at a slower velocity than the higher modes (after Gabriels et al., 1987).

at the Kansas Geological Survey. This group set out to reduce the number of geophones necessary to determine the shear-wave velocity profile so that the technique could be used to map out lateral near-surface shear-wave velocity changes. Surface wave data are transformed into a phase velocity versus frequency section (figure 2.7) where the peak amplitudes provide a direct image of the dispersion curves (Park et al., 1998). This technique has been successfully used to image fundamental and higher Rayleigh wave modes.

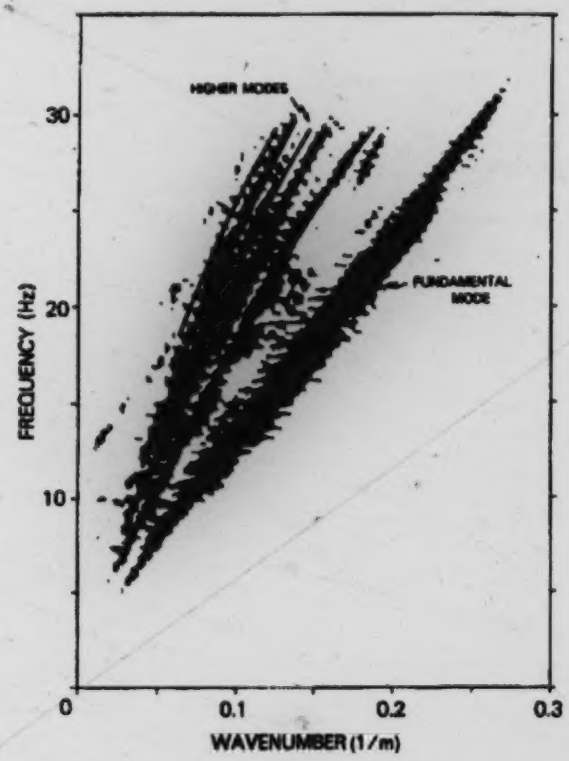

Figure 2.6: Display of $f - k$ amplitude spectrum for 256 traces with offsets of 72-327 m. The superimposed curves represent the dispersion curves calculated for the final shear-wave velocity profile obtained from these data (after Gabriels et al., 1987).

An important consideration in near-surface Rayleigh wave survey is choosing offsets so as to avoid near and far field effects. Both of these effects were observed in a mini-vibrator study (figure 3.5). A technique for decomposing recorded wavefields from an impulsive source into swept-frequency format for easy identification of the optimal range of distances to use for a MASW survey is also described. Near-field effects can be identified on a swept-frequency record

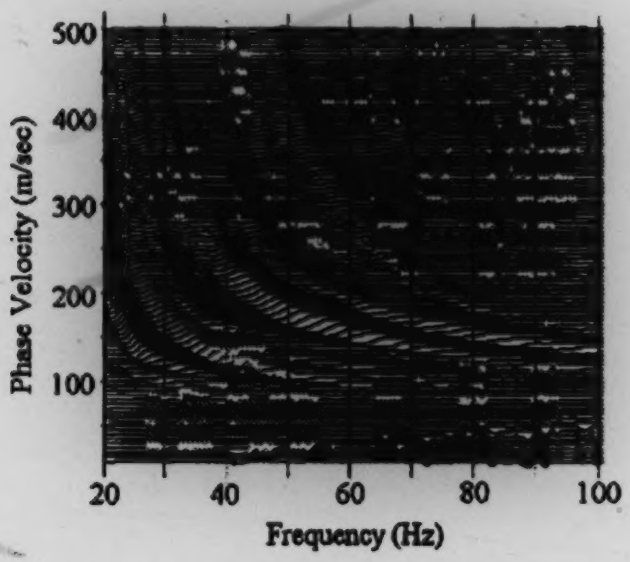

Figure 2.7: Example of the wavefield decomposition technique used by Park et al. (1998). Three Rayleigh wave modes are imaged clearly as coherent dark bands. The fundamental mode appears at th lowest frequencies and the second and third modes can be seen starting at slightly higher frequencies. For a given frequency, each mode has a progressively higher phase velocity starting from the fundamental mode (after Park et al., 1998).

by a deviation from linear slope in the record at near offsets. Higher modes appeared on the record for near offsets of greater than 0.5 times the wavelength of the wave whereas fundamental modes were observed at closer offsets of as little as 0.1 times the wavelength (Park et al., 1999a), likely due to near-field effects (Stokoe et al., 1994). Far-offset effects arise when attenuation of high-frequency components of waves traveling along the free surface cause body waves to dominate the wavefield (Park et al., 1999b).

The MASW technique is relatively insensitive to cultural noise (e.g. buried

utilities, conductive materials, electrical noise). Also, the propagation of detectable surface waves does not require an increase in velocity with depth (as refraction does) or a velocity contrast at a boundary (as reflection methods require). This often makes it possible to produce shear-wave velocity profiles successfully in areas where other geophysical techniques are difficult to use because of the noise level (e.g. EM methods, DC resistivity, magnetic methods) (Miller et al., 1999b; Miller et al., 1999c). The success of the technique is also relatively insensitive to the type of seismic source used (Miller et al., 1999c) which is an asset because for other near-surface seismic methods the source is often the greatest problem.

Linearized inversions have been carried out iteratively on dispersion curve data using the Levenberg-Marquardt and singular-value decomposition techniques (Xia et al., 1999b). The partial derivatives required for this technique were found using Ridders' method of polynomial extrapolation, a standard technique for evaluating partial derivatives numerically (Press et al., 1997). Numerical methods for determining partial derivatives are not as accurate as variational methods (Novotný, 1976), which have also been used in developing linear inversion techniques (Aki and Richards, 1980; Takeuchi and Saito, 1972) but are much simpler to code. A linearized inversion technique was also adopted by Gabriels et al. (1987) (figure 2.9). The standard deviations in the S-wave profile found through inversion were determined using the partial derivatives of the velocities with respect to phase velocity along with the data covariance matrix. There is an increase in uncertainty in S-wave velocity with depth that is characteristic of surface wave techniques.

Initial models for the inversion of Xia et al. (1999b) were determined using the simple inversion formula described in Stoke and Nazarian (1985). In this simple inversion, the shear wave velocity is taken as an arbitrary percentage (close to

110%) of the phase velocity and assigned to a depth of 1/3 to 1/2 of the wavelength. This method does not generally provide an accurate representation of the shear-wave profile so it should not be used in place of a true inversion. Figure 2.8 shows an example of their inversion results compared with the dispersion curve data and borehole S-wave velocity measurements. Only the fundamental mode has been used in the inversions performed by this group.

Comparison of a set of MASW profiles to borehole measurements of S-wave velocity at seven well locations in the Fraser River Delta (figure 2.10) shows that the two methods differ overall by about 15% (Xia et al., 1999a). In another study, discrepancies between borehole and MASW profiles was found to be only 9% (Xia et al., 1999b). Shear-wave profile determination from surface wave methods offers similar accuracy to borehole measurements at a fraction of the cost and without many of the environmental risks associated with borehole methods (Xia et al., 1999b).

The MASW technique has been successfully applied to several environmental problems. In one case a series of MASW surveys were carried out in conjunction with shallow reflection to enhance the effectiveness of a drilling program designed to locate dissolution features at a potential power plant site (Miller et al., 1999a). It has also been shown to be a useful tool for mapping the depth to bedrock (depths of 2-7 m were examined) and potential fracture zones, both of which can influence the transport and eventual fate of contaminants released at or near the ground surface.

2.2.3 Surface waves in earthquake seismology

The idea of using surface waves as a tool to probe the velocity structure of the Earth is one that originated in the field of earthquake seismology. Surface waves generated by earthquakes are an important tool for studying shear-wave

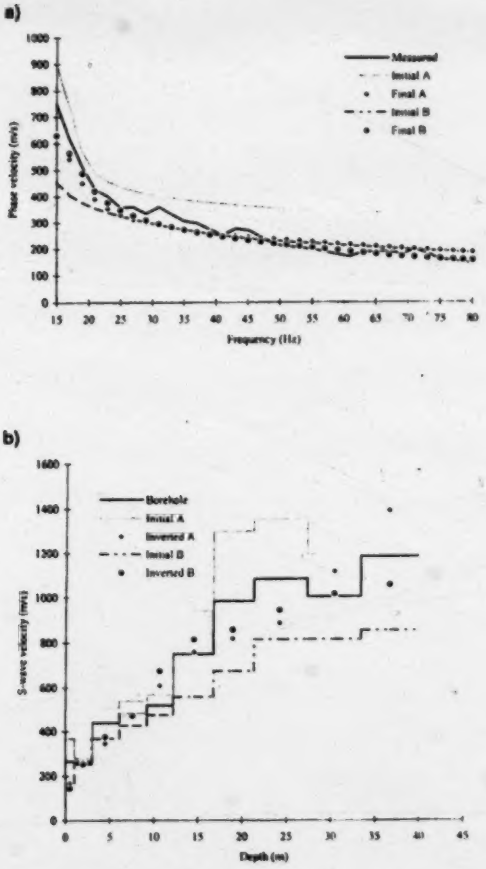

Figure 2.8: Inversion results carried out on real MASW dispersion curve data starting from two different initial models. Initial model B was chosen using the simple inversion algorithm while A was chosen to be uniformly greater than borehole measurements. a) Dispersion curves for the various velocity models along with the measured dispersion curve; b) S-wave velocity models used as initial values in the inversion, resulting from inversion of the dispersion data and determined from borehole measurements (after Xia et al., 1999b).

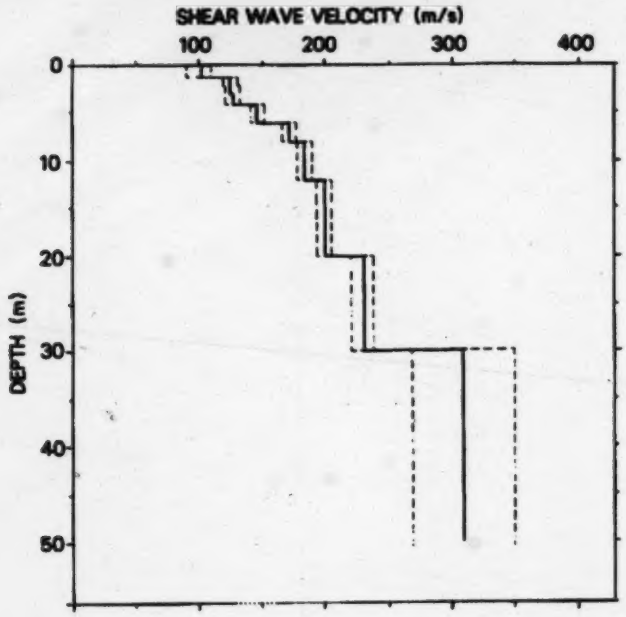

Figure 2.9: The final model for the shear-wave velocity profile obtained from the surface wave data in figure 2.5 (solid line) with its standard deviation (dashed line) (after Gabriels et al., 1987).

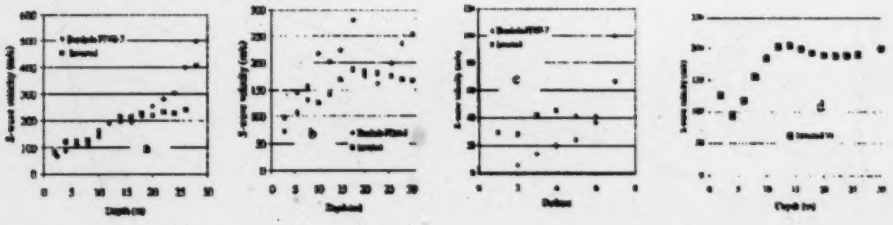

Figure 2.10: Inverted S-wave velocities and borehole measurements taken at four different locations in the Fraser River Delta. For d) no borehole information is available (after Xia al., 1999a).

velocities in the crust and upper mantle. Dahlen and Tromp (1998) provide an extensive coverage of the use of surface waves in earthquake seismology as well as free oscillations of the Earth, which are related phenomena.

There are two independent types of free oscillations - spheroidal oscillations which alter the external shape of the Earth and toroidal oscillations which do not. These two types of free oscillations are the standing-wave analogues to the propagation of Rayleigh and Love waves. Spheroidal oscillations are related to Rayleigh waves while toroidal oscillations are related to Love waves. Free oscillations provide whole earth scale averages and generally are capable of deeper investigation than surface waves (Dahlen and Tromp, 1998).

Surface wave investigations are carried out at a variety of scales ranging from average velocity profiles of the crust and upper mantle for all shield, oceanic and tectonic regions and phase velocity maps for the entire globe (Laske and Masters, 1996) to more detailed studies of specific areas, for example a mid-oceanic ridge (Forsyth et al., 1998).

Toksöz and Anderson (1966) used surface waves of periods 80 to 670 seconds, generated by the Alaska earthquake of March 28, 1964 to study crustal and upper mantle phase velocities. They chose to analyze their results in terms of average properties of oceanic, tectonic, and shield regions. The oceanic dispersion curve falls roughly midway between that of the shield (fast) and of the tectonic regions (slower). The survey did not have high enough resolving power to break the oceanic region into subsets although it is suggested that ocean basins, deep trenches, rises and mid-oceanic ridges should not be expected to be underlain by identical mantle. Figure 2.11 shows the phase velocities for each region for Love waves. Mixed path S-wave velocity models determined for the average conditions over the Mongolia-Pasadena path (model CIT-12 shown in figure 2.12) provides a theoretical dispersion curve that fits very well with Rayleigh wave dispersion

information for this path (figure 2.13).

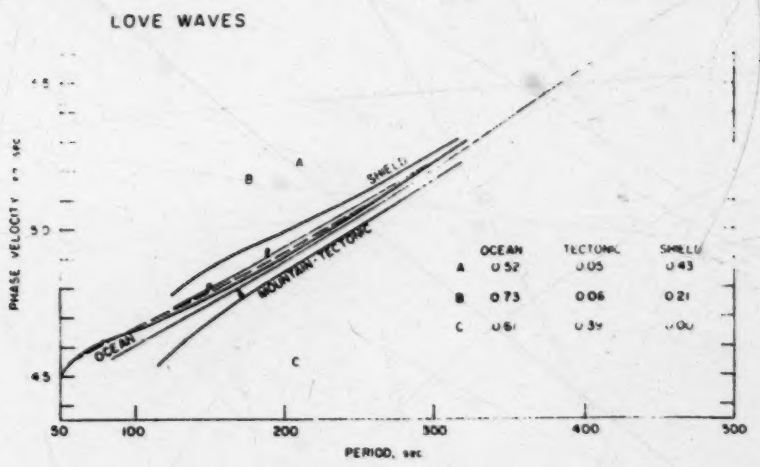

Figure 2.11: Observed composite-path Love wave data and the extracted pure-path dispersion curves (after Toksöz and Anderson, 1966).

Dziewonski (1970) performed a similar study and showed that dividing the surface wave paths into the three "pure path" regions is statistically meaningful, especially when comparing oceanic and shield paths. A least-squares inversion algorithm was used to match the pure-path dispersion results with simple Earth models which show that oceanic regions are characterized by a well-developed low-velocity zone in the upper mantle (Dziewonski, 1971).

A recent study used both Rayleigh wave and Love wave dispersion curves to create global phase velocity maps at frequencies of 5, 10 and 15 mHz (figure 2.14). These maps show phase velocity perturbation with respect to a global model and tend to highlight these observed differences in oceanic, tectonic and shield phase velocities. Red areas of the maps are associated with slower than average velocities and relatively hot areas of the earth while the blue areas indicate faster

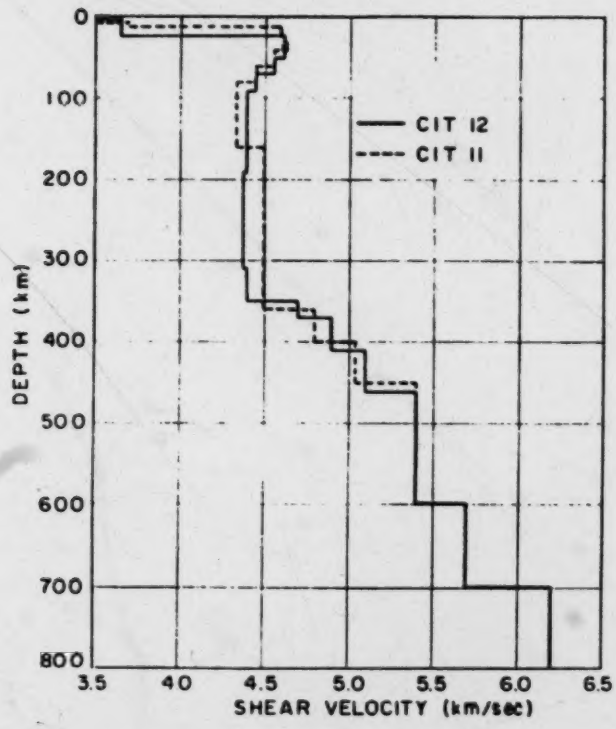

Figure 2.12: Shear velocity distributions for the CIT-11 (New Guinea-Pasadena path) and CIT-12 (Mongolia-Pasadena path) models (after Toksöz and Anderson, 1966).

velocities thought to be related to colder regions (Laske and Masters, 1996).

Another study (Dziewonski and Steim, 1982) used a waveform inversion technique on both Rayleigh and Love waves, determined that oceans older than 38 Myr have faster velocities than younger oceans. Even though Love waves cannot propagate through fluids they can still propagate through the crust and mantle beneath the ocean and are usually recorded using ocean bottom seismometers in locations where there is no dry land. The young oceans have shear-

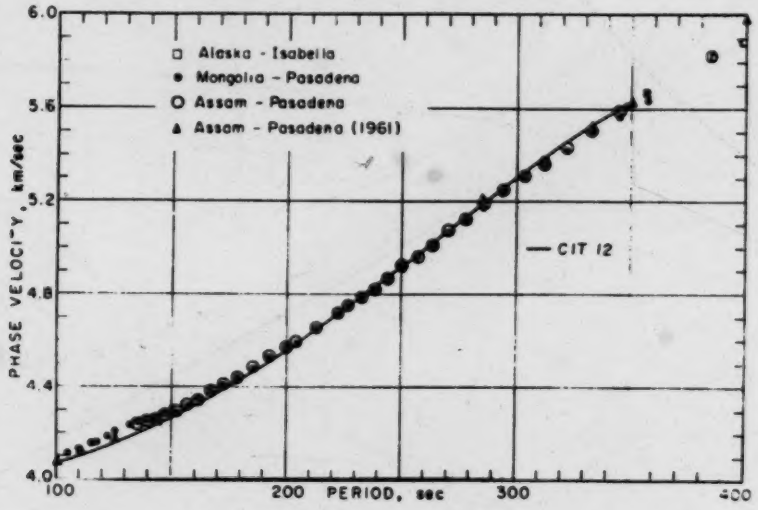

Figure 2.13: Rayleigh wave dispersion curve for the CIT-12 mixed-path model and the observed data over Mongolia and Assam-Pasadena paths which are quite close together (after Toksöz and Anderson, 1966).

wave velocities that are 0.3 km/s slower in a depth range from 80 to 220 km and show a major (4%) difference in the depth range of 400 to 670 km. For intermediate depths, no major differences are observed. In order to explain these velocity discrepancies through temperature alone, the contrast would have to be on the order of 500°C, which is unrealistic. Upper mantle velocities for stable continents and old oceans are similar.

A more detailed study (Nishimura and Forsyth, 1989) used fundamental mode Rayleigh (periods of 20 - 125 s) and Love waves (periods of 33-125 s) to examine the velocity structure and anisotropy (from path directions and from comparing the velocities of SH and SV-waves) of the Pacific seafloor. The upper mantle is composed primarily of olivine (chemical formula $(Mg, Fe)_2SiO_4$). Anisotropy in the upper mantle is thought to result from systematically aligned olivine crystals

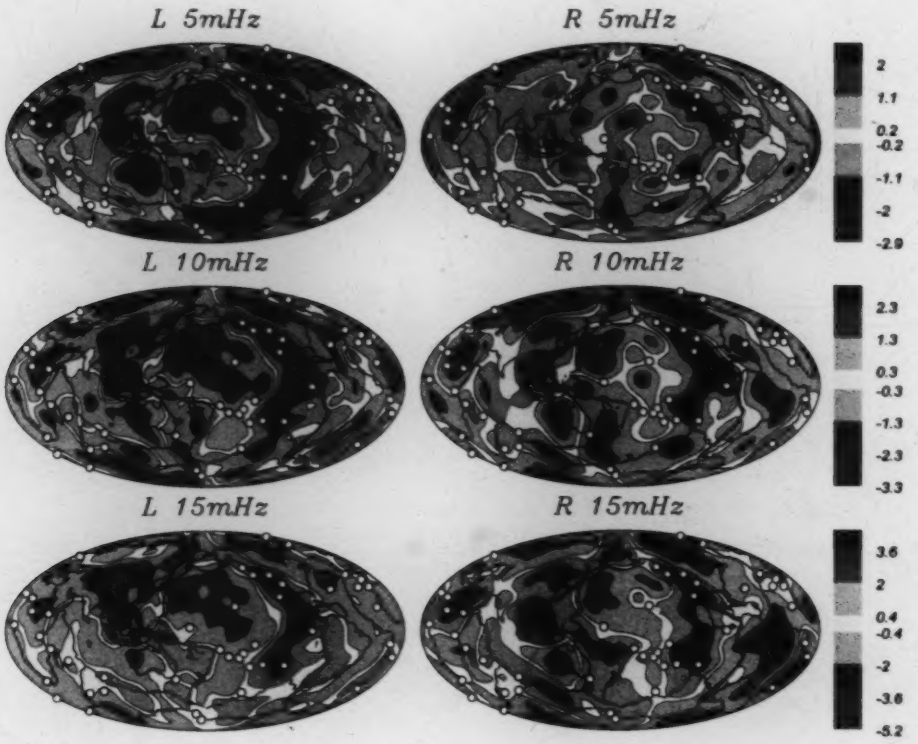

Figure 2.14: Phase velocity maps for Love (left) and Rayleigh waves (right) at 5,10 and 15 mHz. These maps show percentage phase velocity perturbation after the mean has been taken out. The amplitudes in the maps increase with frequency but never exceeds 7%. The white dots mark hotspot locations (after Laske and Masters, 1996).

with the fast olivine a-axis [100] preferentially oriented in the horizontal plane (figure 2.15).

Anisotropic inversion of the surface wave data (figure 2.16) indicates significant anisotropy in regions of the Pacific less than 80 Myr down to a depth of 200 km. In regions older than 80 Myr there is anisotropy only down to 50 km.

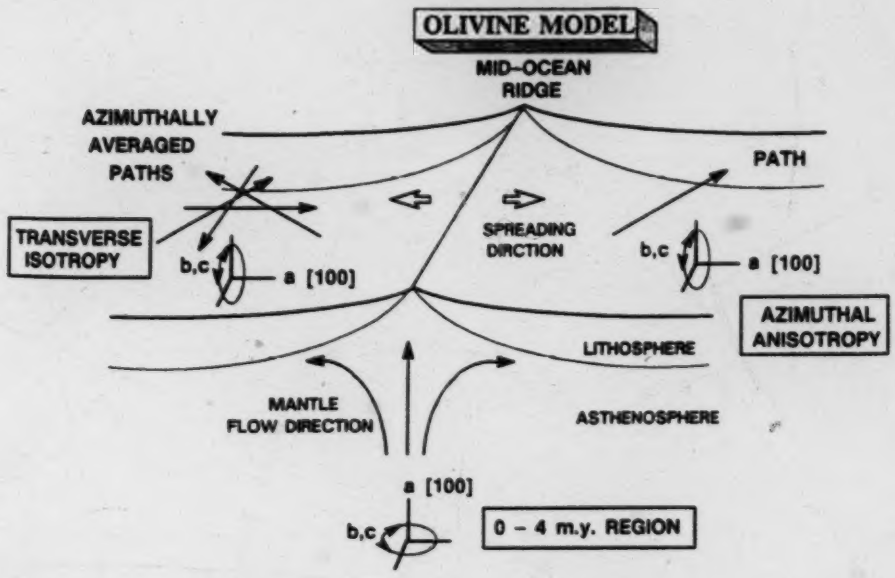

Figure 2.15: Idealized diagram illustrating the preferred model for the oceanic upper mantle in the Pacific. The upper mantle appears to be transversely isotropic if averaging over a number of azimuthal paths is performed. This averages out any azimuthal velocity dependence. The amplitude of the transverse isotropic effect under the mid-ocean ridge system is expected to be low due to the contribution of both horizontal and vertical flow in this region (after Nishimura and Forsyth, 1989).

The anisotropy pattern qualitatively mimics the isotherms of the theoretical thermal cooling of the seafloor, progressively increasing as a function of seafloor age with the greatest velocity change observed in the first 20 Myr (Nishimura and Forsyth, 1989). The observed velocity changes in this age region, however, are larger than can be explained by simple conductive cooling, a feature that is examined in more detail by the MELT experiment (Forsyth et al., 1998).

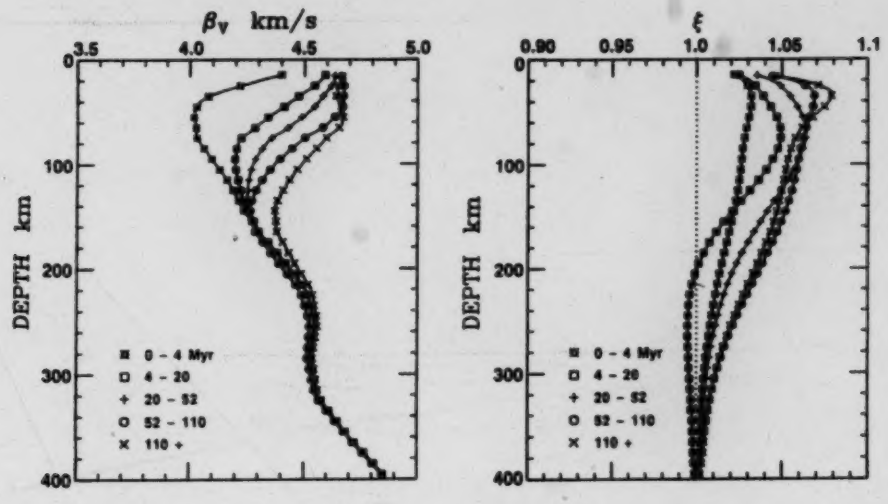

Figure 2.16: Transversely isotropic upper mantle structure found from Rayleigh wave and Love wave dispersion curves. The two parameters shown, β_V and $\xi = (\beta_V/\beta_H)^2$ which represent the S-wave velocity in the vertical direction and the shear wave anisotropy term respectively, are the parameters that could be resolved the most reliably from the data (after Nishimura and Forsyth, 1989).

It is believed that shallow azimuthal anisotropy (within the lithosphere) in regions of the Pacific less than 80 Myr may be related to the direction of fossil seafloor spreading. Deeper anisotropy is likely to be related to present-day absolute plate motions. In the younger crust, the absolute plate motion and the direction of seafloor spreading cause anisotropic effects that are aligned. This has not necessarily always been the case so it is possible that the detection of only shallow anisotropy in older oceanic crust may be due to destructive interference which would result if the directions of anisotropy are not aligned, thereby making the deeper anisotropy undetectable using Rayleigh waves (Nishimura and Forsyth, 1989).

In the youngest region considered (0-4 Myr) the direction of fast velocity was found to be more vertical as opposed to the more horizontal orientation observed further from the ridges. This effect is thought to be due to the more vertical flow direction of the mantle in this region (Nishimura and Forsyth, 1989).

The Mantle Electromagnetic and Tomography (MELT) Experiment, a recent study that took place over the East Pacific Rise (EPR), used surface wave dispersion in conjunction with a variety of other techniques to map out the physical properties of the crust and upper mantle of the region in detail. The object of the study is to use seismic and electromagnetic techniques to distinguish between competing models of magma generation beneath mid-oceanic ridges. Specific goals of this experiment are to constrain the pattern of upwelling beneath the ridge, the geometry of the region of partial melting, the melt concentration in the region, the distribution of melt within the matrix, and the connectedness of the melt pockets (The MELT Seismic Team, 1998). The study site is one of the longest, straightest section of a global spreading system which is spreading at a rate of 145 km per million years (quite fast).

Figure 2.17 shows the great circle paths for earthquakes distributed around the margins of the Pacific that were recorded by the MELT array (a) and the experimental layout on the ocean floor around the East Pacific Rise (b). Inversions for velocity structure and azimuthal anisotropy (assuming weak anisotropy) were carried out for the area corresponding to good ray coverage (Figure 2.18). A period of 25 seconds was chosen for the inversions because the phase velocity at this period represents an integrated measure of the shear velocity in the upper 100 km with the greatest sensitivity to depths of 20 to 70 km, which is of interest as it is expected to be the primary melt production zone. Lateral resolution in the central portion of the study area is as fine as 100 km by 100 km. To reduce the number of variables in the inversion, the coefficients of anisotropy were only

allowed to vary according to distance east or west of the ridge.

The velocity variation seen in Figure 2.18 is the two-dimensional variation of the isotropic phase velocity. Both inversion models were obtained from a starting model that was isotropic and symmetric about the ridge axis. Figure 2.18a is the result of imposing a smoothing constraint on the model whereas Figure 2.18b is the product of using a minimum length constraint that corresponds to weaker damping. The best constrained area of the model is the area bound by 117°W, 110.5°W, and the two receiver lines (Forsyth et al., 1998).

There are primary features that are similar in both models but discrepancies in the detail. The width of the area with velocities of less than 3.80 km/s is more than 400 km, indicating a broad zone containing melt rather than a narrow column. An asymmetry is observed with the lowest velocities situated 50 to 100 km to the west of the ridge (Forsyth et al., 1998), which is consistent with other evidence gathered by the Seismic MELT Team (The MELT Seismic Team, 1998).

The observed anisotropy, averaged for the entire region, has a fast direction of 115°N and 1.8±0.3% peak-to-peak anisotropy. The amplitude of the anisotropy increases to the west by 3 to 5% and to the east by 2 to 3%. There is a gradual rotation of the fast direction to the southeast with distance from the ridge axis. In the low velocity region the anisotropy is also very small, compatible with an olivine upwelling flow pattern.

The surface wave component of this study will help to map out the geometry of the melt zone and any anisotropy associated with the melt pockets or alignment of crystals. The data show that the very young oceanic crust (less than 1.5 Myr) has significantly faster phase velocities than older oceanic crust, in agreement with data from previous teleseismic measurements. These faster velocities are thought to be indicative of the presence of partial melt. The amount of melt

present is not well constrained by the anisotropy and could vary between a few tenths of a percent if the melt pockets are thin films, to 5% for concentrated pockets (Forsyth et al., 1998).

2.2.4 Near-surface seasonal variation study

Surface waves have served as a useful tool to study the subsurface for a wide range of scales. Depths of examination range from less than a metre in pavement studies to several hundreds of kilometres in earthquake seismology projects. As a technique for studying the near-surface, surface wave dispersion is attractive for a number of reasons. Surface waves are relatively easy to generate and acquire and the surveys are insensitive to cultural noise which can be prohibitive to other geophysical methods. This method has been shown to produce shear-wave velocity profiles that agree well with borehole seismic measurements at a fraction of the cost. It is a non-invasive technique that can be easily repeated at the same location and is thus a method well suited to a study of seasonal variability of the elastic properties of the near-surface.

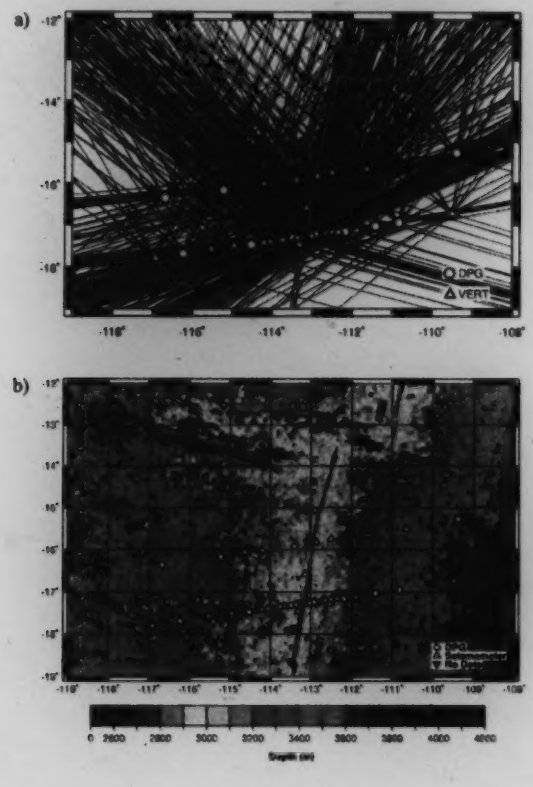

Figure 2.17: a) Great circle paths crossing the MELT study area. The white line marks the spreading center while the locations of ocean bottom 3 component seismograms are marked by open triangles and pressure readings by open circles. At a period of 25 s, 703 paths from 23 earthquakes to 39 stations were used in the tomographic inversion (Forsyth et al., 1998); b) Bathymetry of the MELT study area with symbols for seismometers the same as in a) and seismometers that returned no data marked as inverted, filled triangles. The arrays were oriented at an angle to the ridge such that they would lie along the great-circle path that includes the seismically active regions bordering the southwest Pacific (The MELT Seismic Team, 1998).

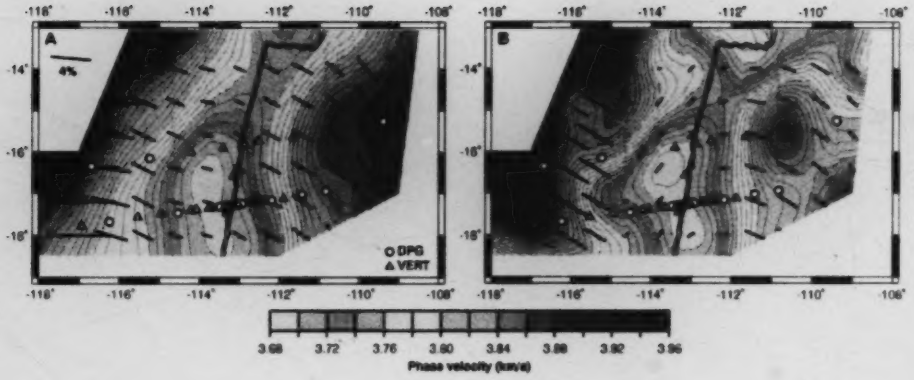

Figure 2.18: Results of tomographic inversions of Rayleigh wave phase velocities at a period of 25 s. Comparison of the two models shows that resolution is poorer near the edges but that there are features closer to the ridge that are imaged by both models. The black bars indicate the direction and degree of azimuthal anisotropy. a) Inversion with a strong smoothing constraint using a starting model that is symmetric about the ridge axis; b) Inversion with a weak minimum length constraint with the same starting model as used in a). (Forsyth et al., 1998).

Chapter 3

Experimental Set-up

Repeated surface wave data sets were obtained at the University of Alberta experimental farm, also known as the Edmonton Research Station, over the course of the summer and early fall of 1999 in order to monitor changes in elastic properties of the near-surface in hopes of relating them to changes in the near-surface soil conditions.

The experiment was set up to gather seismic surface waves using an array of three-component geophones (10 Hz) and a separate set of vertical geophones (14 Hz) at 0.5 m spacing. This geophone spacing distance was chosen to avoid spatial aliasing of wavelengths as small as 1 m (Nyquist wavenumber $k = 2\pi/\lambda_{min} = 6.28\ \mathrm{m}^{-1}$). These small wavelengths contain information about the shear-wave velocity of the first 1/2 to 1/3 of a meter. Imaging layers thinner than this accurately would require even closer spacing. If close enough spacing is not chosen then spatial aliasing will occur which results in energy from wavenumbers greater than the Nyquist wavenumber being folded back into the Nyquist interval. Geophones (figure 3.1) were placed as close to the source as 0.25 m with 0.25 m spacing out to 2 m and 0.5 m spacing after that out to a distance of 38 m. The closer spacing in the first 2 m was chosen to provide sufficient resolution to allow

for refraction analysis of the data. *P*-waves are expected to travel quite slowly in the top-most layer and the closer spacing near the source is required to resolve thin, low velocity layers just below the surface.

The shot point and receiver line were surveyed in each time using an optical survey scope, measuring tapes and flags. Gate posts at opposite ends of the field were used along with a fire hydrant as reference points to ensure repeatability of the experiment. Shallow holes (about 20 to 30 cm deep) were dug and the receivers were firmly planted inside. Care was taken in positioning and levelling the geophones. The three-component geophones have a bubble level and two arrows that can be used for reference in positioning. The experimental layout is shown in figure 3.2. Before recording, the geophones were covered over with soil to help damp the air wave as well as noise from the wind. A photograph of the recording truck and the receiver line at the Edmonton Research Station is shown in figure 3.3.

A sledgehammer impacting on an aluminum plate was used as a source (figure 3.4). To operate this source, the striker kneels on a foam pad in order to minimize operator noise. The operator attempts to strike the centre of the plate each time without letting the hammer reverberate. Ten shots were recorded at each location and stacked to improve the signal to noise ratio. Two other source types were tested initially and rejected. A small axe impacting on the aluminum plate did not provide sufficient energy at large offsets. The other source tested was an accelerated weight drop. This source required the use of a motor to raise up the hammer that even when damped generated too much noise given the close offsets being used. This source had the additional problem that the hammer tended to bounce off of the plate on impact and generate a second impulse. The sledgehammer source provided sufficient energy to generate surface waves at the offsets being considered, offered repeatability that was sufficient for

a survey concerned more with velocities than with true amplitudes, and was also very portable and affordable.

Park et al. (1999b) discuss the near-field effects that arise from positioning the receiver array too near to the source and this was taken into consideration before performing the dispersion analysis. Figure 3.5 illustrates how the near-field effects and far-field effects, which should not be a problem at the offsets used in this study, effect the surface wave data. A near offset of 7 m was chosen for the analysis because clear surface wave arrivals were observed to be well separated in time from the direct and air waves at this point. Figure 3.4 shows the receiver locations used in the surface wave analysis. The data from closer offsets were used to help determine this near offset distance and in the refraction analysis (discussed in Chapter 4).

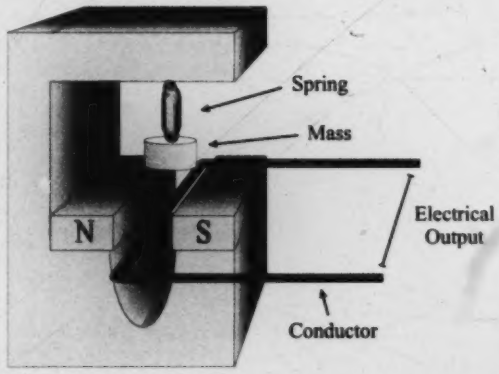

Figure 3.1: Simple model of a velocity geophone of the type typically used in seismic exploration. When a seismic wave passes the case and magnet move but the mass suspended from the spring tends to remain stationary. An output voltage is generated proportional to the velocity of the relative motion between the conductor and the magnetic field (Kearney and Brooks, 1995).

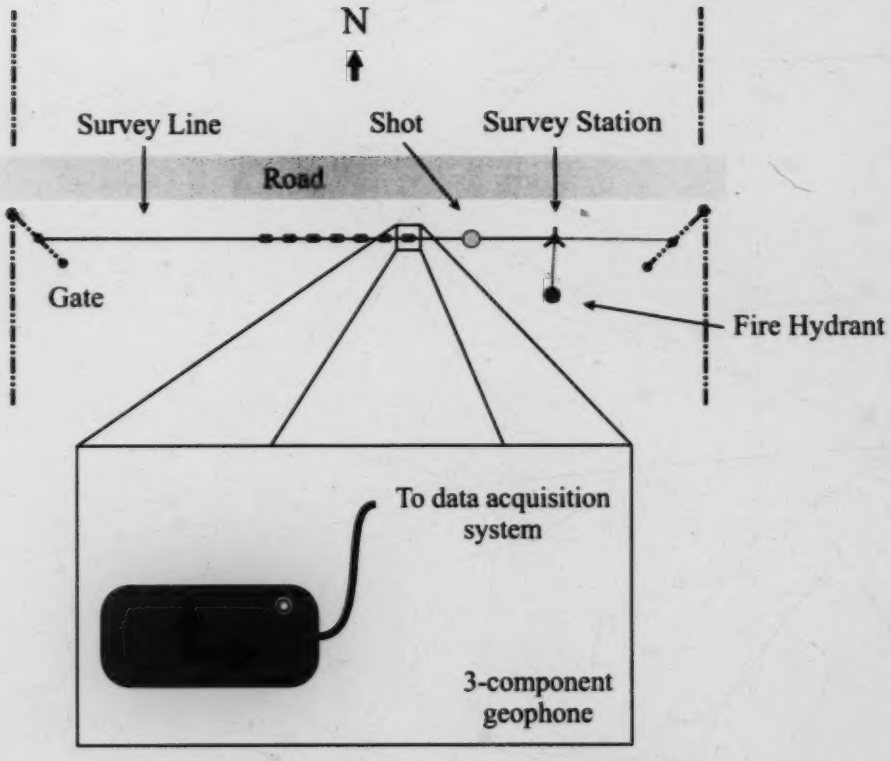

Figure 3.2: Plan view of the layout used for this experiment. Each time the study was repeated, the line was surveyed out using the fire hydrant and the gate posts, which were always in the same position, as reference points. The 3-component geophones were oriented so that the two arrows on the case pointed towards the north and towards the shot point. A bubble on the corner of the case allows the geophones to be levelled.

Figure 3.3: Seismic recording truck next to the receiver line at the Edmonton Research Station.

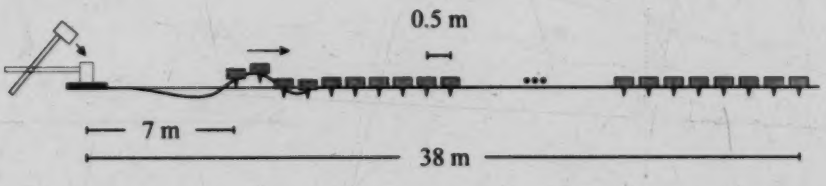

Figure 3.4: Geometry of the survey performed at the Edmonton Research Station indicating the geophone locations used in the surface wave analysis (not to scale). A sledge hammer source was used. The solid line illustrated the propagation of a surface wave. The equilibrium position of the free surface is indicated by the dotted line.

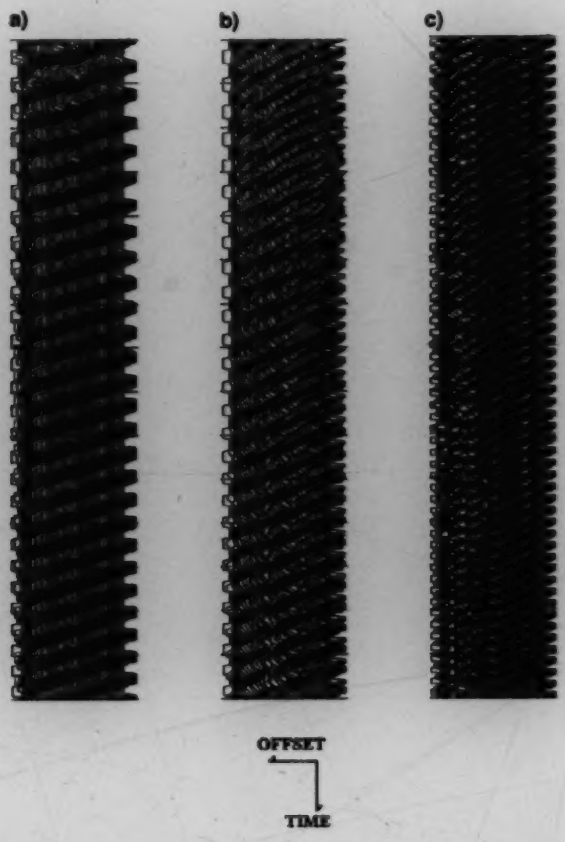

Figure 3.5: Vibroseis field data acquired by Park et al. (1999b). The first trace in each seismogram represents the sweep used. The data in a) show coherency in the ground roll indicating good data quality (minimum offset 27 m). The seismogram in b) demonstrates near-field effects which can be identified by the reduced coherency and fragmentation of the energy packets (minimum offset 1.8 m). In c) the far-offset effects are identifiable by the decrease in ground roll slope (increase in apparent phase velocity) for the same frequencies at closer offsets (not shown) and by the reduced coherency (after Park et al., 1999b).

Date	Receivers
May 20, 1999	3-C (truncated)
May 31, 1999	3-C
June 11, 1999	3-C and V
June 22, 1999	3-C
June 28, 1999	3-C
July 14, 1999	3-C
July 27, 1999	3-C and V
August 6, 1999	3-C and V
August 27, 1999	3-C and V
September 9, 1999	3-C
May 5, 2000	3-C

Table 3.1: Summary of seismic surveys where 3-C and V indicate that three component geophones or that the 14 Hz vertical geophones were used, respectively.

A total of ten data sets were obtained over the course of the summer of 1999 every two to three weeks starting on May 20 and ending on September 9. On several of these days, an independent data set was acquired using the same source and acquisition parameters only substituting a set of 80 single component vertical geophones (14 Hz) for the three-component geophones just for the sake of comparison. An additional three-component data set was acquired on May 5, 2000, allowing a comparison between two separate seasons to be made. A summary of the seismic data sets that were obtained can be found in table 3.1.

In all cases a sledgehammer source was used with the exception of May 20, 1999 where a small axe was used at near offsets and then for the last 8 m of the survey an accelerated weight drop source was used. The data from this

Data Set	Δt (ms)	Number of Points	f_{Ny} (Hz)
May 20, 1999	0.125	4096	4000
May 20, 1999 (decimated)	1	1024 (padded)	250
May 31, 1999 - May 5, 2000	0.125	8192	4000
May 31, 1999 - May 5, 2000 (decimated)	1	1024	250

Table 3.2: Summary acquisition parameters where f_{Ny} is the Nyquist frequency. In the case of the May 20 data, the data were zero padded out to 8192 points before decimating in order to simplify processing.

particular survey showed that the axe did not generate sufficient power at large offsets whereas the weight drop source generated sufficient power to saturate the near-offset geophones and had to be run using a motor which generated significant noise. The sledgehammer provided sufficient energy at the offsets being considered with minimal noise.

A sampling rate of 0.125 ms was used, providing a Nyquist frequency of 4000 Hz, with 8192 samples recorded for all of the surveys except for that conducted on May 20, 1999. The data were later decimated to decrease processing costs but a Nyquist frequency of 500 Hz was maintained. For the initial survey (May 20), only 4096 points were recorded so a small amount of surface wave data at larger offsets was missed. These data were zero padded out to 8192 points before decimating in order to simplify processing. Table 3.2 summarizes the acquisition parameters used in the field and the corresponding parameters after decimation of the data.

Bus traffic on 122 St. was detectable as well as noise from farm machinery, joggers, bikers and automobile traffic through the farm itself. It was possible to minimize the effects of this cultural noise by keeping a careful watch and

recording only during quiet periods and by the "vertical" stacking of the data.

A representative three component data set is shown in figures 3.6 to 3.8. In these figures, every second trace has been omitted in the first 2 m so that the seismogram can be displayed with equal trace spacing of 0.5 m. Energy balancing (normalization by RMS amplitudes over the full length of each trace in this case) has been applied to account for the amplitude effects of geometrical spreading and more random differences in source strength and geophone coupling. The most prominent arrivals on the vertical and horizontal longitudinal components are Rayleigh waves (particle motion for a Rayleigh wave traveling in the x direction is confined to the x and z planes whereas for a Love wave particle motion is only in the y direction). The first arrivals on the vertical component are the direct and refracted P-waves (arrival times of less than 0.06 s) which were used to estimate the P-wave velocity profile independently (see Chapter 4).

Figure 3.9 shows the different types of waves found in a typical vertical component seismic shot gather. An automatic gain control or AGC (normalization over a sliding time window) has been applied to these traces to boost the signal strength at later times. The direct and refracted P-waves, Rayleigh waves, the air wave which is the wave from the impact traveling just above the surface through the air to the geophone, and the area on the seismogram where reflections can be found are all identified in this figure. A sledgehammer source impacting on a metal plate generates P-waves well but S-waves only weakly so the S-wave direct and refracted arrivals, which would be expected to arrive later in time than the corresponding P-wave arrivals, are low in amplitude compared to the other waves in the seismogram making them difficult to identify.

The horizontal transverse component is noisier than the other components. The strongest arrivals seen here should be Love waves. Love waves result from the constructive interference of various SH waves at the surface when there is

an increase in velocity with depth. Since they are made up entirely of SH waves they should theoretically only be detectable on the horizontal transverse component. Some of the noise on this component may be due to error in the angle of the receiver placement which would result in contamination of the Love waves with some energy from the Rayleigh waves and imperfections of the detecting geophones themselves.

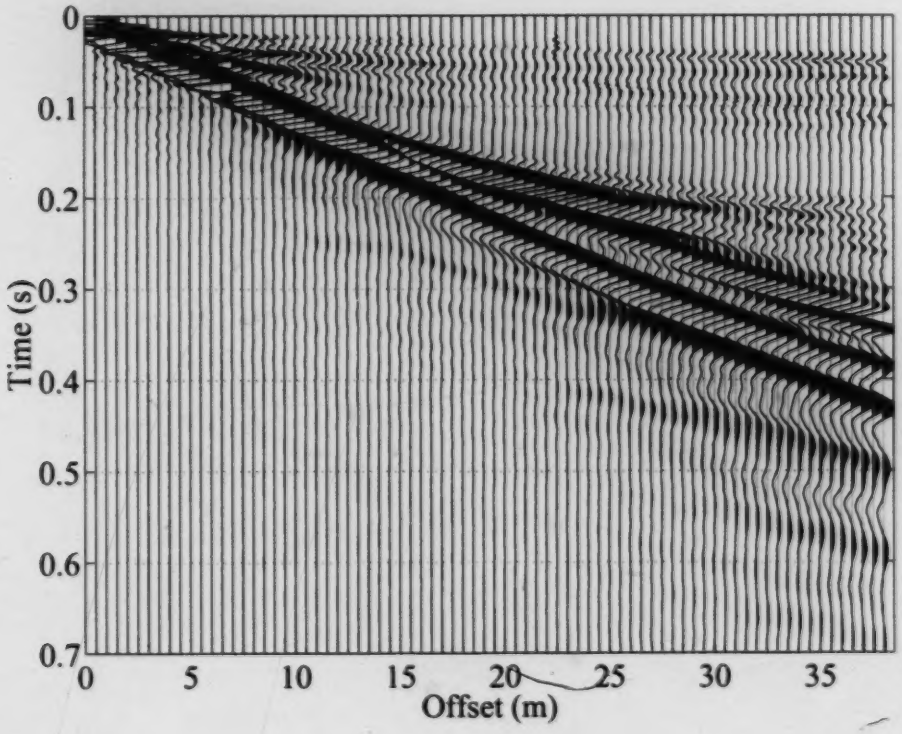

Figure 3.6: Stacked data recorded on September 9, 1999, vertical component.

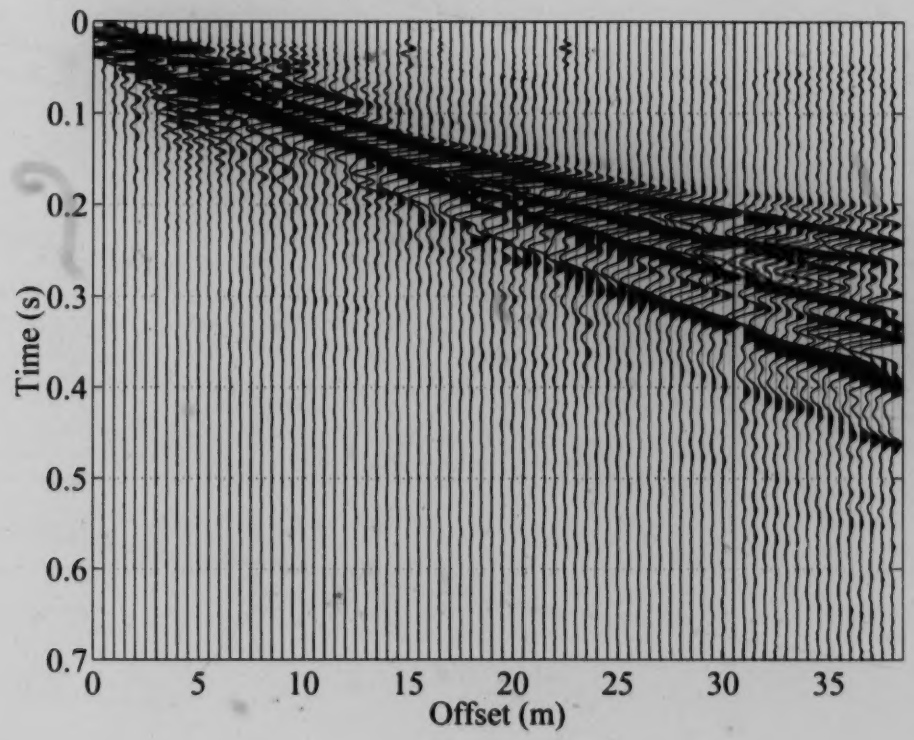

Figure 3.7: Stacked data recorded on September 9, 1999, horizontal transverse (HT) component.

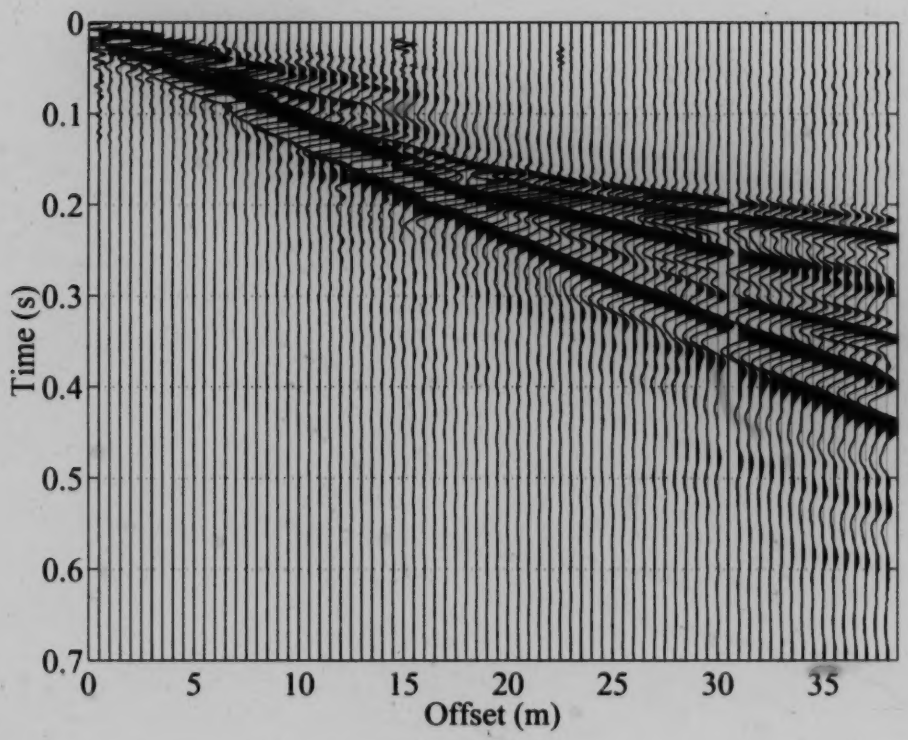

Figure 3.8: Stacked data recorded on September 9, 1999, horizontal longitudinal (HL) component.

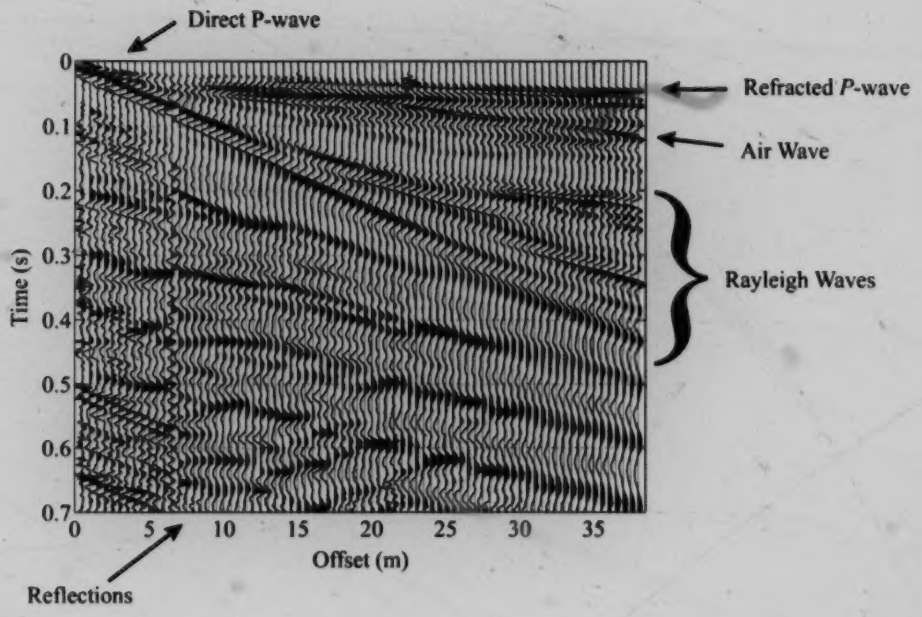

Figure 3.9: This figure shows the different types of waves found in a typical seismic shot gather.

3.1 Frequency limitations of equipment

This study depends critically on the fidelity of the seismic data acquired and as a result it is important to determine whether the recording system could adversely influence the data quality. The data acquisition system used was an OYO-DAS1 system with 48 channels with a timing accuracy of 31.25 μs. The system includes an analog low cut (3 Hz @ 6 dB/octave) and anti-alias filters (4700 Hz @ 12 dB/octave). The amplitude and phase response of the data acquisition system is shown in figure 3.10. The amplitude response drops off fairly rapidly near the 3 Hz mark and has no effect between 10 and 100 Hz which is the region of interest. The phase response shown (i.e. the phase shifts that will be introduced to the recorded data at each frequency), however, is significant up to 30 Hz. Fortunately the method being used in this study to determine phase velocities of the surface waves deals with each frequency independently and finds the velocity through phase delays with respect to the other traces, not with respect to the initial times and such instrumental shifts common to all measurements are no longer important. These properties of the chosen analysis technique make it possible to neglect phase shifts introduced by the acquisition system because they will have no effect on the dispersion curves.

The frequency response of the geophones being used should also be considered. Two types of geophones were used in this experiment: a set of 10 Hz, 3 component geophones, and a set of 14 Hz vertical geophones. The specifications for both sets of geophones can be found in table 3.3. The phase effects can again be neglected but it should be noted that for the 14 Hz vertical geophones there is a gradual decrease in amplitude response below about 23 Hz that becomes an exponential drop below 14 Hz. At the high frequency end the response remains flat to greater than 400 Hz. For the 10 Hz geophones, the amplitude response starts to drop gradually at around 20 Hz and exponentially below 10 Hz. The

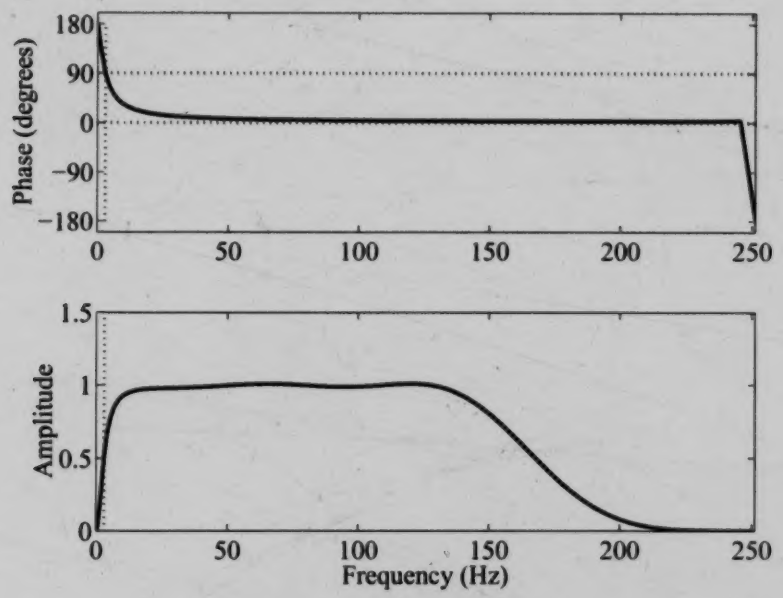

Figure 3.10: Phase (top) and amplitude (bottom) response of the OYO data acquisition system for a sampling rate of 2 ms (private communication, OYO Instruments, Inc., 9777 Gulf Bank Suite 10, Houston, Texas 77040). The low frequency response is due to the 3 Hz low-cut analog filter and the high frequency response is due to a digital anti-aliasing filter that is applied before storing the data.

high frequency end of the curve is flat up to 150 Hz.

3.2 Trigger test

A number of triggering devices were used for seismic data acquisition. On June 11, 1999 a test was performed to the reliability in timing of the small piezo trigger, a large piezo trigger, and a contact trigger, and a contact trigger with an

Manufacturer	Components	Product	f (Hz)	Coil L (Ohms)	Shunt (Ohms)	Damping
Mark Products	1	L-410	14	330	846	0.700
Mark Products	3	L-28A-1	10	395	3331	0.700

Table 3.3: Specifications for geophones used in this study where f is natural frequency, and L is impedance.

optical isolater attached to the aluminum plate. The piezo triggers respond to the acoustic signal from the hammer hitting the plate while the contact trigger sends the signal to start recording when a circuit is completed from the metal end of the hammer to the aluminum plate. Vertical geophones (14 Hz) were used as receivers in the first 48 positions (0.25 m spacing out to 2 m, 0.5 m spacing out to 23 m). Three shots (with no stacking) were recorded using each of the 4 triggers. Results are shown in figure 3.11. For this test a sampling rate of 0.125 ms was used, the same as that used for obtaining surface wave data.

The mean and standard deviations found in comparing the first arrival picks from the different trigger types to the small piezo trigger are shown in table 3.4. These results show that there is a difference between the small and large piezo trigger of 0 ± 2 samples, meaning that the trigger timing between the two piezo switches is indistinguishable. The standard deviation of 2 samples (0.25 ms) can be attributed to random noise and differences in the location the hammer hits the plate at with each swing. This random fluctuation should have a negligible effect on the phase velocity measurements. The time differences between the contact switch without and with the optical switch present are the same within the standard deviations of the pick times, however, their time difference from the piezo triggers are 5 ± 2 and 6 ± 1, respectively. In true time these translate to 0.7 ± 0.2 ms and 0.8 ± 0.2 ms which are still quite small compared to other

	large piezo	contact	contact & optical
samples	0 ± 2	5 ± 2	6 ± 1
ms	0 ± 0.2	0.7 ± 0.2	0.8 ± 0.2

Table 3.4: Results of the trigger test (June 11, 1999) showing the mean and standard deviation of pick times, in samples, for three different trigger types as compared to the results for the small piezo trigger.

sources of error in a seismic experiment. This source of error is easily avoided simply by being sure to use the same type of trigger throughout a survey. It is not necessary to use the same trigger type for all surveys because the phase velocities rely on relative timing within a single survey, not on absolute timing.

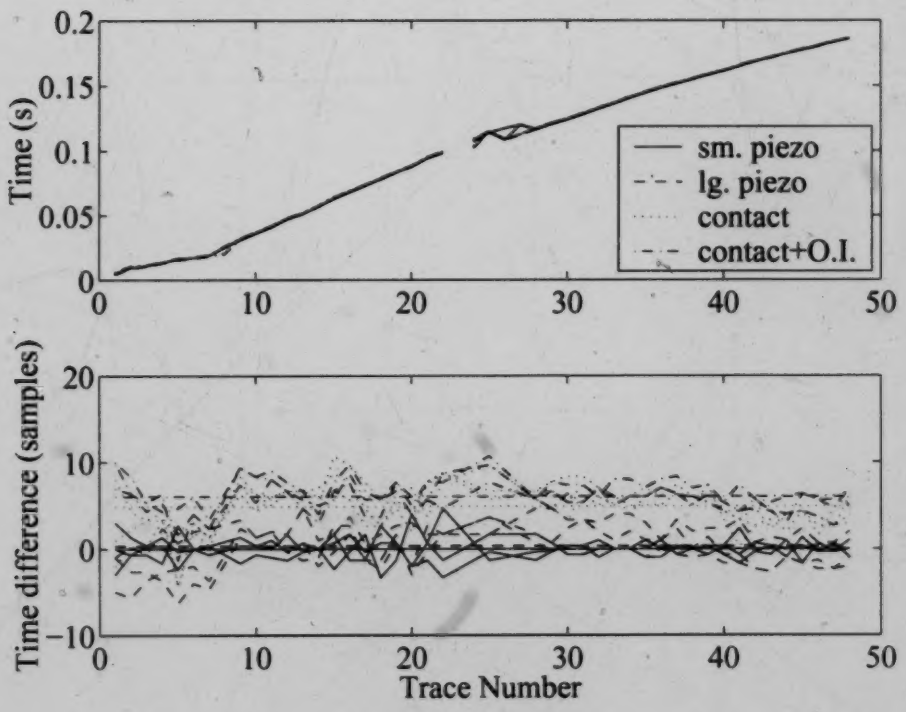

Figure 3.11: Results of the trigger test. Top - surface wave first break picks for each trace (three records per trigger type, one shot per record); bottom - difference between picks, in number of samples, with the results from the small piezo trigger used as a baseline. Mean values are displayed as flat lines. The legend applies to both plots where O.I. stands for 'optical isolater'.

Chapter 4

Study Site

The University of Alberta farm, also known as the Edmonton Research Station, was chosen as the site for this study. The site was chosen primarily for its simple geology (Kathol and McPherson, 1975) and easy accessibility. The site is located just south of the main campus within a 15 minute drive of the main campus. An aerial photo of the study site is shown in figure 4.1.

The geology of the Edmonton area has been mapped out fairly extensively. Around the farm area there is a layer of glacial lake sediments 5-10 m thick followed by a layer of glacial till 5-25 m thick, underlain by Cretaceous bedrock, including sandstone and shale. Three coal seams are shown under this area running through the Cretaceous bedrock, the shallowest of which is at about 30 m depth around the farm study site (Edmonton Geological Society, 1993).

A more detailed description of the geology of the area including a number of maps is contained in Kathol and McPherson (1975). The thickness of surficial deposits (any deposits above the bedrock, which is made up of interbedded shales and sandstones) in the study area is expected to be between 15 and 23 m. A geological cross-section of the area within a few city blocks of the study site indicates 10 m of lacustrine deposits, followed by 10 m of glacial till, underlain

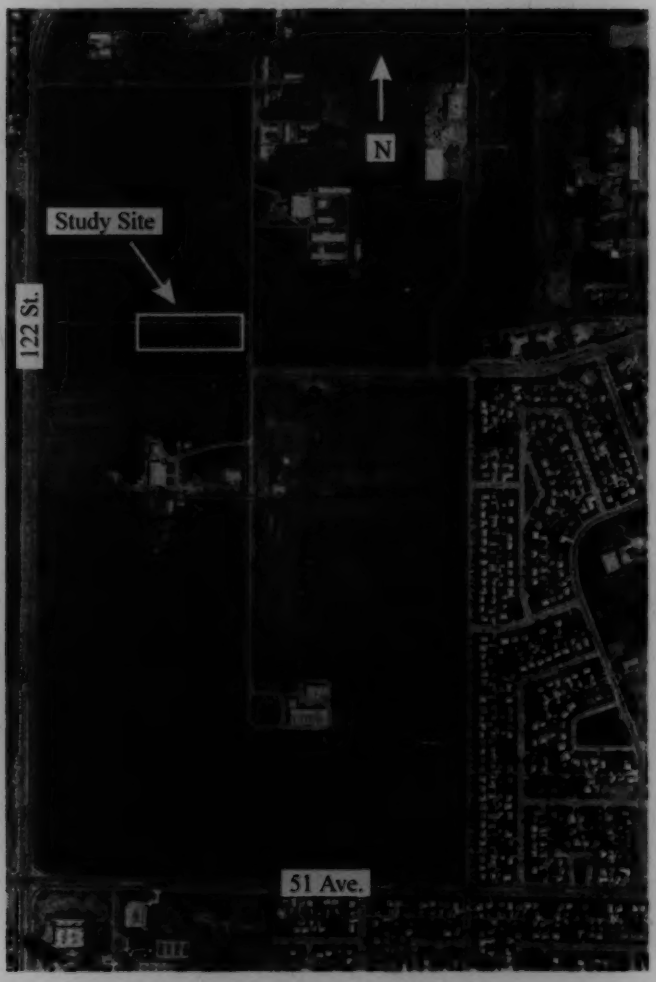

Figure 4.1: Aerial photograph of the University of Alberta Edmonton Research Station (courtesy of the Department of Agriculture, University of Alberta). This experiment was carried out on the west side of the farm, as marked.

by Cretaceous bedrock. The lacustrine deposits consist of mostly clays and silts deposited by Glacial Lake Edmonton. Glaciolacustrine sand and silty sand is present in scattered locations, generally in small pockets less than 1.5 m thick.

The glacial tills are unsorted, unstratified sediments deposited by a glacier composed of clay, silt and sand with pebbles, boulders and bits of coal. The bedrock is part of the Edmonton formation and is composed of interbedded shales and sandstones with numerous coal seams.

4.1 Site characterization

Soil coring, a vertical seismic profile (VSP), seismic refraction, DC resistivity and ground penetrating radar (GPR) were all used to provide additional information about the geophysical properties of the study site. The soil coring provided a geological profile as well as soil moisture and bulk density information, the later of which can be used as an input parameter in the inversion of surface wave dispersion curves. The VSP was used to obtain P- and S-wave velocity profiles which are useful as starting parameters for the inversion process as well as providing an independent measure for comparing the profiles determined through the surface wave dispersion curves. Refraction analysis of the seismic data allows another estimate of P-wave velocity to be made. A Schlumberger type DC resistivity survey and a ground penetrating radar survey were also carried out in order to gain an understanding of how resistivity changes with depth correspond to the changes in geology and moisture content. The GPR data can also be used to determine if the site is laterally homogeneous as assumed in the modelling.

4.1.1 Soil coring

The near surface geological profile was determined by soil coring at the University farm study site. The samples were also analyzed for moisture content and bulk density. Cores were taken using an auger drill rig (figure 4.2) with 1.5 foot (0.46 m) split spoon cores with a diameter of 3 inches (7.6 cm), shown in figure 4.3.

The coring was carried out by Mobile Augers. This provided cores of 1.5 foot (0.46 m) length separated by 1 foot (0.3 m) with samples taken in the 1 foot (0.3 m) interval directly off of the auger. Split spoon cores were obtained down to a depth of 9.8 m. Augering was continued down to 10.7 m and several samples were taken in this interval. These deeper samples off of the auger, however, likely contain some material from shallower depths so the results are less reliable. The hole was located at approximately the center of the seismic line.

Figure 4.2: An auger drill rig was used to obtain soil cores at the University of Alberta Edmonton Research Station (drilling done by Mobil Augers).

The near surface stratigraphy as determined from the core taken on site is given in table 4.1. The geology from this soil core agrees with the previously mentioned information on the geology of the Edmonton area (Kathol and M-

cPherson, 1975). The lacustrine deposits are slightly thinner than expected but only by 1.5 m. They had the consistency of plasticine and were easily molded and held their shape. The wet silty, sandy layer from 6.7 to 8.5 m may be indicative of a small sandy lens which is not uncommon for this area. The wet, sandy material was much weaker in character and it was difficult to keep this section of the core intact. The glacial tills, found at depths of 8.5 m and greater, were well consolidated and difficult to core because they were very hard. The depth to the water table was also measured directly after coring and was found to be 10.2 m. Two days later the water had risen to a depth of 7.6 m due to recharge. There was no precipitation during this period.

Bulk density, dry density and moisture content measurements were made on the core samples using standard techniques (Head, 1980). Core samples were carefully unwrapped on a flat surface. Every 1 to 3 feet (0.3 to 0.9 m) a sample approximately 2 cm thick was carefully cut from the cylindrical core. Vernier calipers were then used to measure the diameter and the thickness of each sample. Several readings were taken and averaged and then the volume was calculated

Figure 4.3: A soil core taken using a split spoon sampler.

Depth Range	Thickness	Geology
0-0.3 m	0.3 m	black top soil
0.3-1.5 m	1.2 m	gray and brown clay-like soil
1.5-6.7 m	5.2 m	clay, probably lacustrine deposits
6.7-8.5 m	1.8 m	very wet, sandy and silty soft clay
8.5-10+ m	1.5+ m	compacted glacial tills with pebbles, bits of coal

Table 4.1: Geology of the study site as determined from core samples.

($V = \pi z(d/2)^2$ where V is the volume, d is the sample diameter, and z is sample thickness).

Samples were places in clean, dry glass petri dishes with lids and then the mass of the each sample was determined using a balance. The masses were taken quickly as possible after sample preparation to minimize moisture loss. Samples were placed in an oven with the temperature held constant between 105 and 110°C until dry (this sometimes took as long as three days for some of the very moist clays). The oven used has a vacuum pump attached to it to draw moisture out of the oven so this was used during the last 6 to 8 hours of drying. Dry samples were cooled in a dessicator, which is a closed container containing a drying agent such as anhydrous silica gel. Once cool, the samples were covered and the masses were measured. Water is a naturally occurring part of the soil and clay structure (e.g. clay adsorption). The aim of oven drying is not to remove all of the water from the sample but rather to remove all of the water contained in the pore spaces in a standardized manner.

Bulk density is found by dividing the initial mass of the sample before drying by the volume of the sample. The samples for the most part held their shape and dried into hard, cracked disks. The dry density is the ratio of the mass of the sample after drying to its volume. Moisture content is the percentage of water

that can be removed from the soil pore space when dried at 105 - 110°C relative to the mass of the dry soil sample. The results of these measurements on the soil core obtained at the study site are shown in figure 4.4. Some of the samples were very friable making accurate volume determination difficult.

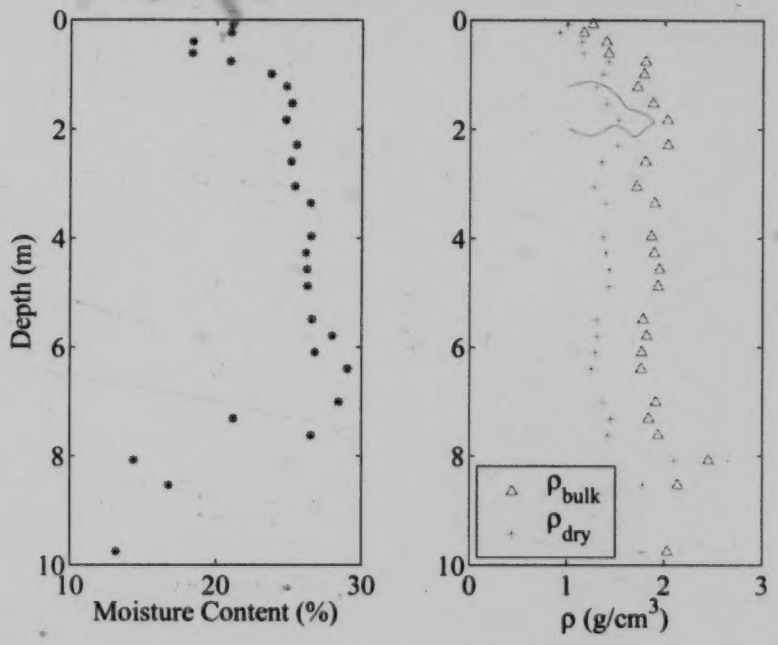

Figure 4.4: Soil moisture content and bulk density measurements from a soil core obtained on October 6, 1999.

4.1.2 Borehole seismic measurements

In the hole left from the soil coring, a vertical seismic profile (VSP) was conducted in order to gain an independent measure of *P*- and *S*-wave velocities with depth. Shallow vertical seismic profiles have been well established as a tool for determining near surface velocity profiles (Hunter et al., 1998; Xia et al., 1999a;

Xia et al., 1999b; Woods, 1994; Robertson and Fear, 1994).

The survey was conducted on October 6, 1999 using a three component geophone tool (containing 3 Mark Products L21 14 Hz geophones located at the bottom end; length of tool = 1.5 m). The sledge hammer was used as a source by pounding on an aluminum plate resting on the ground surface for generating *P*-waves, and resting on the vertical side of a hole approximately 30 cm deep as an *S*-wave source. The shot point was 0.36 m away from the center of the borehole. The top of the hole was stuffed with a rolled up foam pad to minimize noise from the air-wave. Measurements were made every 20 cm starting with the top of the tool at a depth of 7.0 m and ending with the top of the tool at the surface (geophones at 1.5 m). The data using the *S*-wave source came up only to 3.5 m due to technical problems (batteries wore out) and was quite noisy.

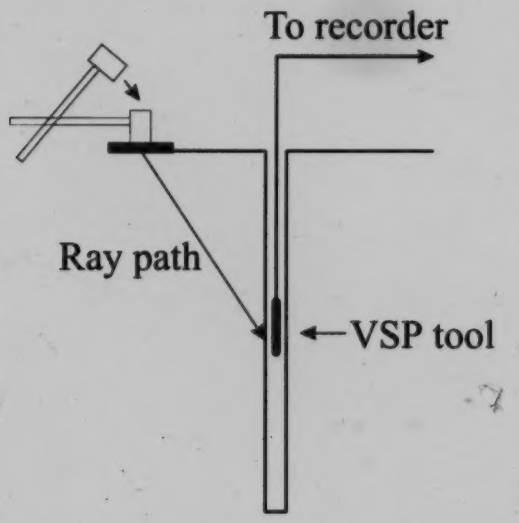

Figure 4.5: Geometry of the VSP survey performed at the Edmonton Research Station. A sledge hammer impacting on an aluminum plate was used as a source.

The full dataset obtained using the *P*-wave source, however, contained both *P*- and *S*-wave arrivals on the H1 component (figure 4.6). Comparison of the data recorded on the H1 component with the data recorded on the H2 component (figure 4.7) shows that most of the horizontal energy in the direct arrivals was in line with the direction of the H1 receiver. There is considerable scatter in the first arrival picks which can in part be attributed to error in the positioning of the tool but must be to a larger degree due to scattering and heterogeneities in the near-surface materials. Results from near the bottom of the borehole are less reliable as the depth measurements are less accurate here because the tool is raised up from the bottom of the hole so the initially the amount of cable passing through the depth encoder is probably greater than the distance traveled by the tool as the cable stretches out. There also may be error introduced if the tool was resting on the bottom of the hole.

The vertical component (figure 4.8) was extremely noisy making it impossible to obtain reliable picks so only the horizontal component was analyzed. The noise was likely due to oscillations of the cable set up by the wind. There is no borehole casing so nothing to clamp the cable to at the surface to damp the oscillations. This type of noise would affect the vertical component the most (L. Tober, private communication). Also, coupling of the tool to the soft material at the wellbore wall may not have been ideal.

Analysis of the *P*- and *S*-wave picks from the horizontal component was carried out first using a linear regression technique and second using a smooth inversion of the traveltime data (Lizarralde and Swift, 1999). The first method involves the examination of a plot of traveltime picks versus distance traveled and the determination of regions that could be approximated well by a line of constant slope. The slopes the best fit lines for the points in each of these regions were then found using linear regression and the velocities were taken as

the reciprocal of the slope. The linear regression fits are shown in figure 4.9. This analysis gave P-wave velocities of $\alpha = 488$ m/s between depths of 1.6 and 4.7 m and $\alpha = 1650$ m/s between 5 and 7.4 m. Regression analysis of the S-wave picks gave $\beta = 142$ m/s between 1.6 and 7.4 m and $\beta = 1040$ m/s between 7.4 and 8.8 m.

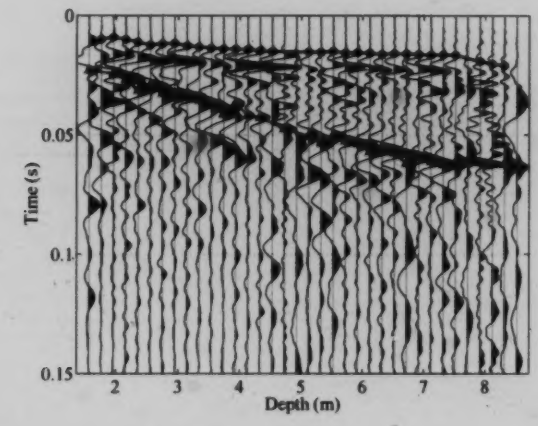

Figure 4.6: Component H1 of October 6, 1999 VSP survey at the Edmonton Research Station. P-wave picks are marked by circles and S-wave picks by triangles.

The smooth inversion of the VSP traveltime data was carried out using a damped, weighted least-squares inversion (Lizarralde and Swift, 1999). VSP first-arrival travel times can be obtained theoretically from the linear equation

$$\mathbf{t} = \underline{\mathbf{Z}}\mathbf{u} \tag{4.1}$$

where $\mathbf{t}$ is a column vector of first-arrival travel times for each depth, $\mathbf{u}$ is a column vector of interval slowness values (reciprocal of the average velocity in the interval between adjacent geophones), and $\underline{\mathbf{Z}}$ is a matrix of layer thicknesses (straight-ray paths are assumed i. e. ray bending due to changes in layer velocity

are not accounted for),

$$\underline{\mathbf{Z}} = \begin{bmatrix} z_1 & 0 & \cdots & 0 \\ z_1 & z_2 & & \vdots \\ \vdots & & \ddots & 0 \\ z_1 & z_2 & \cdots & z_M \end{bmatrix}. \tag{4.2}$$

The solution for interval slownesses is an even-determined problem with imprecise data so some form of regularization is required in order to get a meaningful solution. A damped, weighted least-squares approach is common. This approach yields a better solution in the presence of noise than a direct inversion would. For a damped, weighted least-squares inversion, a solution is sought to minimize

$$L = ||\mathbf{t} - \underline{\mathbf{Z}}\mathbf{u}|| + \varepsilon^2 ||\underline{\mathbf{D}}\mathbf{u}|| \tag{4.3}$$

where ε is a damping parameter, $\underline{\mathbf{D}}$ is a first or second difference matrix, and $\mathbf{u}$

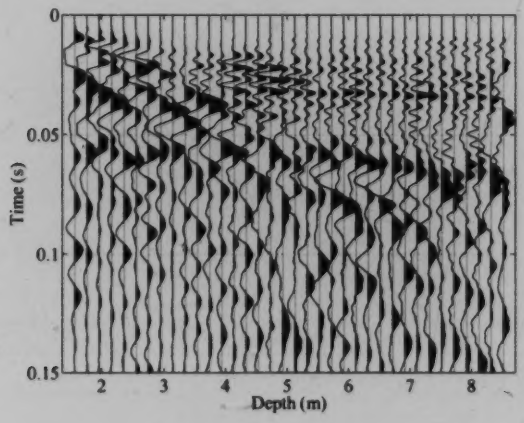

Figure 4.7: Component H2 of October 6, 1999 VSP survey at the Edmonton Research Station. Coherent *P*- and *S*-wave arrivals are much harder to pick out indicating that the majority of the horizontally propagating energy has been recorded on component H1.

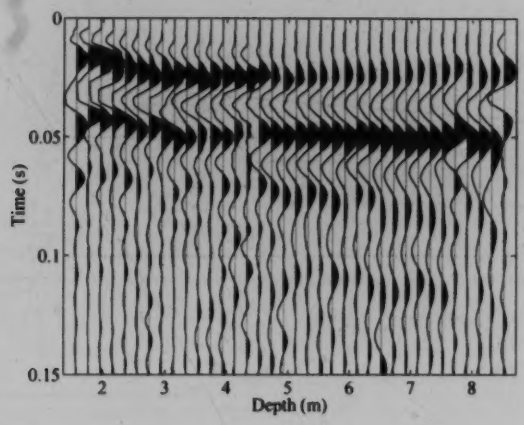

Figure 4.8: Vertical component of October 6, 1999 VSP survey at the Edmonton Research Station. Low frequency noise dominates the seismogram.

is now a matrix of estimated slownesses. For this study, $\underline{\mathbf{D}}$ was chosen as a first order difference matrix of size $M-1 \times M$. For example, for $M = 4$ $\underline{\mathbf{D}}$ would be

$$\underline{\mathbf{D}} = \begin{bmatrix} -1 & 1 & 0 & 0 \\ 0 & -1 & 1 & 0 \\ 0 & 0 & -1 & 1 \end{bmatrix} \tag{4.4}$$

A typical solution to (4.3) can be found in Menke (1984). One solution, including weighting according to data variance, is

$$\mathbf{u} = [\underline{\mathbf{Z}}^T \underline{\mathbf{W}}_e \underline{\mathbf{Z}} + \varepsilon^2 \underline{\mathbf{D}}^T \underline{\mathbf{D}}]^{-1} \underline{\mathbf{Z}}^T \underline{\mathbf{W}}_e \mathbf{t}. \tag{4.5}$$

The weighting matrix $\underline{\mathbf{W}}_e$ is a diagonal matrix of data variances. In assigning the data variances, factors such as the width of the first arrival peak, whether or not there were multiple modes in the peak, the noise level of the trace, and the coherence of the arrival with respect to the arrivals on other traces were considered.

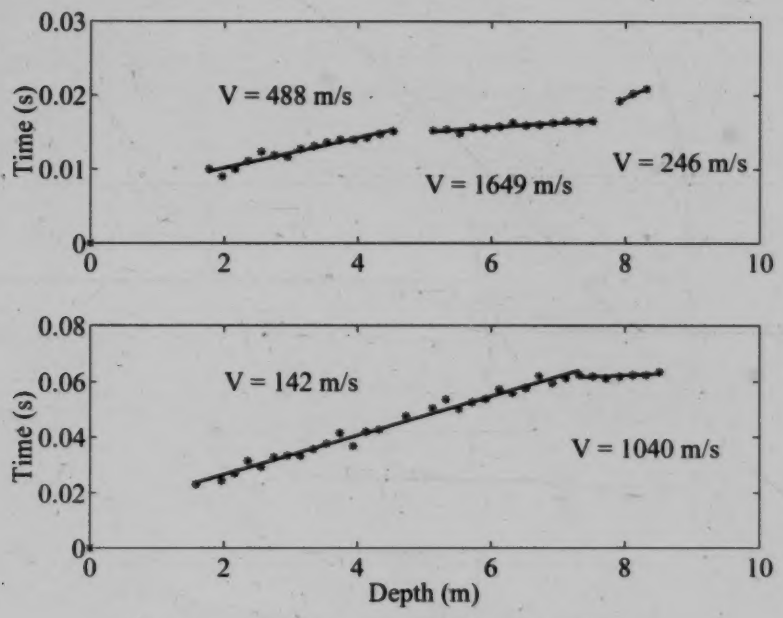

Figure 4.9: Regression analysis of the P- (top) and S-wave (bottom) first break picks from the October 6, 1999 VSP, component H1.

The magnitude of the damping parameter can be selected based on the reduced χ^2 statistical fit of the predicted data to the observed data where the χ^2 parameter is defined by

$$\chi^2 = \sum_{i=1}^{M} \frac{\left(t_i - \sum_{n=1}^{i} z_n u_n\right)^2}{s_i} \tag{4.6}$$

where s_i are variances for the measured travel times. An acceptable model should have $\chi^2 = M \pm (2M)^{(1/2)}$.

The results of the traveltime inversions for both P- and S-wave velocities are shown in figure 4.10 along with the regression analysis results. Figure 4.11 shows the traveltime picks (symbols) for both P- and S-wave direct arrivals along with the travel times predicted by the velocity profiles found through the inversions.

The inversion results compare fairly well with those of the regression analysis showing a smoother transition from slow to faster velocities with depth. This smooth nature of the transition is probably partially real and partially induced by the smoothness criterion imposed in the inversion process. Factors such as a smooth change in saturation in this zone, a gradient in the compaction of the clays, or changes in composition within the clay layer could cause a smoothing in the velocity profile. In the case of the *P*-wave profile the transition is much more gradual than that of the inverted *S*-wave profile so the smooth result is probably closer to the real velocity profile than the one determined from the linear regression technique.

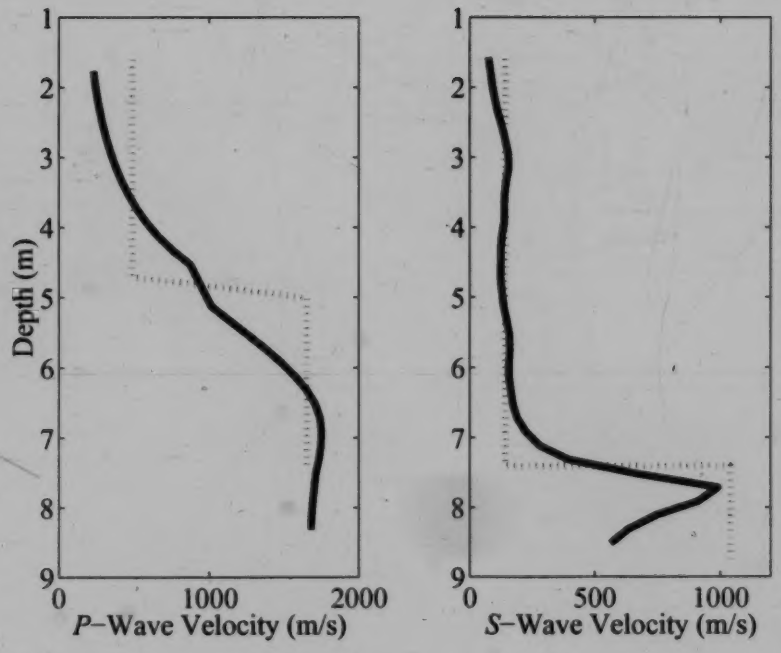

Figure 4.10: Inversion analysis (solid line) of the *P*- (left) and *S*-wave (right) first break picks from the October 6, 1999 VSP, component H1. The results from regression analysis on the VSP data are represented by the dotted lines.

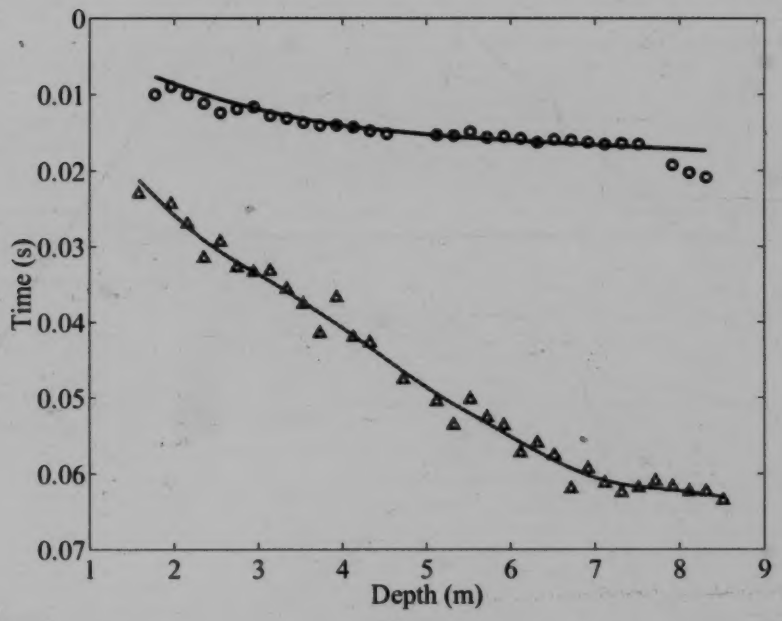

Figure 4.11: A comparison of traveltime picks with those estimated from the inversion results.

4.1.3 Seismic refraction analysis

The same seismic data that were obtained for surface wave dispersion analysis also provided another means of examining the shallow subsurface through standard refraction analysis. The close spacing of the geophones in the first 2 m (0.25 m spacing) provides good resolution of the speed of P-waves traveling in the top-most (also the slowest) layer. The data obtained on September 9, 1999 were chosen for refraction analysis because it was a relatively clean dataset with no bad traces on the vertical component. First break picks were made at the onset of first energy for each trace and then a basic refraction analysis was carried out. Assuming a set of flat, homogeneous layers, a plot of first break time versus offset distance can be fit with a set of straight lines, each representing the arrival returned from a layer. The slope of each straight line, determined using least-squares regression, is the inverse of the velocity of the layer, v_n. Thicknesses of the layers, h_n can be determined using the following standard relations

$$\begin{aligned} T_1 &= 0 \\ T_2 &= (2h_1 \cos\theta_{12})/v_1 \\ T_3 &= (2h_1 \cos\theta_{13})/v_1 + (2h_2 \cos\theta_{23})/v_2 \end{aligned} \tag{4.7}$$

where T_n are the intercept times and θ_{ij} are the angles that the ray that is critically refracted off of the j^{th} layer makes with the i^{th} interface. These angles are determined using Snell's law of refraction, $\sin\theta_{ij} = v_i/v_j$ where v_i and v_j are P-wave speeds in layers i and j respectively (Kearney and Brooks, 1995).

The linear fits to the first break picks from the September 9 dataset are shown in figure 4.12. A three layer model was used, giving the following P-wave velocity information:

v_1=185 m/s, h_1=0.81 m
v_2=468 m/s, h_2=1.14 m
v_3=1310 m/s.

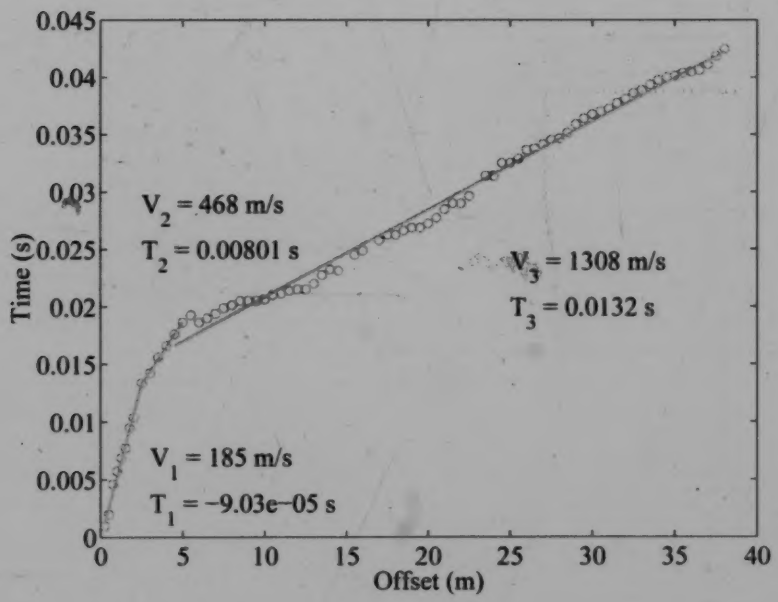

Figure 4.12: Refraction analysis on vertical component of September 9, 1999 data. The picks represent the onset of first energy.

These values fall within the *P*-wave velocity ranges for unconsolidated materials (top two layers) and clays (bottom layer) (Sharma, 1997). The refraction analysis provides information about the *P*-wave velocities in the top 1.5 m which are not available from the VSP data. If the VSP inversion curve could be simply extended to the surface then the refraction and VSP results would agree well in this region. The refraction and regression analysis of the VSP agree quite well at a depth of about 2 m. The refraction data, however, show an increase in velocity at a much shallower depth than the VSP results do and the maxi-

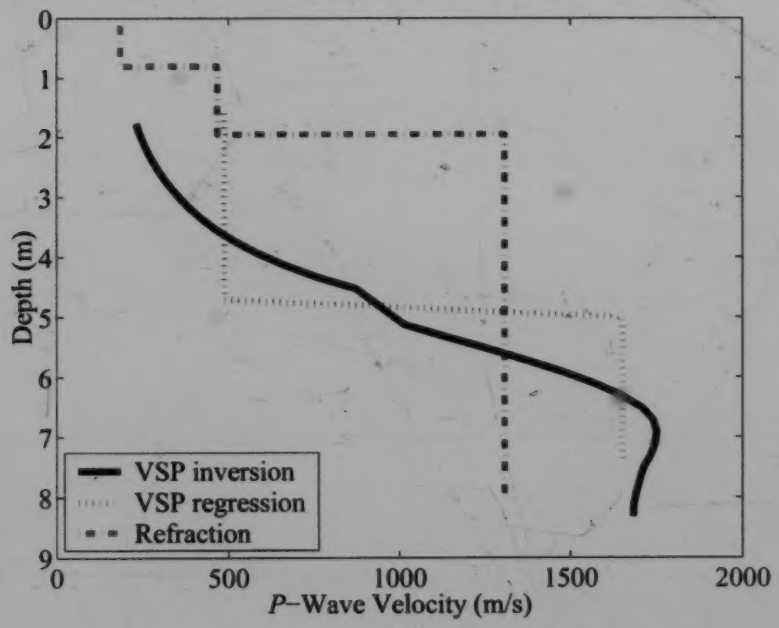

Figure 4.13: Comparison of *P*-wave velocities as determined by the VSP survey using regression analysis and inversion with those found by refraction analysis.

mum velocity reached is also smaller. One final point is that the VSP velocities are obtained from waves propagating vertically though the structure whereas the critically refracted arrivals in the refraction analysis are more indicative of horizontal wave propagation. These near-surface materials may be anisotropic, which could explain the differences in the two observations.

4.1.4 DC Resistivity

In a DC resistivity survey a current I is sent into the ground and the potential difference ΔV measured between two electrodes are used to find the apparent resistivity ρ_a of the earth. Ohm's law, $\Delta V = IR$, relates the current and potential difference to the resistance R of the electrical circuit configuration. The resistivity of a homogeneous earth is related to resistance by a geometrical factor of the electrode configuration used. The earth is in reality inhomogeneous, so the resistivity determined in this fashion is dubbed the apparent resistivity. Although this is called a 'DC resistivity' survey, in practice a low frequency AC (alternating current) source (less than 10 Hz) is often used. This eliminates the effects of polarization of the electrodes and telluric currents in the earth.

A Schlumberger type DC resistivity survey, which provides a vertical resistivity profile, was carried out on August 23, 1999 at the farm study site. A Schlumberger array has four electrodes with the distance between inner electrodes (MN) set up to be much smaller than the distance between outer electrodes (AB). A current is sent into the ground through outer electrodes and the potential is then measured between the inner electrodes. The array is symmetric about its centre. For this array type the apparent resistivity is given by:

$$\rho_a = \frac{\pi L^2}{2l}\left(\frac{\Delta V}{I}\right) \tag{4.8}$$

where L is half the distance between outer electrodes (L=AB/2), and l is half the distance between inner electrodes (l=MN/2) (Sharma, 1997; Telford et al., 1976).

The vertical electrical sounding survey technique is based on the idea that current penetrates deeper with increasing electrode separation. When the current electrodes are close together compared to the thickness of the top layer then the apparent resistivity will be very close to the resistivity of the top layer. At larger separations some of the current will travel through lower layers as well and

a smaller proportion will travel through the top layer. The penetration of the current depends on the power of the current source, near surface inhomogeneities, resistivity contrast between the layers, and electrical anisotropy within the layers (Sharma, 1997).

A vertical electrical sounding is performed in practice by setting up a Schlumberger array with small spacing (L=1 m and l=0.2 m were used in this survey to start). The inner electrodes are left in place while measurements are made with increasing L. When the voltage measured begins to be small compared to the noise then either the M and N electrodes can be moved further apart or the power can be increased (i.e. more current can be sent into the ground). Measurements were made out to an L of 50 m. Close to the end of the survey, l was increased to 2 m. Whenever the inner electrodes are moved, measurements for at least two L positions should be taken at each of the l spacings in order to later account for the effects of near-surface inhomogeneities. The data, corrected for changes in l, are shown in figure 4.14.

Most earth materials are fairly resistive with the exception of massive sulfides and graphite. Sandstones can have resistivities from 1-6.4$\times 10^8$ Ωm. Clays have resistivities between 1 and 100 Ωm and values for sands and alluvium range from 10 to 800 Ωm. Water greatly decreases resistivity, especially water of higher salinity (Telford et al., 1976).

Forward modelling will be performed on the data using a recurrence formula and linear filtering technique as described by Koefoed (1979). The general expression for the potential V over a series of horizontal layers is

$$V = \frac{I\rho_1}{2\pi} \int_0^\infty K(\lambda) J_0(\lambda r)\, d\lambda \tag{4.9}$$

where ρ_1 is the resistivity of the top layer, $J_0(\lambda r)$ is a Bessel function of order zero, K is a kernel function that depends only on the resistivities ρ_i and thicknesses h_i of the layers used in the model, and λ is a variable of integration with the

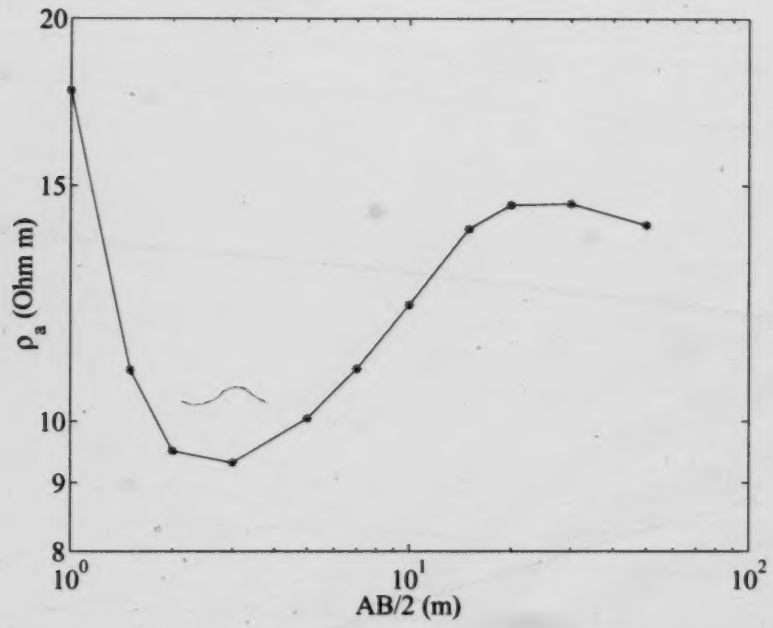

Figure 4.14: Apparent resistivity versus half the distance between outer electrodes for a Schlumberger DC resistivity survey carried out at the of Edmonton Research Station on August 23, 1999.

dimension of inverse length.

Most methods for determining the resistivity profile from a DC resistivity survey employ a resistivity transform function. The resistivity transform function $T(\lambda)$, which has the physical dimensions of resistivity (Ωm), is related to the kernel function through the following expression

$$T_i(\lambda) = \rho_i K(\lambda) \tag{4.10}$$

where ρ_i is the resistivity of layer i. The resistivity transform can be calculated efficiently using the recursive relation

$$T_i = [T_{i+1} + \rho_i \tanh(\lambda h_i)]/[1 + T_{i+1} \tanh(\lambda h_i)/\rho_i]. \tag{4.11}$$

For the nth layer, K can be shown to be equal to 1. The value of T_n can then be found and used as a starting point in the recursive calculation.

For a Schlumberger array configuration the apparent resistivity for the model can be found from the resistivity transform through the following relation

$$\rho_a = L^2 \int_0^\infty T(\lambda) J_1(\lambda L) \lambda d\lambda, \tag{4.12}$$

where $J_1(\lambda)$ is the first order Bessel function (Sharma, 1997). Alternately, Ghosh (1971) shows that a linear, moving average filter $f(k)$ can be used to obtain apparent resistivity from the resistivity transform as follows

$$\rho_a = \sum_{k=k_{min}}^{k_{max}} T(\lambda) f_k. \tag{4.13}$$

Filter coefficients can be found in Koefoed (1979). These equations were used to obtain the resistivity transform and the apparent resistivity.* The modelling technique outlined above assumes that all layers are horizontal.

Inversion of the resistivity data from this survey yielded the resistivity profile shown in the lower portion of figure 4.15. The apparent resistivities calculated from this profile match the data very well with an RMS misfit of 2.4% (top panel of figure 4.15). The resistivity profile has a thin (30 cm) layer of high resistivity right at the surface that corresponds to drier soils. Directly below this layer there is an extremely thin conductive layer which may indicate the presence of a small amount of water directly above the lacustrine deposits. These lacustrine deposits appear to be divided up into two layers of similar resistivities with the transition at a depth of about 2.8 m. This change in resistivity could be due to any number of factors including changes in water content, clay mineralogy or salinity.

*A computer program for performing the forward modelling and the inversion for a 1-D Schlumberger resistivity profile is available in Burger (1992).

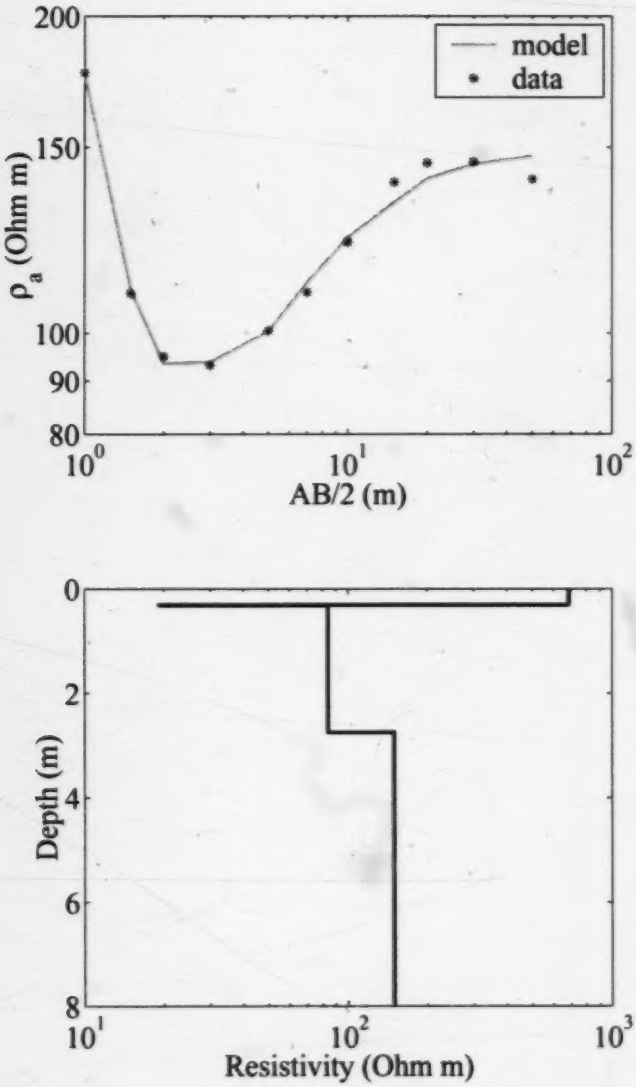

Figure 4.15: Top - a plot of apparent resistivity versus AB/2 showing data gathered August 23, 1999 and a model that fits very well. The resistivity depth profile used to generate this model is shown in the lower plot.

4.1.5 Ground penetrating radar

A ground penetrating radar (GPR) survey was carried out at the same site to look for heterogeneities at the site and to see if the soil profile matched that found through coring along the entire seismic line. A Sensors and Software GPR unit was used with 25 and 50 MHz antennae, which correspond to approximate depths of investigation of 30 and 10 m, respectively. The acquisition parameters used are summarized in table 4.2.

Antenna Frequency (MHz)	25	50
Sampling Rate (ps)	1600	3200
Step Size (m)	1	0.5
Antenna Separation (m)	4	2

Table 4.2: Acquisition parameters for the GPR survey.

The results of the ground penetrating radar survey carried out May 5, 2000 are shown in figure 4.16. The overall data quality is relatively poor for this survey. The clays in the area are relatively conductive, as seen in figure 4.15, which is likely one of the primary reasons for this poor data quality as the presence of conductive materials near the surface greatly decreases the effective penetration depth of GPR. Bandpass filters were applied to eliminate high and low frequency noise. Trim statics were also applied to align the direct arrivals more precisely. Deviations in the alignment are due to instrument drift and error in positioning of the antennae. Finally, an AGC (automatic gain control) was applied to boost the signal strength at later times.

The propagation velocity of radar waves in wet clay/silt is between 0.11 and 0.05 m/ns. In dry clay/silt the velocities are slightly higher (0.12 to 0.17 m/ns) (Sharma, 1997). Figure 4.17 shows the GPR data plotted as depth versus offset

where the conversion from time to depth has been carried out using a velocity v of 0.11 m/ns in the following formula

$$z = \frac{\sqrt{t^2v^2 - \Delta x^2}}{2} \tag{4.14}$$

where z is depth, t is time, and Δx is the distance between the transmitter and receiver. The depth to the air wave (first and most prominent arrival) is overestimated because this wave travels at a much higher speed of 0.3 m/ns.

For the 50 MHz data, two reflectors can be observed at 0.04 and 0.07 μs. At later times the data are too noisy to resolve deeper structure. Using the velocity range for wet clay, the depth to the top of the second layer (first reflection) was estimated to be between 0.2 and 2.0 m. The depth to the top of the next layer should be between 1.5 and 3.7 m. The resistivity structure determined from the DC resistivity survey shows layer boundaries that fall within each of these ranges.

The single observable reflection in the 25 MHz data is at 0.19 μs which corresponds to a depth of between 4.4 and 10 m. The DC resistivity data provided no information past about 4 m so a comparison cannot be made in this case. This reflection should correspond to the top of the glacial tills which is at about 8.5 m according to soil core analysis. Much better estimates of depth could be obtained if careful measurements of velocity had been made at the time. The most important result of this survey to note is that each of these reflectors is relatively flat. This lends validity to the assumption that the geology can be adequately represented using a set of laterally homogeneous horizontal layers which is made in the inversion of the surface wave dispersion curves.

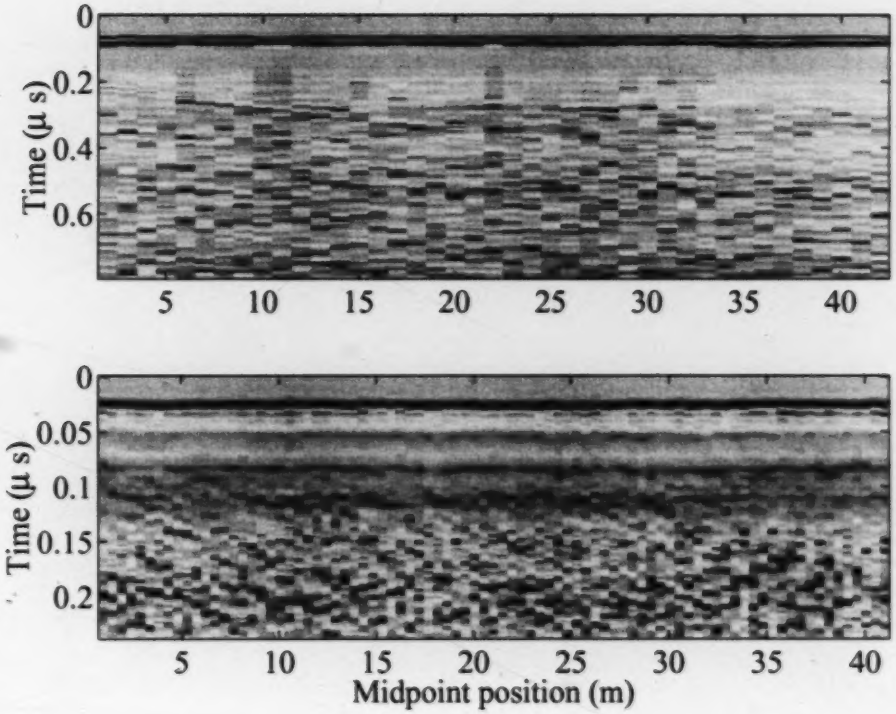

Figure 4.16: Processed GPR data obtained May 5, 2000 at the Edmonton Research Station. The top and bottom images show data obtained using the 25 MHz and 50 MHz antennae, respectively.

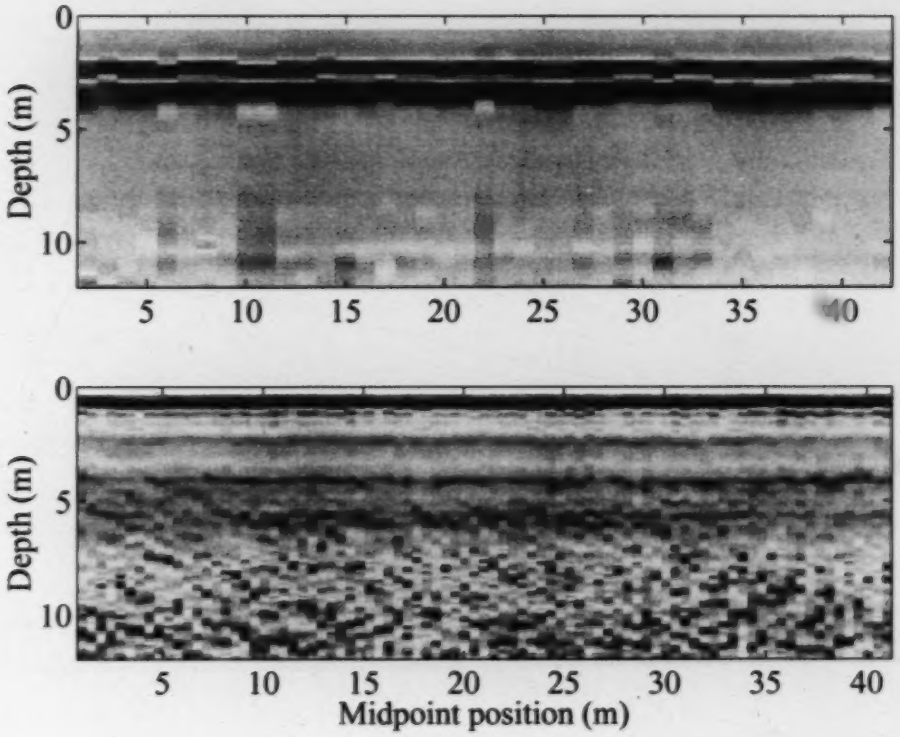

Figure 4.17: GPR data obtained May 5, 2000 at the Edmonton Research Station with the time scale converted to depth using a velocity of 0.11 m/ns. The top and bottom images show data obtained using the 25 MHz and 50 MHz antennae, respectively. Both use the same depth scale.

Chapter 5

Dispersion Analysis

5.1 Obtaining dispersion curves experimentally

Obtaining phase velocity dispersion curves from observed Rayleigh waves is a two step process. First the waves must be isolated from the other arrivals on the seismogram (Dziewonski and Hales, 1972). This can be achieved by windowing the surface wave data in either the offset-time ($x - t$) or frequency-wavenumber ($f - k$) domains if an array of geophones is used. Only the relevant data are retained. These windowing techniques will be compared later.

The second step is to extract the dispersion curves. This section will describe the various methods for finding dispersion curves from surface wave data. One method, used commonly in earthquake seismology, exploits the phase information of the Fourier transform of the surface wave. Other methods have been developed specifically for an array of multiple geophones. Fundamental and higher mode dispersion information can be obtained by locating peaks in the $f - k$ spectrum or else on the frequency-slowness ($f - p$) representation of the data.

5.1.1 Phase comparison methods for determining dispersion curves

A wave packet can be described as the superposition of a number of monofrequency plane waves, each of amplitude

$$A(x,t,\omega) = A_0(\omega)e^{i(Kx-\omega t+\phi_0(\omega))}, \tag{5.1}$$

where $A_0(\omega)$ is the maximum amplitude of the wave, $K(\omega) = k(\omega) + i\alpha(w)$, K is called a propagation constant , k is the real wavenumber (in rad/m) , α is the attenuation coefficient in units of length^{-1}, $\omega = 2\pi f$ where ω is the angular frequency and f is the frequency, and ϕ_0 is the initial phase of the wave. A band-limited wave packet $P(x,t)$ can then be described as a superposition,

$$P(x,t) = \int_{w_1}^{w_2} A(x,t,\omega)\, d\omega. \tag{5.2}$$

The phase velocity of the wave c is defined for each frequency as

$$c(\omega) = \frac{\omega(k)}{k}. \tag{5.3}$$

The phase velocity describes the speed at which the monofrequency components making up the wave packet travel. The group velocity, on the other hand, is often referred to as the energy velocity* because it describes the propagation velocity of the envelope of the wave packet, which contains the majority of the wave packet's energy. The group velocity U can be defined as

$$U(\omega) = \frac{d\omega}{dk(\omega)}. \tag{5.4}$$

*In a lossless homogeneous medium the group velocity and energy velocity, the velocity at which energy propagates, are identical. If the medium is not strongly dispersive then the group velocity may be considered to represent the velocity at which energy is propagated but this is not strictly true in general (Mavko et al., 1998).

Note that the phase velocity dispersion curve may be plotted as ω versus k, the local slope of which yields the group velocity directly.

The group and phase velocities can be determined using the unwrapped phase spectrum of the Fourier transform of a waveform (Molyneux and Schmitt, 2000). The unwrapping of the Fourier phase spectrum of a waveform can be achieved by changing absolute jumps greater than π to their 2π complement. The phase spectrum $\phi_1(\omega)$ observed at a distance x_1 measured along the shortest path along the surface between source and receiver is given by

$$\phi_1(\omega) = \frac{\omega x_1}{c(\omega)} + \phi_0(\omega), \tag{5.5}$$

where $\phi_0(\omega)$ is the phase spectrum of the source which unfortunately is often not known to great accuracy.

In practice it is possible in global seismology to obtain more accurate measurements of the velocities by comparing the phase spectra at two recording stations at different distances along the great circle path, or alternately, to compare two seismograms recorded at the same station – one of the event when it first is received and another of the event after it has traveled an additional full circle of the Earth (Toksöz and Anderson, 1966). In smaller scale surveys the phase spectra at two receiver locations in line with the source would be used. Phase velocity can then be expressed as

$$c(\omega) = \frac{\omega(x_2 - x_1)}{\Delta\phi(\omega)} = \frac{(x_2 - x_1)}{\Delta t_{phase}}, \tag{5.6}$$

where $\Delta\phi(\omega) = \phi_2(\omega) - \phi_1(\omega)$. The group velocity can be found using the slope of the $\Delta\phi(\omega)$ versus ω curve:

$$U(\omega) = \frac{x_2 - x_1}{\frac{d(\Delta\phi(\omega))}{d\omega}} = \frac{x_2 - x_1}{\Delta t_{group}}. \tag{5.7}$$

An alternative method to subtracting phase spectra is to exploit the properties of the cross-correlation operation, which corresponds to forming a signal

whose phase function corresponds directly to the difference between phases of the two original signals. For a discretized signal the cross-correlation of two signals G and H can be expressed in the time domain as

$$g_{GH}(\tau) = \sum_{k=-x}^{x} G_k H_{k+\tau}\, dt \tag{5.8}$$

where τ is the lag time, dt is the sampling rate, and x is the maximum lag time. One direct advantage of this method is that the time duration of the pertinent part of the cross-correlogram is always less than the full extent so it is possible to reject the unwanted portion to eliminate noise and increase the accuracy. The cleaner signal and the fact that there is only one phase spectrum that must be unwrapped also results in fewer errors due to the phase unwrapping process (sometimes it is difficult to determine exactly where factors of 2π must be added or subtracted). This is the method used in SASW surveys and in many earthquake seismology examples. Dziewonski and Hales (1972) provide a useful summary of this method and several others that have been used in earthquake seismology to obtain surface wave dispersion curves.

A comparison of the phase difference and cross-correlation methods applied to Rayleigh waves generated by the Rat Island event (21:44:17.2 GMT on 29 April 1963) is shown in figure 5.1. The dispersion curve found using the phase subtraction method is more erratic in nature with several large spikes that are likely due to phase unwrapping problems whereas the curve determined using the cross-correlation method is much smoother (Dziewonski et al., 1968). The cross-correlation method is generally the recommended technique for dispersion analysis of earthquake generate surface waves (Dziewonski and Hales, 1972).

The methods discussed above are most useful when surface wave modes can be easily separated and treated individually or else if the fundamental mode strongly dominates. Otherwise the resultant dispersion curve represents a weighted average of all of the modes which can be more difficult or impossible to interpret

using the methods above that are more fundamentally developed for a single discrete wavepacket with a unique single-valued phase velocity for each frequency. These methods were initially applied to the data obtained in this study under the naive assumption that the higher order modes were not important. The presence of multiple modes yielded poor results so the results of these earlier analyses will not be shown. Multichannel methods were found to be necessary to provide more detailed and reliable results in the context of near-surface studies.

5.1.2 Multi-channel methods for obtaining dispersion curves

There are several methods that have been developed for obtaining dispersion curves from multi-channel recordings of Rayleigh waves. One method involves first a Radon or $\tau - p$ transform on the data, followed by a one dimensional Fourier transform along the τ direction (McMechan and Yedlin, 1981). An example is shown in figure 5.2. This technique yields better results if the $\tau - p$ transform is performed in the frequency domain because interpolations that are necessary in the time domain can be achieved through the addition of a phase factor in frequency domain which is generally more accurate (see figure 5.3) (Park et al., 1998).

Another method, described by Gabriels et al. (1987), requires picking the peaks associated with surface wave energy in the $f - k$ domain. This method was also used by Nolet and Panza (1976) on recordings from an array of earthquake seismographs and by Yang et al. (1989) for a near-surface study. This method works on the principle that a point in $f - k$ space can be related directly to an apparent phase velocity through the relation $c = 2\pi f/k$. The group velocity would be the local slope of a line fit to the loci of phase velocities.

Both techniques were tested initially and it was determined that the while the results obtained from both agree well, the former provides better resolution

of the dispersion curves for this particular experiment. For the $f - k$ method, increasing the amount of zero padding around the data would help to improve the resolution but this requires the use of a large amount of memory.

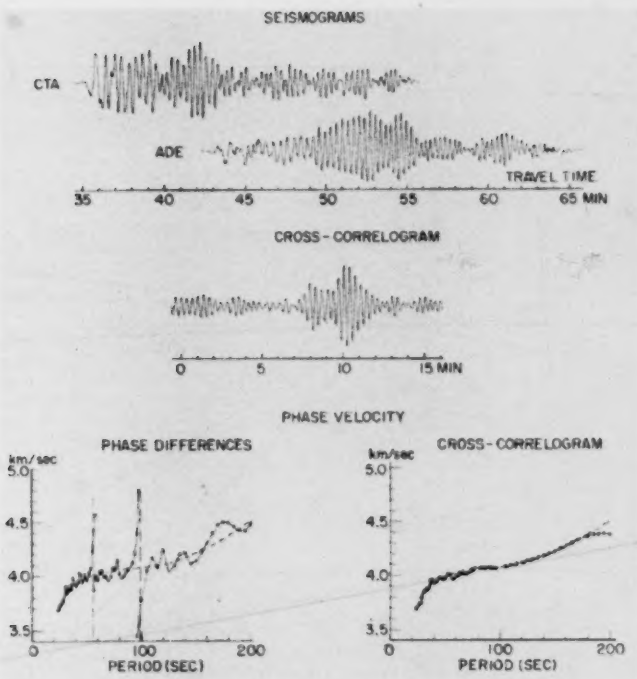

Figure 5.1: Seismograms (top) showing the Rayleigh wave, fundamental mode, for the Charter Towers-Adelaide path (epicentral distances of 8513 km and 10319 km, respectively) generated by the Rat Island event (21:44:17.2 GMT on 29 April 1963). Phase velocities calculated from the phase difference and cross-correlogram methods are shown (bottom). The dashed line represents a reference level (after Dziewonski et al., 1968).

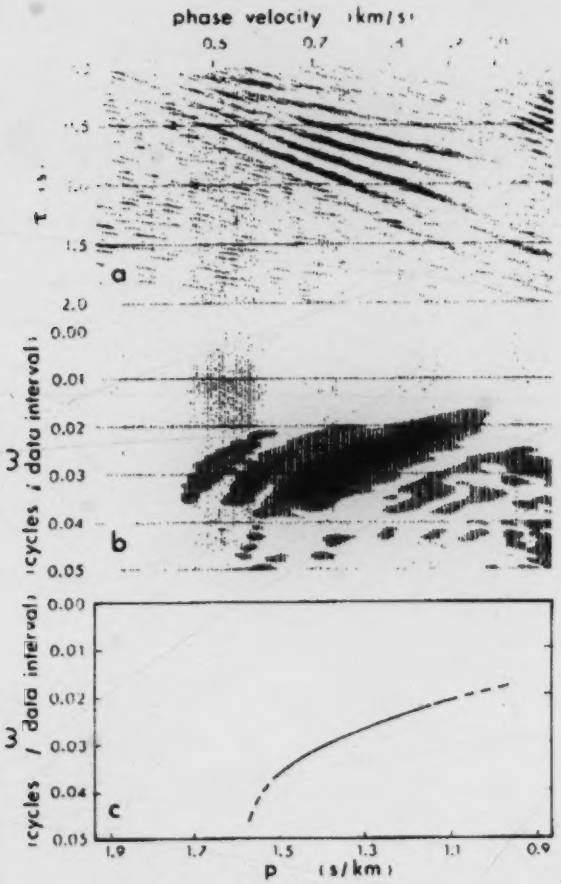

Figure 5.2: a) A slant-stack of a set of marine surface wave data is transformed into a $p-\omega$ images by taking the Fourier transform along the τ direction of the $\tau-p$ section. The locus of maximum amplitude in b) provides an estimate of the dispersion curve for the fundamental mode present in the data. Higher modes were not observed in this data set (after McMechan and Yedlin, 1981).

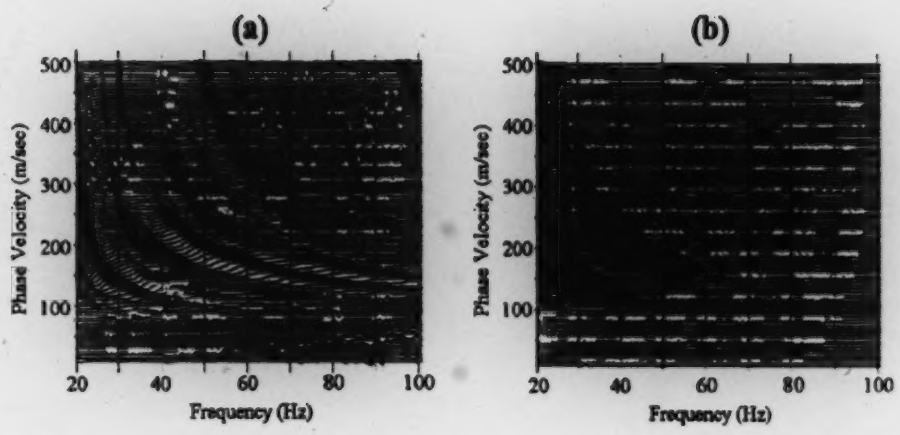

Figure 5.3: Figure comparing the phase velocity versus frequency representations of the same Rayleigh wave dataset using a) frequency domain methods and b) determination of the $\tau - p$ transform in the time domain. Note that interpolation has been performed to transform the data from representation in slowness to phase velocity (after Park et al., 1998).

5.1.3 Obtaining the $f-p$ section

Determination of the $\tau - p$ transform of a surface wave dataset is the first step in the method described in McMechan and Yedlin (1981) for obtaining dispersion curves from a multichannel seismogram. The slant stack or $\tau - p$ transform used for geophysical applications is a discretized version of the Radon transform. The Radon transform can be defined as (Radon, 1917) (English translation in Deans (1983))

$$m(p,\tau) = \int_{-\infty}^{\infty} d(x, t = \tau + px)dx \tag{5.9}$$

where τ is an intercept time and $p = 1/c$ is slowness or the inverse of velocity. This transform results in the integration of the amplitudes $d(x,t)$ along the straight line $t = \tau + px$ onto a single point (τ, p) in the $\tau - p$ domain. The discretized form of this transform is given in the following expression

$$m(p,\tau) = \sum_{i=1}^{N} d(x_i, t = \tau + px_i) \tag{5.10}$$

where x_i is the offset value for trace i and N is the number of seismic traces used in the $\tau - p$ transform. In practice, calculating the summation in (5.10) in the time domain requires interpolation which can introduce errors and is quite slow. This method is often referred to as a "slant stack" in the exploration geophysics literature (Gardner and Lu, 1991).

Similarly to (5.10), the data in the offset-time domain can be represented in terms of the data in the $\tau - p$ domain as

$$d(x_j, t) = \sum_{k=1}^{M} m(p_k, \tau = t - p_k x_j), j = 1, \ldots, N \tag{5.11}$$

where the seismic traces do not have to be regularly spaced and the slowness is discretized according to $p_k = p_0 + \Delta p(k-1)$ with $k = 1, \ldots, M$. Consequently, the $\tau - p$ transform is often used for purposes of interpolation where data may otherwise be lost or irregularly spaced in the $x - t$ domain.

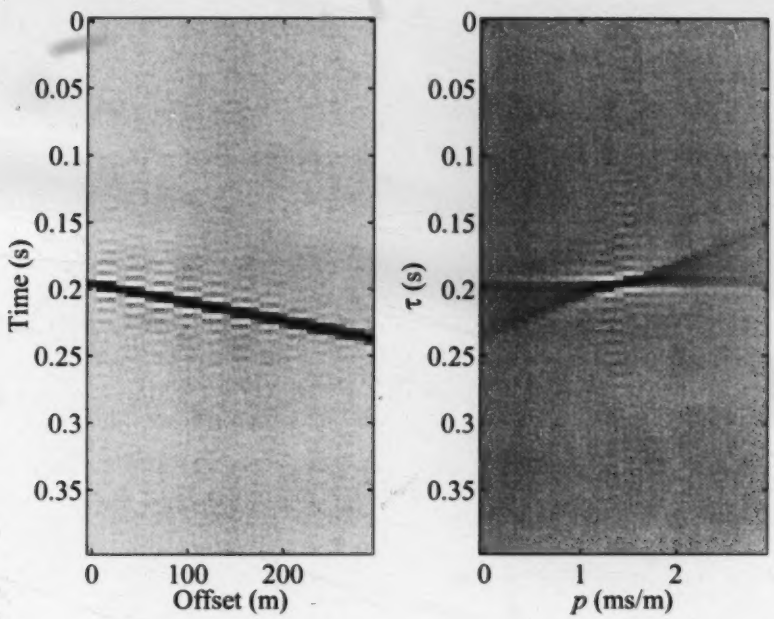

Figure 5.4: An arrival of constant velocity in the offset versus time domain will map onto a point in the $\tau - p$ domain given by its slope and zero offset intercept time.

A time shift Δt imposed on the data in the time domain is equivalent to multiplying the Fourier representation by a factor of $\exp(-i2\pi f \Delta t)$. This makes it possible to avoid the interpolations that are necessary when calculating the $\tau - p$ transform in the time domain by transforming the problem into the Fourier domain. The Fourier transform of (5.11) taken with respect to time can be written as

$$d(d_j, f) = \sum_{k=1}^{M} m(p_k, f) e^{i2\pi f p_k x_j}, j = 1, \ldots, N \tag{5.12}$$

In (5.12), each frequency can be treated independently. Equation (5.12) can be written in matrix form:

$$\mathbf{d}(f) = \underline{\mathbf{L}}(f)\mathbf{m}(f) \tag{5.13}$$

where $\mathbf{d}$ is a vector of length N containing Fourier coefficients for a given frequency for all of the seismic traces, $\mathbf{m}$ is a vector of length M containing amplitude information for all values of p at a given frequency, and $\underline{\mathbf{L}}$ is a $M \times N$ matrix defined by (Kostov, 1990)

$$\underline{\mathbf{L}} = \begin{pmatrix} e^{i2\pi f p_1 x_1} & \cdots & e^{i2\pi f p_1 x_N} \\ \vdots & \ddots & \vdots \\ e^{i2\pi f p_M x_1} & \cdots & e^{i2\pi f p_M x_N} \end{pmatrix}. \tag{5.14}$$

The least squares solution to (5.13) can be estimated through minimizing the cost function (Menke, 1984)

$$\phi = ||\mathbf{d} - \underline{\mathbf{L}}\mathbf{m}||^2 \tag{5.15}$$

which yields

$$\mathbf{m} = (\underline{\mathbf{L}}^T\underline{\mathbf{L}} + \mu\underline{\mathbf{I}})^{-1}\underline{\mathbf{L}}^T\mathbf{d} \tag{5.16}$$

where μ is a prewhitening parameter. If the matrix $\underline{\mathbf{L}}^T\underline{\mathbf{L}}$ is poorly conditioned, which is often the case, then the term $\mu\underline{\mathbf{I}}$, which serves to add noise along the diagonal of the matrix, will help to ensure the stability of the matrix inversion. The value selected for μ is usually a small percentage of the trace of $\underline{\mathbf{L}}^T\underline{\mathbf{L}}$. The full frequency-slowness representation or $f-p$ section can be constructed by calculating $\mathbf{m}$ for all frequencies of interest. This $f-p$ section is equivalent to taking the one dimensional Fourier transform along the τ direction of the Radon panel as described by McMechan and Yedlin (1981) but is computationally much faster and errors due to interpolation in the time domain are avoided. The $\tau-p$ section is obtained by taking the inverse Fourier transform along the τ direction. To go from the Radon panel back to an offset-time representation of the data equation (5.13) can be applied.*

*Matlab code is available for performing both the forward and reverse $\tau-p$ transforms (Sacchi, `http://rubble.phys.ualberta.ca/~sacchi/SEISMIC_LAB/`).

When performing a $\tau - p$ transform on a data set it is important to choose the values of τ and p so as to avoid creating an aliased representation of the data (Turner, 1990). Aliasing is a phenomenon that arises from undersampling with the result that high frequency components may appear in the data as low-frequency signals. Sampling in the τ direction should be chosen based on the same rules that govern time sampling of a time series. The required sampling rate in τ is

$$\Delta\tau \leq \frac{1}{2f_{max}} \tag{5.17}$$

where f_{max} is the maximum frequency present in the data. Aliasing in p results if more than one constructive summing direction is available on the $\tau - p$ section (figure 5.5). This can be avoided if Δp is chosen such that

$$\Delta p < \frac{1}{x_r f_{max}} \tag{5.18}$$

where x_r is the range of offset values.

Dispersion curves are obtained by picking the coherent peaks on the $f - p$ section and taking the inverse of the slowness p to obtain the Rayleigh wave phase velocity. Often multiple peaks are present at a given frequency indicating the presence of multiple Rayleigh modes. Figure 5.6 shows a typical $f - p$ section with three modes labelled.

A bootstrapping technique, a Monte Carlo method of estimating the standard error in a parameter found from an empirical dataset, can be used to find the error in the dispersion curves (Chernick, 1999; Efron and Tibishirani, 1993). This technique is implemented by taking a random set of seismic traces, constructing the $f - p$ map and estimating the location of the peak amplitude within the general region of each dispersion curve. The mean value and standard error associated with the dispersion curves can be determined by monitoring the location of the peaks over a number of iterations (on the order of 100). At each iteration

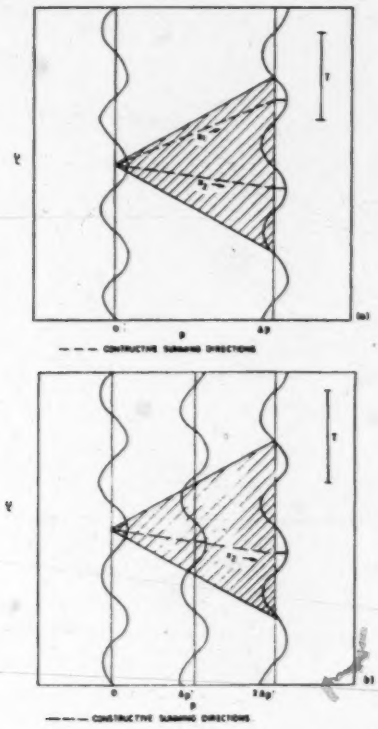

Figure 5.5: Closeup of $\tau - p$ data of a single frequency showing all of the possible directions of constructive summing within the range of offsets in the data (slopes in the $\tau - p$ domain) indicated by the shaded area. The $\tau - p$ section in a) has a spacing in p that would result in an aliased reconstruction of the data whereas b) has only one constructive summing direction (x_2) available and would result in the correct reconstruction of the data (after Turner, 1990).

a new random set of traces is used to reconstruct the $f - p$ section. A minimum error of half of the sampling interval in slowness should be imposed.

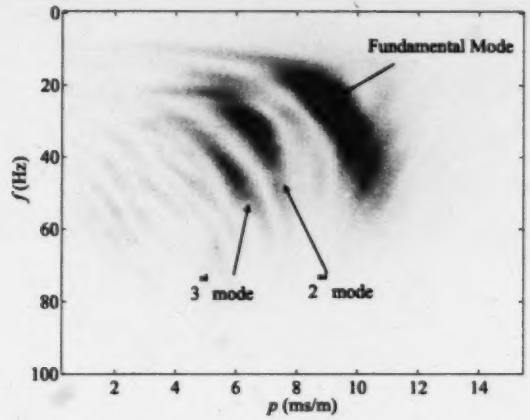

Figure 5.6: Typical $f - p$ section showing three Rayleigh wave modes.

5.2 Application of multichannel methods to the data

Both the $f - k$ and the $f - p$ methods for obtaining dispersion curves from multichannel methods, discussed in the previous section, were applied to the data recorded at the Edmonton Research station and compared. Prior to applying these methods it was necessary to isolate the surface wave arrivals on the seismogram and to scale the amplitudes of the traces.

Trace scaling was carried out by normalizing the data by the RMS amplitude of the traces, a scheme that is also known as energy balancing. The normalization factor for a given trace can be expressed as

$$A = \sqrt{\frac{\sum_{i=1}^{n} a_i^2}{n}} \tag{5.19}$$

where n is the number of points in the time series and a_i is the amplitude of point i. The normalization step attempts to account for geometrical spreading effects as well as variations in source strength and geophone coupling to the ground.

Prior to this step energy is only visible in the first few traces of the seismogram.

The purpose of windowing the data is to allow the processing to focus on only the surface wave signal. Two different techniques were used - windowing in the time domain, and windowing in the $f-k$ domain. The two windowing techniques were tested and compared in order to identify the superior method which was then used for the remainder of the analysis. The $f-p$ sections were computed for each data set and the dispersion curves have been assembled in order to make a comparison between study dates.

5.2.1 Comparison of the windowing methods

Two different windowing techniques were examined as potential methods for separating surface wave arrivals out from other arrivals in the seismic data. The first method involved isolating the Rayleigh waves using a $f-k$ filter. In the $f-k$ section of the September 9 data (figure 5.7) the surface wave energy is confined to the negative wavenumbers and in general they are found at lower frequencies than body wave arrivals for a given wavenumber. This property makes it possible to isolate the surface waves using a $f-k$ filter. Indeed, because they often lie in different regions of the $f-k$ plane than do more flat-lying reflection events, the $f-k$ transform is often used to filter out or attenuate the surface waves in reflection profiling.

One potential drawback to this method is that if there are any bad traces in the data set then this can introduce artifacts. It is also difficult to separate body and surface waves at smaller wavenumbers where the arrivals become very close together on the $f-k$ section.

The second windowing technique isolates the surface waves in the time domain. Times can be picked on each trace corresponding to the beginning and the end of the region occupied by surface waves. A tapered mute is then applied

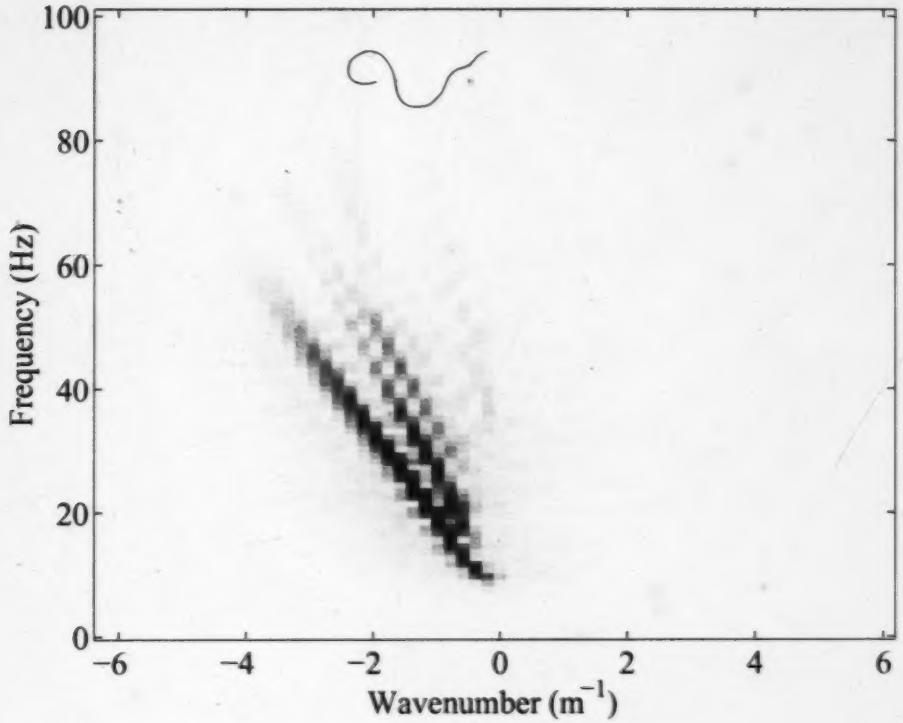

Figure 5.7: $F - k$ representation of data obtained September 9, 1999 before any windowing has been carried out. The brightest mode on the image is the fundamental Rayleigh wave mode.

to the data outside of the selected window. Applying a taper to the data, a Hanning window of 100 samples (12.5 ms) in this case, helps to avoid artifacts later when a Fourier transform is used.

The drawback of the time windowing method is that body wave reflections that are contained in the same time window are not removed, but since surface wave arrivals tend to be higher in amplitude than direct body waves the reflections, which will be even lower in amplitude, they should have only a small

effect.

The dispersion curves (fundamental modes only) for five surveys carried out on May 20, May 31, June 11, June 22, and September 9, 1999 were determined using data windowed in the $f-k$ domain(figure 5.8) and in the time domain (figure 5.9). Overall, the curves exhibit similar behaviour with the lowest velocities of about 95 m/s observed at mid-frequencies, slightly higher velocities at the highest frequencies, and a sharp increase in velocity near the low frequency cut-off. This sharp velocity increase is in good agreement with the abrupt change in the lithology at 8.5 m from clays to higher velocity compacted glacial tills.

The phase velocities at the low frequency limit show one of the key differences between the windowing methods. The dispersion curves found using data windowed in the $f-k$ domain show phase velocities at the low frequency end that are consistently as much as 25% (80 m/s) lower relative to dispersion curves obtained from traces windowed in the time domain. This discrepancy arises from the poorer sampling resolution and smearing of the low frequency data in the $f-k$ filtering technique.

Another discrepancy between the two windowing techniques is observed a the high frequency end. A 12% difference between May 20 and September 9 phase velocities is observed at the high frequency end of the spectrum (60-80 Hz) of figure 5.8 which is greater than the error in picking the dispersion curves from the $f-p$ map. According to a simple inversion scheme where the sensing depth is taken as 1/2 to 1/3 of the wavelength (Stokoe and Nazarian, 1985), this 12% difference would indicate a faster S-wave velocity in the top 1 m. Contrary to this result, figure 5.9 shows very good agreement between survey dates at high frequency for the surveys that contain sufficient energy at those frequencies suggesting that the faster velocity on May 20 is probably an artifact that could be caused by the presence of multiple bad traces in this data set.

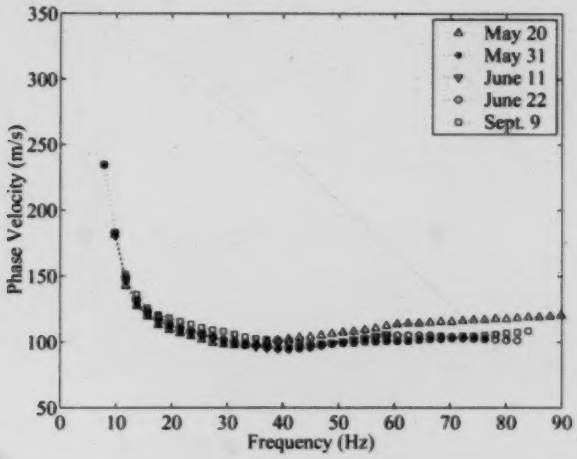

Figure 5.8: Dispersion curves obtained from data windowed in the $f-k$ domain taken at various times between May and September, 1999. Only the fundamental mode is shown.

The results from this investigation have shown that the time windowing method will provide more reliable results for this study. The remainder of the dispersion analysis will be carried out using this technique.

5.2.2 Comparison of the $f-p$ and $f-k$ methods

The goal of this section is to compare the $f-p$ and the $f-k$ methods for obtaining dispersion curves and to determine which method will be better suited for the purpose of this study. In order to make a valid comparison between the two methods a good data set is required. The vertical component of data obtained on September 9, 1999, windowed in the time domain, is shown in figure 5.10. This same dataset is also shown in figure 3.6 before windowing has been carried out. The time window used is displayed in the offset-time domain as well as the Fourier domain in figure 5.11. The power spectrum in figure 5.12 shows that

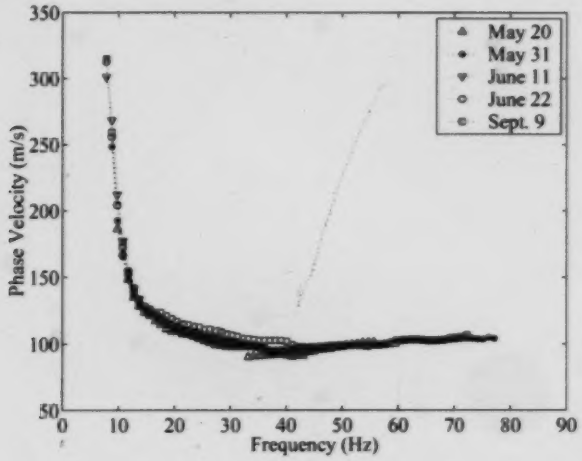

Figure 5.9: Dispersion curves obtained from data that were windowed in the time domain taken at various times between May and September, 1999. Only the fundamental mode is shown.

there is reliable energy between about 10 and 75 Hz in this experiment. The windowing process will have little effect on the frequencies in this range. As previously mentioned in chapter 3, these surface wave data were obtained using a receiver spacing Δx of 0.5 m from a near offset of 7 m out to a maximum offset of 38 m. This data set is very clean, meaning that it contains very little noise and has no bad traces, and was chosen as the data set to use for the comparison of the two methods for determining dispersion curves.

The first method for obtaining dispersion curves that was applied to the data was the $f-p$ method. The data were first decimated from 8192 to 1096 samples (from a sampling rate of 0.125 ms to 1 ms) to save on computation time. This reduces the Nyquist frequency f_{Ny}, the highest frequency that can be resolved by the data, to 500 Hz. The slowness parameters were chosen in such a way that phase velocities from as low as $c_{min} = 65$ m/s up to as high as $c_{max} = 3000$

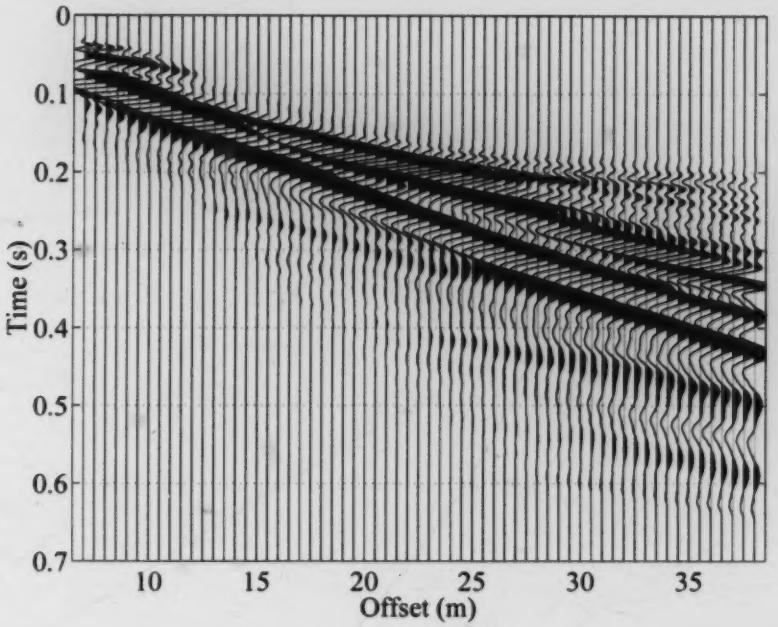

Figure 5.10: Seismic data showing strong surface waves (vertical component of the September 9, 1999 data set). Receiver spacing is 0.5 m and the minimum offset displayed is 7 m. The data have been windowed in the time domain to include only surface wave arrivals.

m/s could be obtained from the $f - p$ section. The spacing in slowness, Δp, was chosen to preserve frequencies up to at least 200 Hz without aliasing using Turner's formula (1990) $\Delta p < 1/x_r f_{max}$ where Δp is the p spacing, x_r is the range of offset values, and f_{max} is the maximum frequency in the data (equation 5.18). The Δp chosen was 0.15203 ms/m which yields 100 p values between $1/c_{min}$ and $1/c_{max}$. This choice is more than adequate as the power spectra of the data indicate that there is sufficient energy between about 5 Hz and 75 Hz in this experiment (figure 5.12).

Figure 5.13 shows the process of analysis applied to the September 9 data

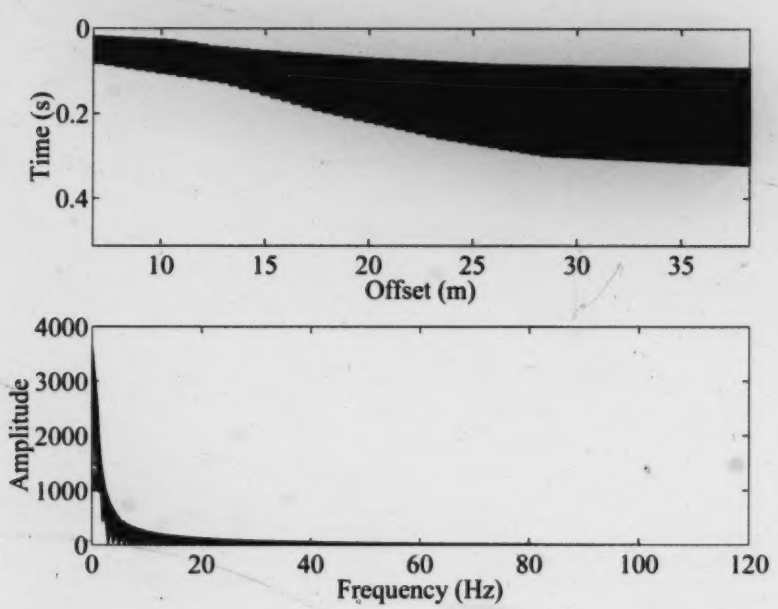

Figure 5.11: The time window applied to the September 9 data set (figure 5.10) shown in the offset-time domain (top) as well as in the Fourier domain (bottom). In the top panel, amplitudes range from 0 (white) to 1 (black). The windowing will have very little effect on the data in the frequency range of interest (about 10 to 75 Hz).

starting from windowed data in the $x-t$ domain, followed by the $\tau-p$ transform, the $f-p$ display and a reconstruction of the data from the $\tau-p$ section. The excellent match between the initial data and the data reconstructed from the $\tau-p$ section shows that the parameters used in the $\tau-p$ have preserved the information contained in the data well. Darker areas on the $f-p$ map indicate a concentration of energy related directly to the dispersion curves. In this case there are three strong modes evident, the strongest of which with the strongest slownesses is the fundamental mode.

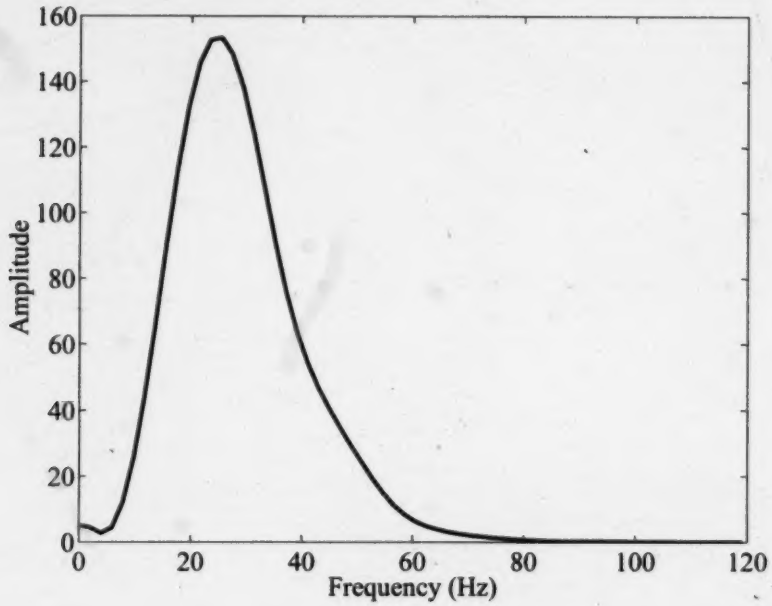

Figure 5.12: Average power spectrum of surface waves recorded September 9, 1999.

The second multichannel method for obtaining dispersion curves employs the $f-k$ transform. This method involves taking the two dimensional Fourier transform of the data and picking out the peaks in the frequency versus slowness domain that correspond to the fundamental and higher Rayleigh modes.

Choosing the appropriate parameters for the $f-k$ section is a standard procedure. The number of points used in f and in k is the next power of 2 up from the number of samples in time and the number of traces, respectively. This works out to 8192 points in f and 64 in k. Unlike the $f-p$ method, the data are required to be regularly sampled in both the space and time. The maximum frequency that can be resolved by the data, the Nyquist frequency, is $f_{Ny} = 1/(2\Delta t) = 4000$ Hz. The Nyquist wavenumber k_{Ny} is $\pi/\Delta x = 6.28$ m^{-1}.

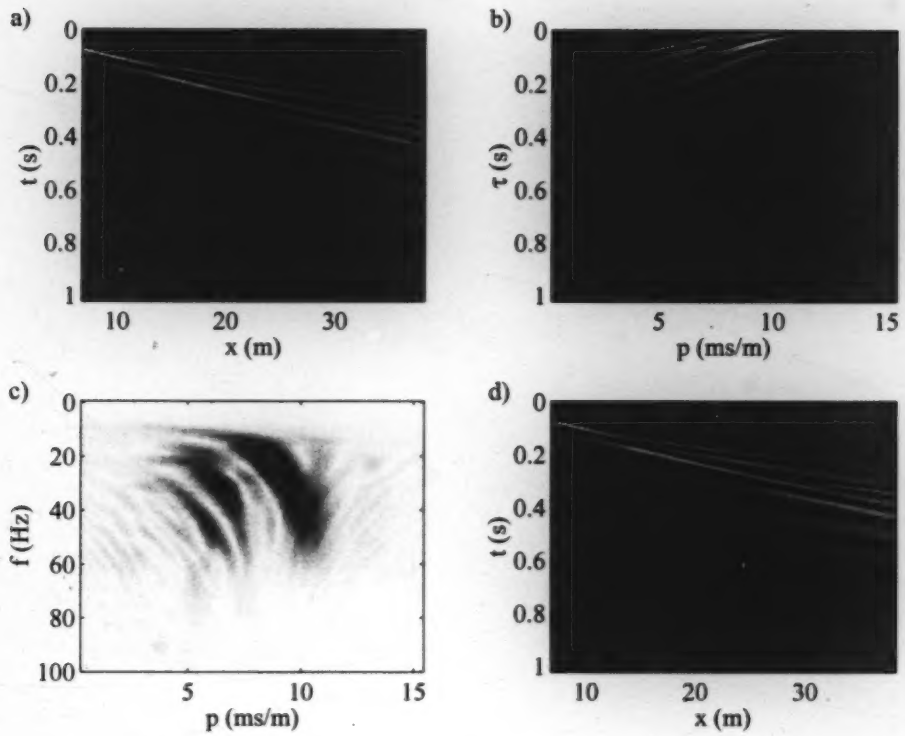

Figure 5.13: a) Seismic data recorded September 9, 1999 windowed in the time domain showing strong surface waves arrivals (vertical component). Receiver spacing is 0.5 m and the minimum offset displayed is 7 m. b) Slant stack of data. c) Map of frequency versus slowness where the dark peaks correspond to Rayleigh wave dispersion curves. d) Reconstruction of the data in the offset-time domain from the slant-stack representation.

The $f - k$ spectrum for the data obtained on September 9, 1999 is shown before and after windowing in the time domain has been carried out in figures 5.7 and 5.14, respectively. The brightest peak, which appears at the lowest frequencies, corresponds to the fundamental Rayleigh wave mode. The phase velocity c

of a Rayleigh mode can be determined by picking the frequencies and wavenumbers that corresponding to the peaks of the $f-k$ spectrum and applying the relation $c = 2\pi f/k$.

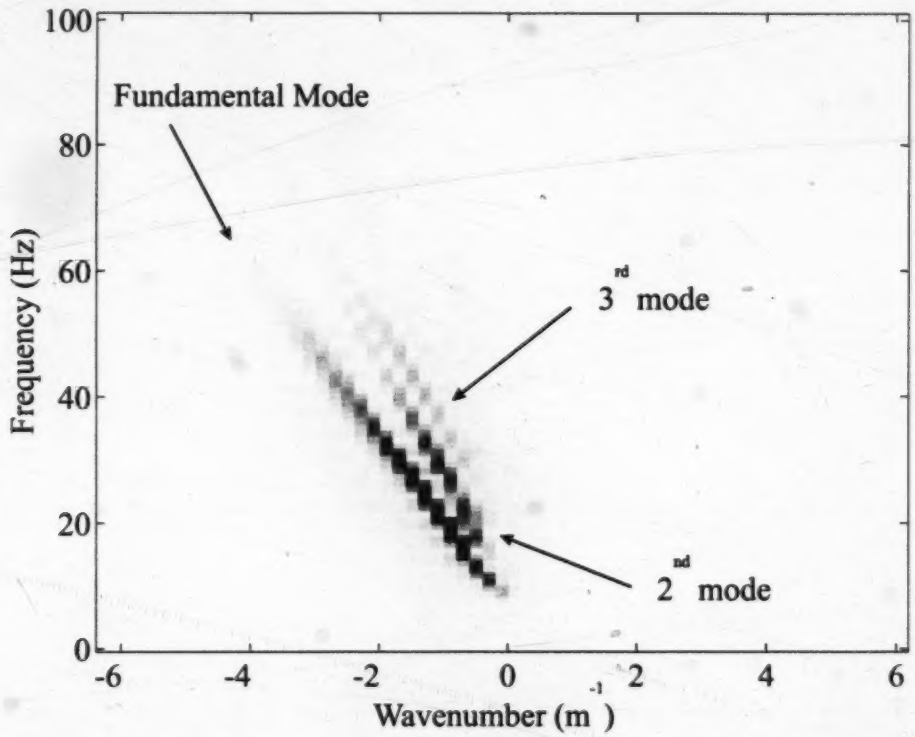

Figure 5.14: $F-k$ representation of data obtained September 9, 1999 which was first windowed in the time domain. Three distinct Rayleigh modes can be seen.

Dispersion curves obtained by applying both the $f-k$ and the $f-p$ methods to the September 9 data set are shown in figure 5.15. Three distinct modes are observed in both datasets with good agreement between the two methods, although the $f-p$ method provides better overall phase velocity resolution as compared to the $f-k$ section which looks noisier. The better resolution is

probably due to the Fourier interpolation carried out in constructing the $f-p$ image. This method, however, has the additional advantage that the data are not required to be evenly spaced so it is insensitive to dead traces on a seismogram.

There is a general trend of decreasing phase velocity with increasing frequency, indicating that materials closer to the surface have slower shear-wave velocities, as expected. The dispersion curve obtained using the $f-p$ method (the triangles connected by a solid line in figure 5.15) picks out what might be considered a best fit line to the dispersion points (the circles in figure 5.15) obtained using the $f-k$ method. This smooth curve obtained using the $f-p$ method provides a clearer, more realistic representation of the dispersion curve. Consequently the $f-p$ method was chosen as the preferred method to be used in carrying out the remainder of the dispersion analysis.

5.3 Vertical component dispersion analysis

Figures 5.16 and 5.17 show the $f-p$ images for the vertical component data from the 3-component 10 Hz geophones. The $f-p$ sections of the data recorded using the 14 Hz vertical geophones is shown in figure 5.18. It is clear that same three modes, displayed as black lines on the $f-p$ sections, are present in all cases.

When looking for changes in a property it is important to consider the uncertainty associated with that property. For dispersion curves, the uncertainty in both phase velocity and frequency should be considered. The independent treatment of the frequencies in the $f-p$ method ensures that the the frequency resolution, which is excellent to begin with because of high time sampling rates, is not effected by the transform (Park et al., 1998). The uncertainty in the frequency of the dispersion curve points is thus considered negligible.

Uncertainty in the phase velocity of the dispersion curves is related to the

width and coherence of a given band of amplitude related to a mode in the $f-p$ images (McMechan and Yedlin, 1981). A bootstrapping method was used to find the statistical uncertainty due to the coherency of the image. A minimum error of one half of the sampling rate in slowness was imposed because this is the limit on the accuracy to which a peak can be chosen. The width of the amplitude bands in the $f-p$ section is associated with the signature of the source. It is suggested that the width of these bands could be used as a measure of uncertainty in the dispersion curves (McMechan and Yedlin, 1981) but the method for determining the width was not described in detail so it has not been included as in the error bars displayed in these figures. A general idea of the magnitude of this source of uncertainty can be gained by examining the $f-p$ sections (figures 5.16 and 5.17).

May 20 and May 31 maps show comparable energy in all three modes but they also seem quite noisy as compared to some of the other sections. All of the $f-p$ sections obtained in June appear much cleaner but contain less energy in the higher modes than in the fundamental mode. July 14 shows a strengthening of the higher modes, the second more so than the third, and the sections for the remainder of the summer show strong primary and secondary modes as well with a weaker third. The September 9 data set contains by far the strongest and clearest signature in the high frequency range (above 30 Hz) as compared to all of the other datasets. The images for these dates are also much clearer (less noisy) than the ones from earlier in the season; this could be related to a change in soil conditions. The data set obtained in May of 2000 has a fundamental mode signature that looks similar to those found in late May/early June of the previous year and has a strong secondary mode similar to those found in May of the previous year but the tertiary mode is weaker compared to those of the previous May.

There are three possible reasons for the variations in image quality and char-

acter. It could be indicative of changes in the source strength which is a possibility when using a sledgehammer source. It could also be due to changes in how well the receivers were planted into the ground. Later in the summer, a hard layer developed at the top of the soil and it was difficult to plant the geophones well whereas in May the soil was much looser and quite moist so it tended to hold the geophones very well. The third possibility is that the attenuation properties of the near-surface materials was changing. This is the most interesting possibility of the three. It raises the question as to whether a surface wave dispersion study might be a viable technique for monitoring changes in attenuation in the near-surface.

Figure 5.19 shows the compilation of all of the fundamental mode picks for the vertical 10 Hz geophones. The secondary and tertiary modes are shown along with the fundamental mode in figure 5.20. The phase velocity dispersion curves agree well. The phase velocities are virtually identical for all of the surveys. The only significant difference between survey dates is the range of frequencies over which dispersion information is available.

The dispersion curves obtained using the 14 Hz vertical geophones looks quite similar and also show no phase velocity changes with survey date (figure 5.21). The August 6 data and the July 27 data deviate from the third mode curve around 47-55 Hz and 60 Hz respectively but this is caused by the picks jumping to a stronger peak on the $f - p$ section during the bootstrapping process and is not indicative of the behaviour of the third mode in these areas. Figure 5.22 shows that the general there is good agreement between the dispersion curves obtained from the 10 Hz and 14 Hz vertical geophone data.

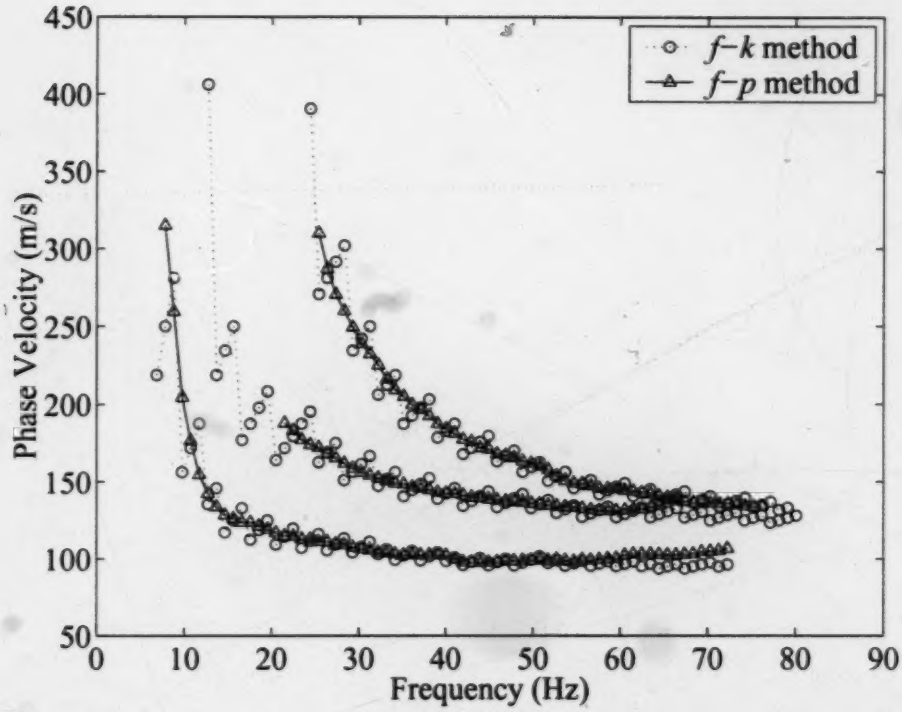

Figure 5.15: Dispersion curves obtained from surface wave data using the slant stack method on data windowed in the time domain (triangles connected with a solid line), and using the *f-k* method on data windowed in the time domain (circles connected with a dotted line). The fundamental mode is the lower-most, followed by the second and third modes having greater phase velocities.

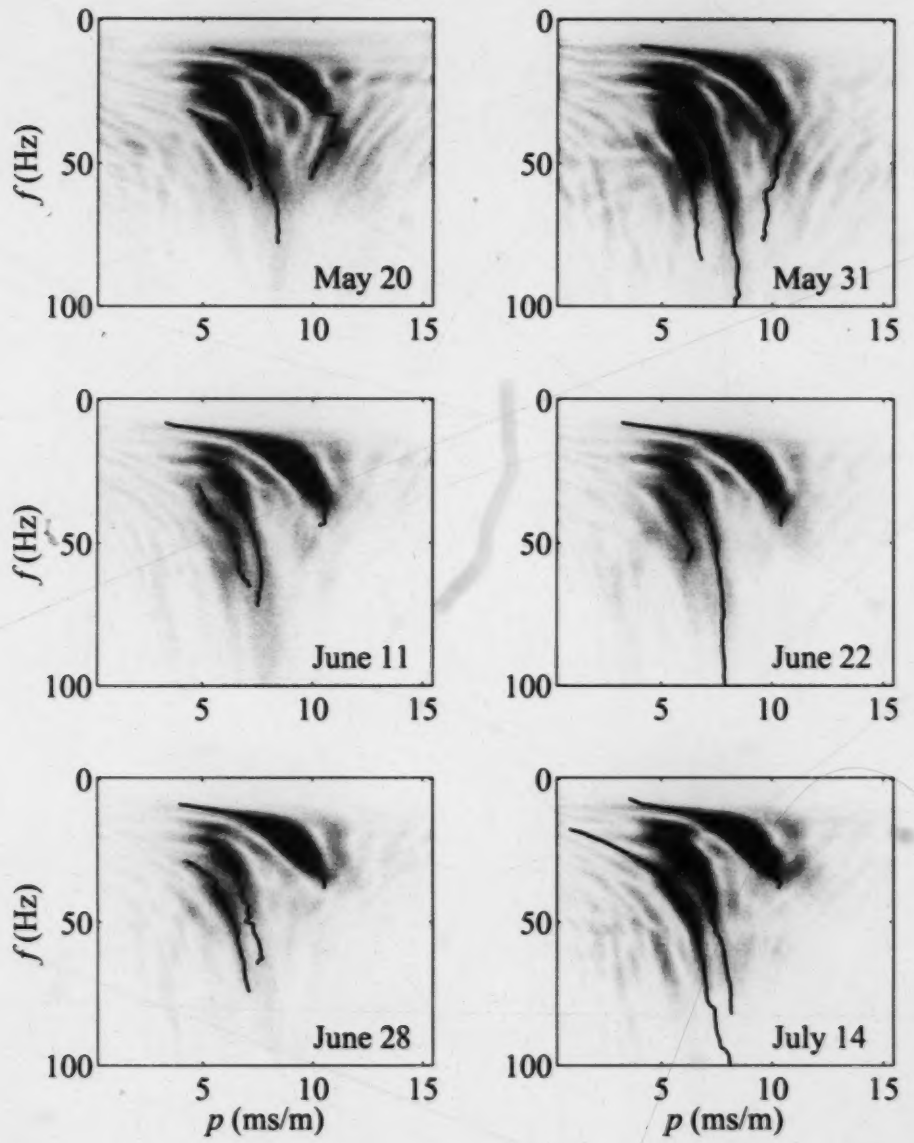

Figure 5.16: Frequency versus slowness sections for vertical component data (10 Hz geophones).

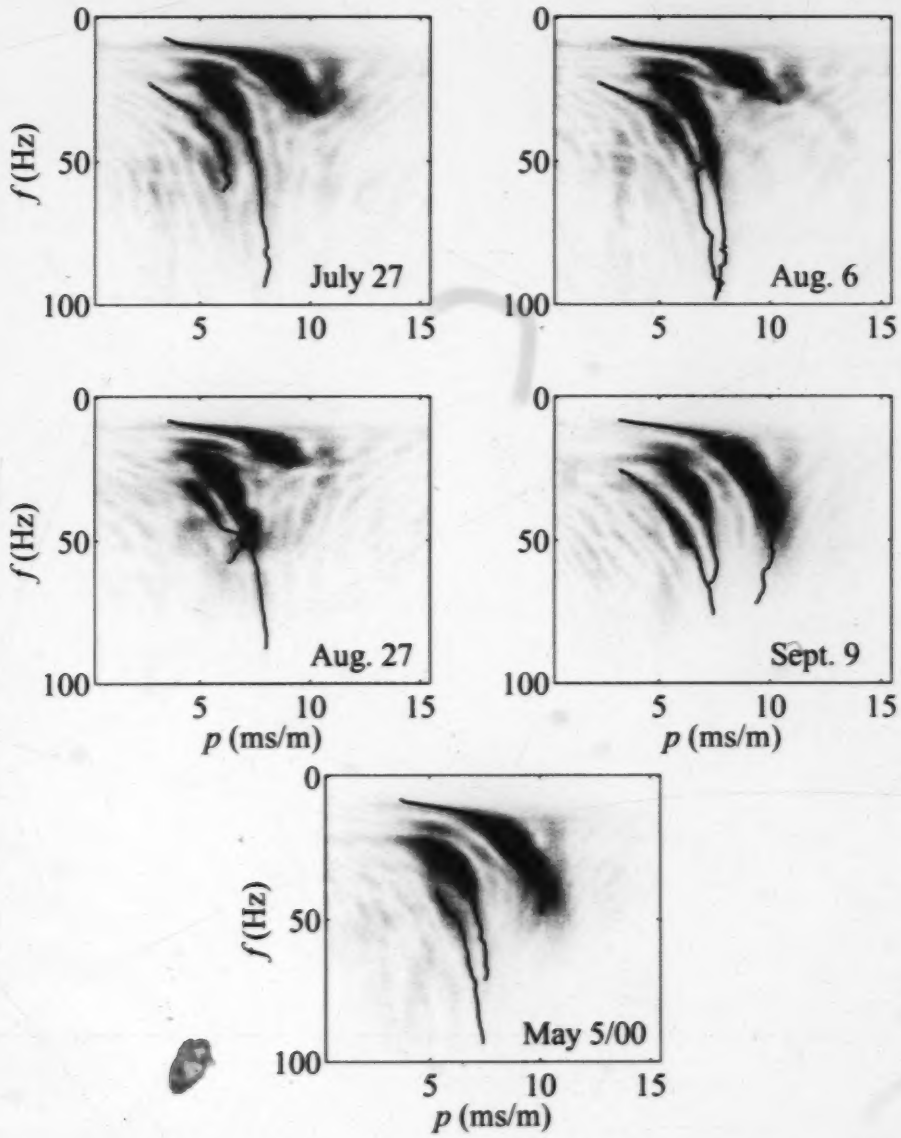

Figure 5.17: Frequency versus slowness sections for vertical component data (10 Hz geophones). In some cases, for example the May 20 fundamental mode, dispersion curve picks may have been influenced by artifacts in the image.

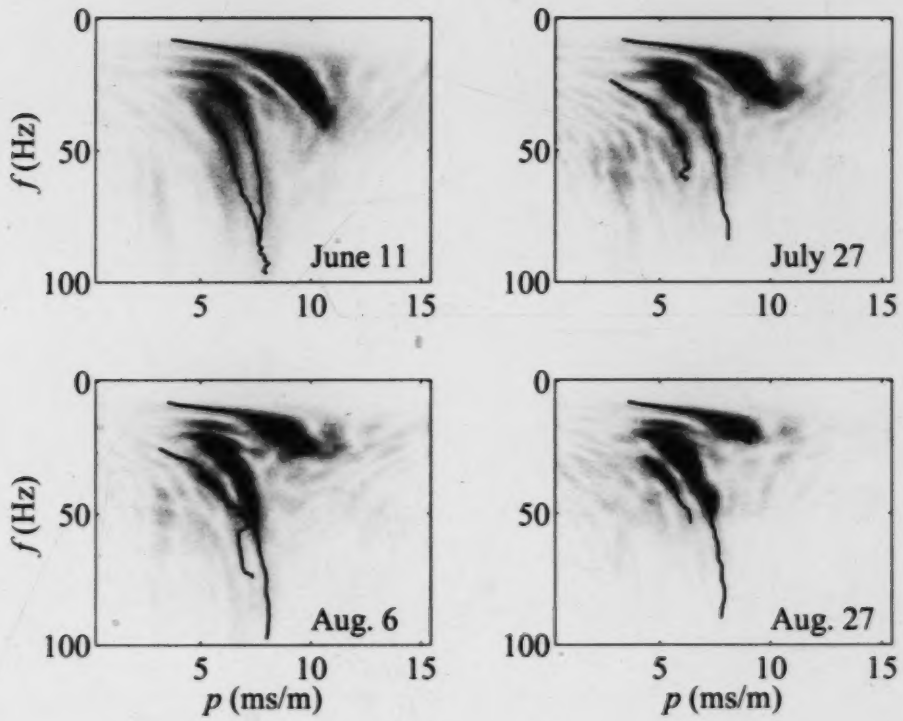

Figure 5.18: Frequency versus slowness sections for vertical component data (14 Hz geophones). Again there are a few cases, for example the third mode in the Aug. 27 section, where the dispersion curve picks may have been influenced by artifacts in the image or by proximity to another mode (second and third modes from Sept. 9 section).

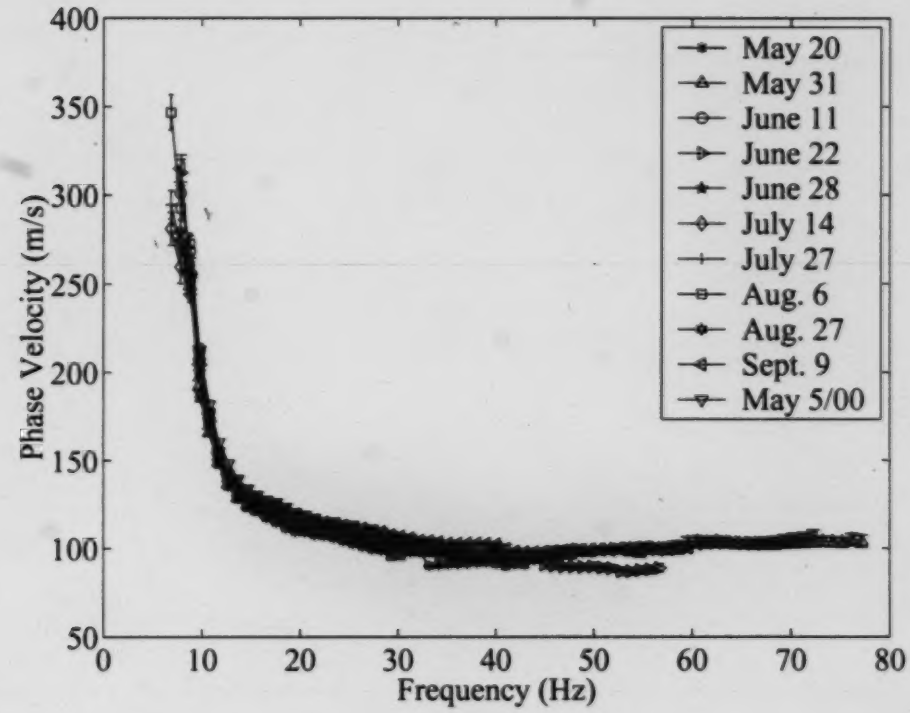

Figure 5.19: Phase velocity dispersion curves for Rayleigh waves recorded at the Edmonton Research Station (vertical component of 3-component 10 Hz geophones). Only the fundamental mode is shown.

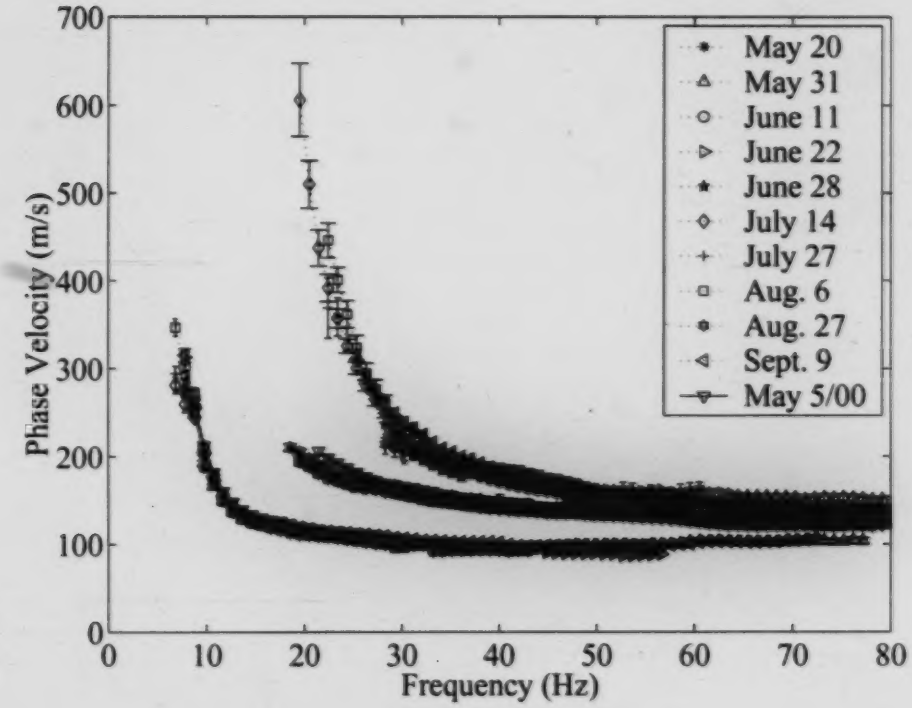

Figure 5.20: Phase velocity dispersion curves for Rayleigh waves recorded at the Edmonton Research Station (vertical component of 3-component 10 Hz geophones). All modes that were distinguishable in the data are shown.

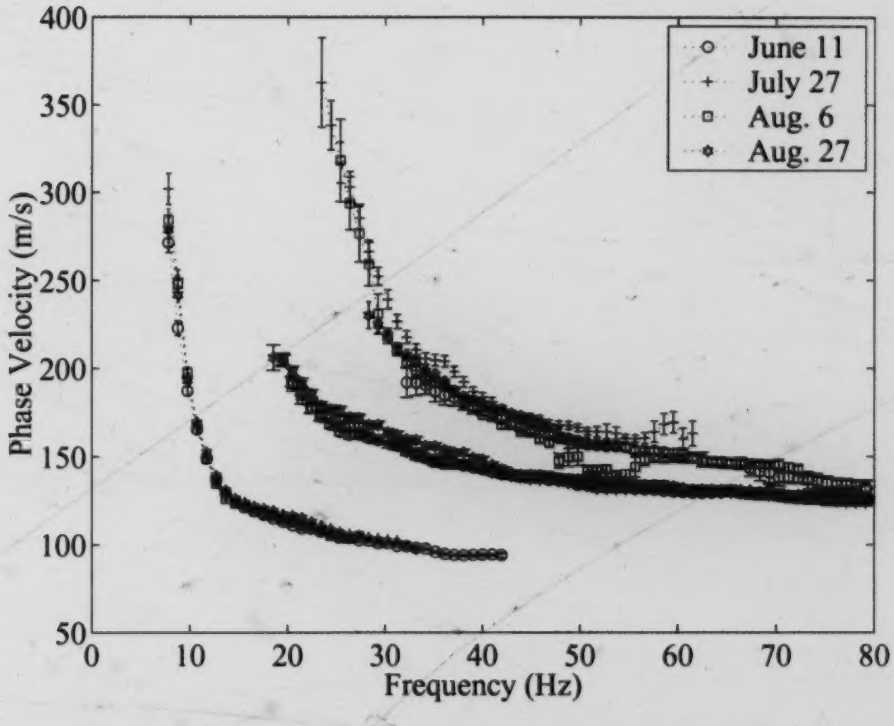

Figure 5.21: Phase velocity dispersion curves for Rayleigh waves recorded at the Edmonton Research Station (vertical 14 Hz geophones). All modes that were distinguishable in the data are shown.

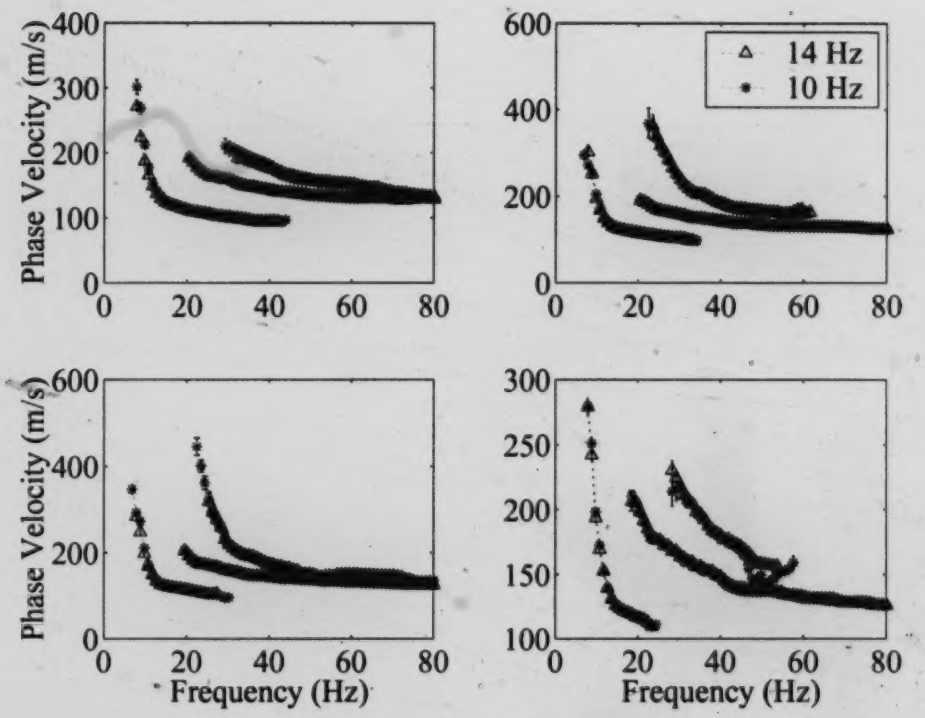

Figure 5.22: Phase velocity dispersion curves for Rayleigh waves recorded at the Edmonton Research Station (vertical component) showing data recorded on the same dates by both the 10 Hz and 14 Hz geophones. Survey dates were as follows: top left - June 11, 1999; top right - July 27, 1999; bottom left - August 6, 1999; bottom right - August 27, 1999.

5.4 Horizontal component dispersion analysis

5.4.1 Longitudinal horizontal component

The horizontal component of the data recorded using the 10 Hz 3-component geophones was analyzed in using the same parameters as the vertical component data. The $f-p$ sections of the horizontal longitudinal component look quite similar to the $f-p$ images created from the vertical component data except that they tend to lack the clear higher modes (figures 5.23 and 5.24). The black lines superimposed on the images represent the fundamental mode dispersion curves only. For the horizontal-transverse component this should be the fundamental Love wave mode and for the horizontal-longitudinal it represents the fundamental Rayleigh wave mode.

Most of the images contain a smearing of energy in the location where higher modes can be identified on the vertical component sections but coherent peaks are more difficult to identify except on a few sections. The June sections and the September section are quite clean with the majority of the energy contained in the fundamental mode. The May 5, 2000 section has a strong fundamental mode that extends to fairly high frequencies ($>$ 50 Hz) as does Sept. 9 and May 31 (although this section is much noisier). Once again, good agreement of the fundamental mode dispersion curves for all of the survey dates is observed (figure 5.25). These curves also agree well with the vertical component dispersion curves.

5.4.2 Transverse horizontal component

The transverse horizontal component are in general of poor quality due to the low amplitudes as might be expected (figures 5.26 and 5.27). Part of the reason for the poor data quality is that the Love waves are of lower amplitude than the

Rayleigh waves so if the receivers are not positioned properly there is a good chance that the small amount of Rayleigh wave energy detected because of the positioning will be strong enough to effect the Love wave data quality. Also, as noted earlier the geophones themselves are imperfect and would allow for some crosstalk between the different channels even if they were perfectly aligned.

The fundamental mode is difficult to pick out in most of the $f-p$ sections and tends to be identifiable over a much narrower frequency range than the dispersion curves on other components. The June data sets and the September 9 data set are the cleanest while those from later July and all of August are the least coherent. The agreement between the fundamental mode picks for all of the survey dates (figure 5.28) is surprisingly good considering the noisy attenuating appearance of these $f-p$ sections.

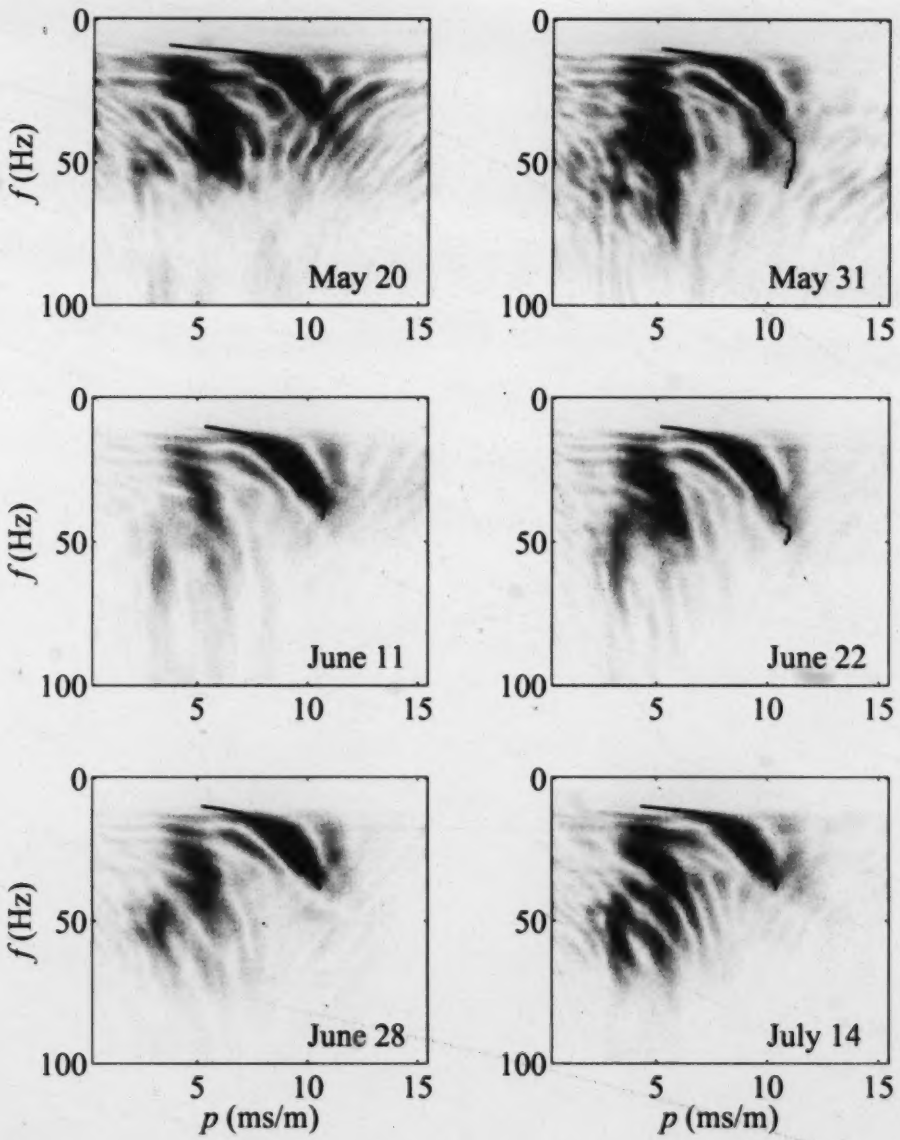

Figure 5.23: Frequency versus slowness sections for longitudinal horizontal component data (10 Hz geophones). The black line superimposed on the image represent the fundamental mode dispersion curve.

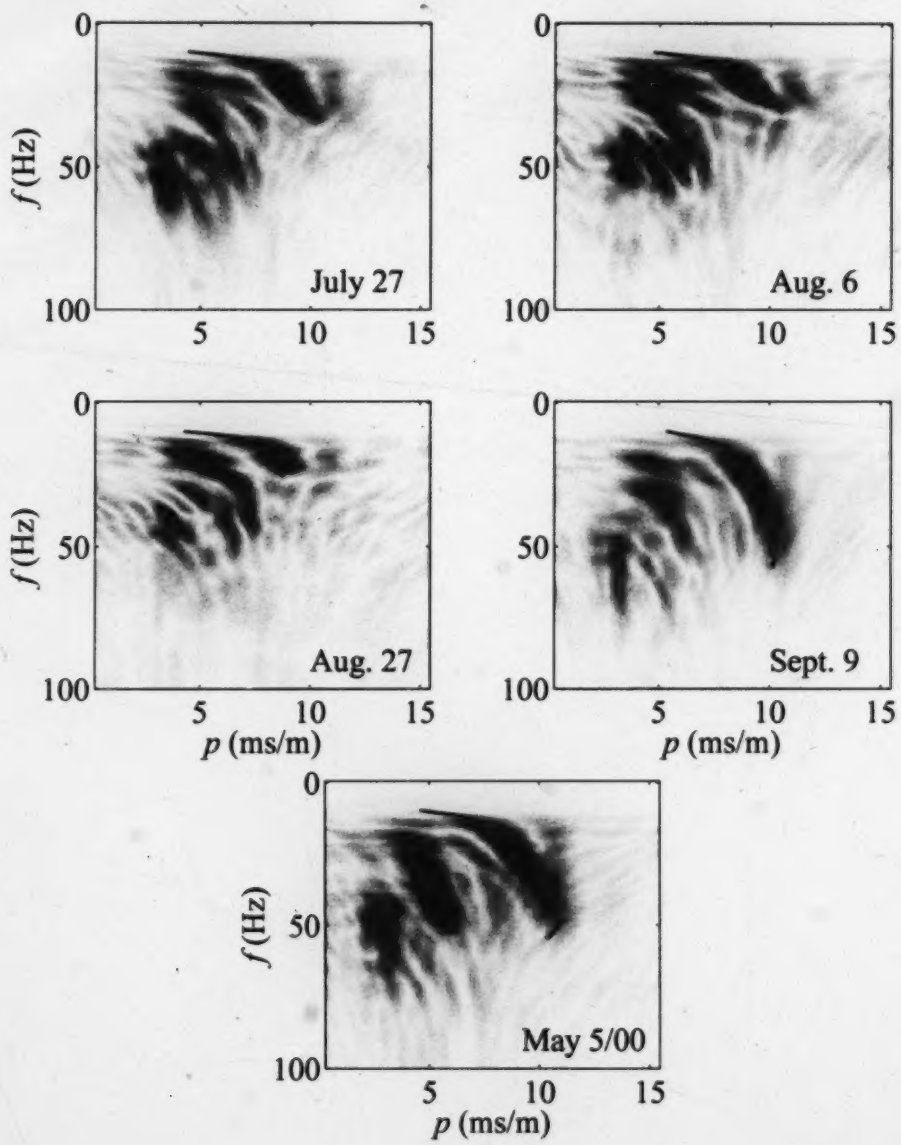

Figure 5.24: Frequency versus slowness sections for longitudinal horizontal component data (10 Hz geophones). The black line superimposed on the image represent the fundamental mode dispersion curve.

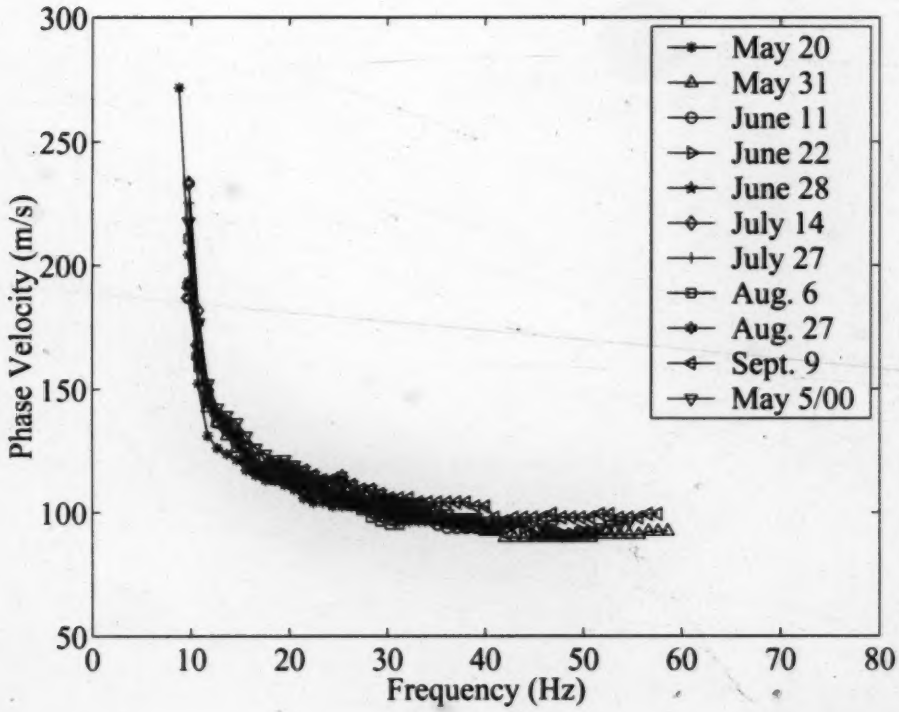

Figure 5.25: Phase velocity dispersion curves for Rayleigh waves recorded at the Edmonton Research Station (horizontal-longitudinal component of 3-component 10 Hz geophones). Only the fundamental mode is shown.

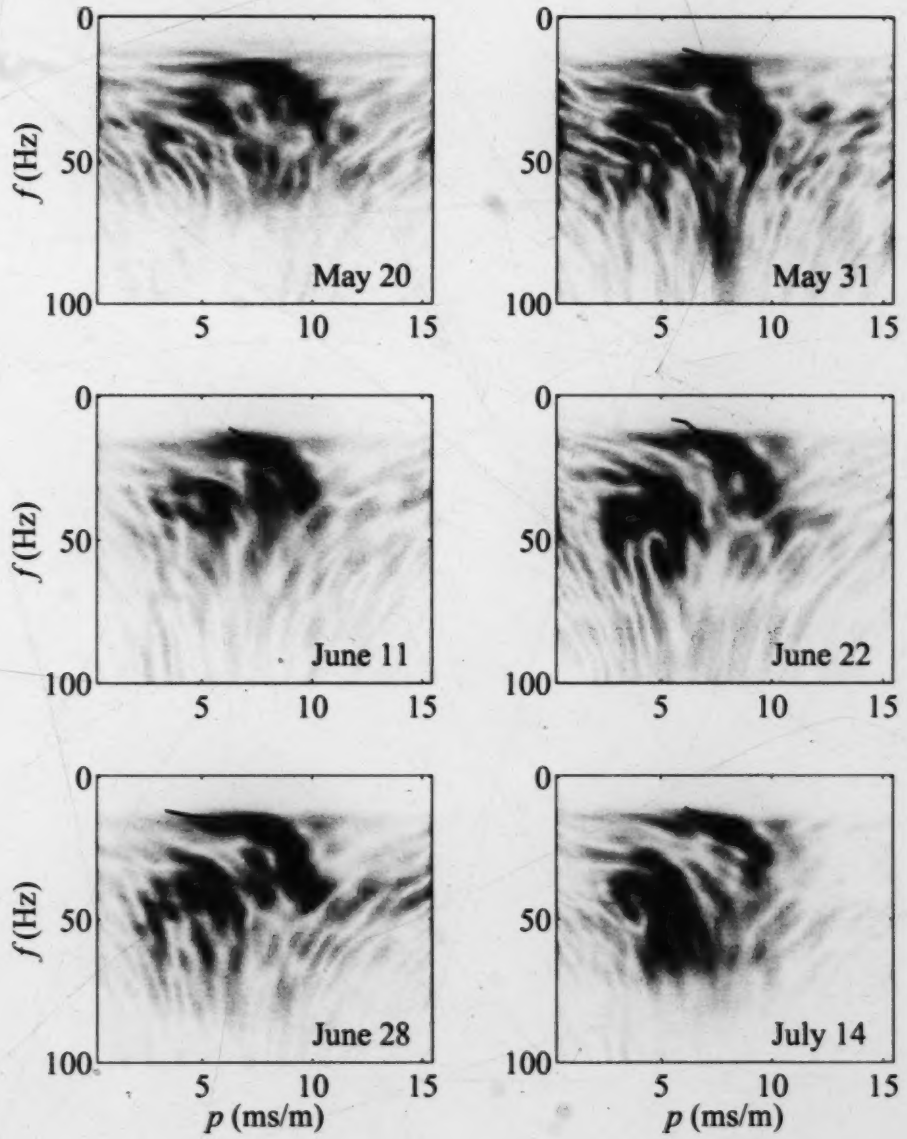

Figure 5.26: Frequency versus slowness sections for transverse horizontal component data (10 Hz geophones). The black line superimposed on the image represent the fundamental mode dispersion curve.

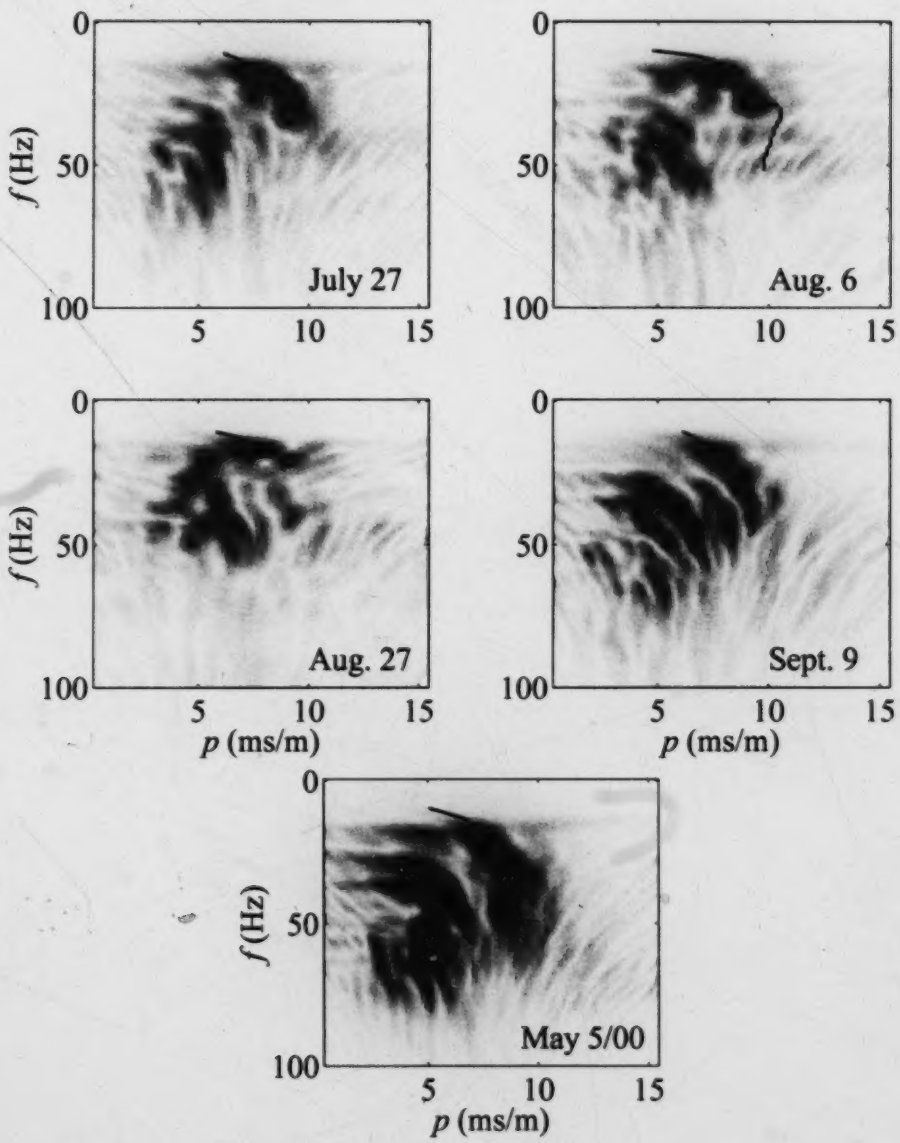

Figure 5.27: Frequency versus slowness sections for transverse horizontal component data (10 Hz geophones). The black line superimposed on the image represent the fundamental mode dispersion curve.

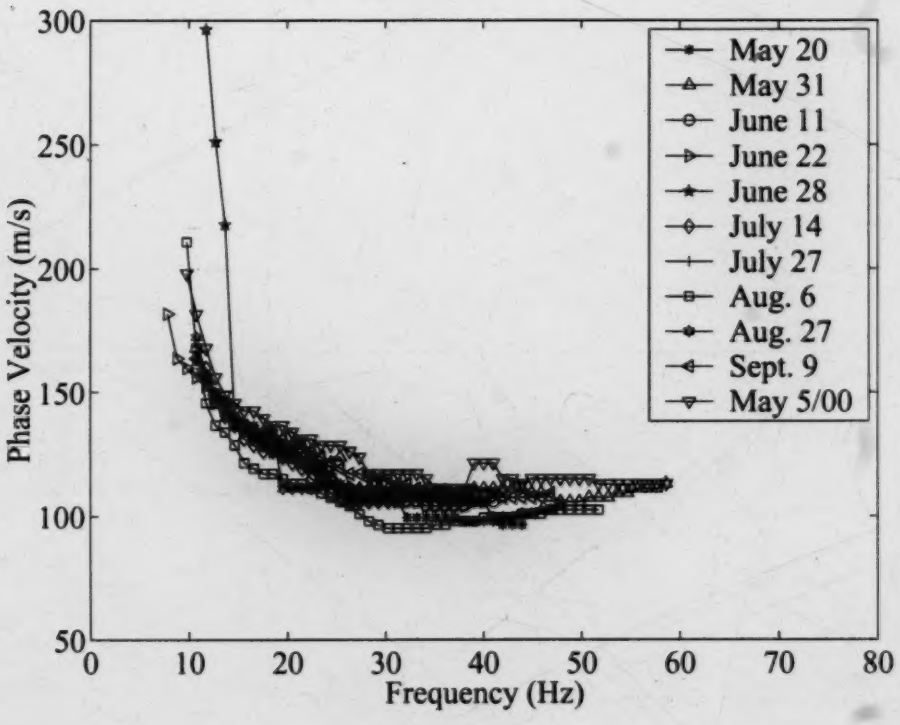

Figure 5.28: Phase velocity dispersion curves recorded at the Edmonton Research Station (horizontal-transverse component of 3-component 10 Hz geophones). Only the fundamental mode is shown.

5.5 Seasonal changes in dispersion curves

The main goal of this experiment was to examine seasonal changes in the seismic response of near-surface materials over the course of the summer and early fall. Dispersion curves obtained from surveys carried out on ten different dates between May 20 and September 9, 1999 indicate that there is no detectable change in Rayleigh wave phase velocity over the course of the survey period. Indeed, the uniformity of the differing observed curves is somewhat surprising.

There are, however, other differences in the data that become apparent when the surveys are compared. There are changes in the sharpness of the $f - p$ images that are noticeable when the sections from different dates are compared. These differences may be due to changes in the attenuative properties of the near-surface, which this experiment was not set up to examine adequately. In order to do this, a more repeatable source would be required.

Changes in attenuation are also apparent when the ranges of frequencies for which dispersion information is available for each date are examined. Figure 5.29 is the result of performing an interpolation between study dates of the phase velocities obtained from the dispersion analysis of the vertical component of the 3-component 10 Hz geophones. Phase velocities at frequencies for which there was no dispersion information were set to zero for interpolation purposes.

This image highlights two interesting results. The first has already been seen in figure 5.19 where it is evident that the phase velocities are virtually identical for all survey dates. The second observation that can be made is that there is a general trend of loss of high frequencies phase velocity data over the course of the summer with an abrupt regain of high frequencies in the fall. This trend of decreasing high frequency resolution is apparent in the data obtained using the 14 Hz vertical geophones as well (figure 5.22). This loss of high frequency data suggests that there is a trend of increasing attenuation in the top layer (about

1 m) that is likely related to a loss of soil moisture. A loss in soil moisture will result in lower connectivity between grains, more scattering of energy, and the presence of more air in the soil which is highly attenuating. All of these will result in the loss of the high frequency signal which is more rapidly attenuated and does not penetrate as deep as the lower frequency waves (longer wavelengths).

Meteorological data recorded hourly at the Edmonton Research Station, which may be useful for comparing to the data, are shown in figure 5.30 (Jeff Thurston, Department of Renewable Resources, University of Alberta, private communication).

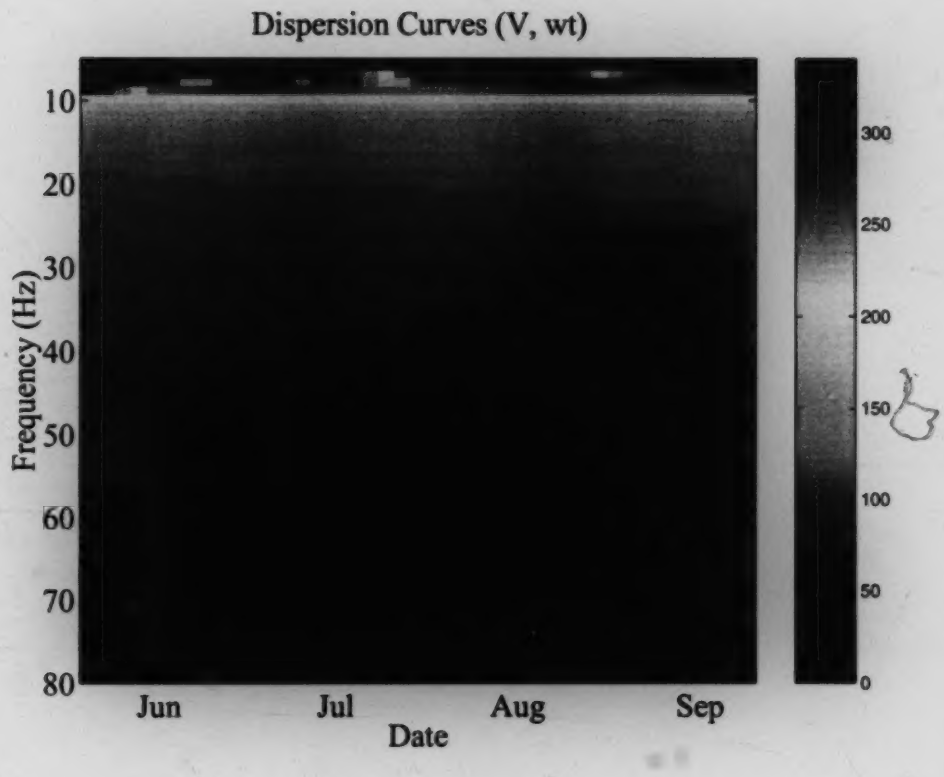

Figure 5.29: Interpolated image of the evolution of the fundamental mode Rayleigh wave dispersion curves with time. Phase velocity is represented by the colour of the image. The phase velocities at frequencies for which there was no dispersion information available have been set to zero for interpolation and display purposes. Note the progressive loss of higher frequency information with time during the summer.

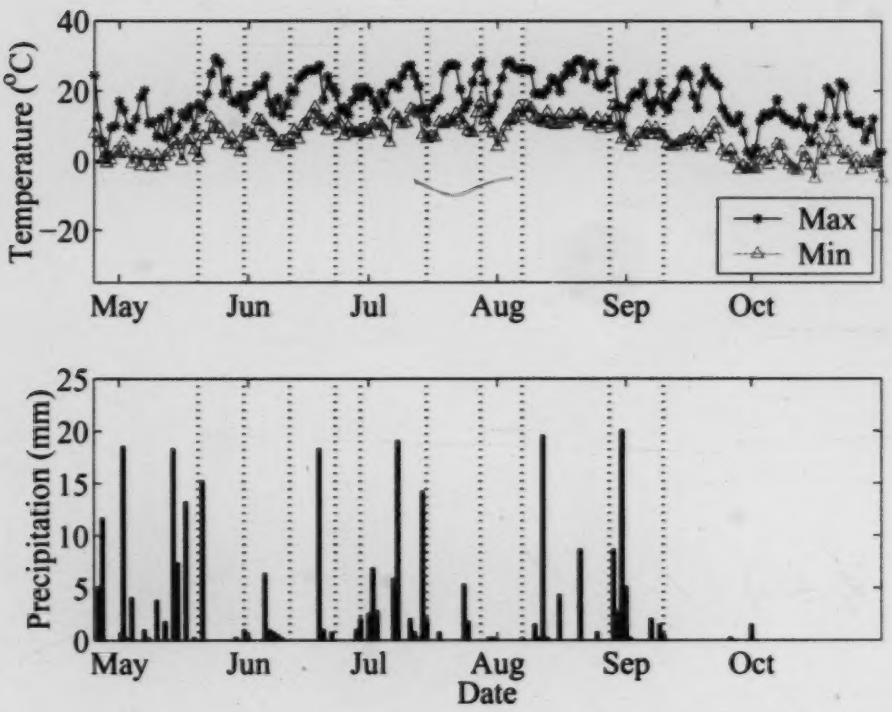

Figure 5.30: Top - Maximum and minimum daily temperatures; Bottom - Daily precipitation amounts recorded at the Edmonton Research Station. Vertical dotted lines indicate the dates that surface waves were recorded. Dates are labeled according to the first of each month (meteorological data provided by Jeff Thurston, Department of Renewable Resources, University of Alberta, private communication).

Chapter 6

Inversion and Interpretation

This chapter presents the forward modelling and inversion portion of the study. A matrix propagator method was chosen as a means for obtaining theoretical dispersion curves for Rayleigh waves in a layered medium of known elastic properties. This forward model was then incorporated into a simulated annealing algorithm in order to perform inversions on the observed dispersion curve data. Simulated annealing is a directed Monte Carlo inversion method that is well suited to finding the global minimum of a nonlinear error function. Finally, the results of the inversions and the uncertainty in these results, obtained using a Monte Carlo importance sampling technique, will be addressed.

6.1 Forward modelling and inverse theory

With surface wave studies, as with most other geophysical surveys, the main objective is to gain an understanding of the physical characteristics of the earth materials present at the study site. Rayleigh wave dispersion in an elastic medium is dependent on density, P- and S-wave velocities. The strongest dependence is on S-wave velocity (Fowler, 1990; Ewing et al., 1957). This section will first

describe the forward modelling technique used to obtain theoretical dispersion curves in an elastic, layered medium and then proceed to outline the inversion technique used to obtain velocity profiles from the measured dispersion curves.

6.1.1 Rayleigh waves in a homogeneous half-space

The solution for Rayleigh waves in a homogeneous half space shows that these waves are characterized by retrograde elliptical particle motion at the surface. The amplitude of the wave decays exponentially with depth. Horizontal particle motion ceases altogether at a certain depth after which particle motion becomes prograde elliptical (Ewing et al., 1957). The propagation of Rayleigh waves in a homogeneous isotropic half-space is one of only a very few situations for which dispersion curves can be found analytically.

The particle motion of a wave propagating through an isotropic, linearly elastic medium can be described by the equation

$$\rho\frac{\partial^2\mathbf{u}}{\partial t^2} = (\lambda+\mu)\nabla(\nabla\cdot\mathbf{u}) + \mu\nabla^2\mathbf{u}, \tag{6.1}$$

where $\mathbf{u}$ is the particle displacement vector, ρ is the density, and μ and λ are elastic constants known as the Lamé parameters. The parameter μ is also known as the shear modulus. Applying the following vector identity

$$\nabla^2\mathbf{u} = \nabla(\nabla\cdot\mathbf{u}) - \nabla\times(\nabla\times\mathbf{u}) \tag{6.2}$$

to equation (6.1) yields

$$\rho\frac{\partial^2\mathbf{u}}{\partial t^2} = (\lambda+2\mu)\nabla(\nabla\cdot\mathbf{u}) - \mu\nabla\times(\nabla\times\mathbf{u}). \tag{6.3}$$

Helmholtz's theorem (Lay and Wallace, 1995) states that any vector field $\mathbf{u}$ can be represented in terms of a vector potential $\boldsymbol{\psi}$ and a scalar potential ϕ through the relation

$$\mathbf{u} = \nabla\phi + \nabla\times\boldsymbol{\psi} \tag{6.4}$$

where the potentials must satisfy

$$\nabla \times \phi = 0 \tag{6.5}$$

and

$$\nabla \cdot \psi = 0. \tag{6.6}$$

Physically these conditions mean that ϕ involved no shearing motion and ψ involves no change in volume. Equation (6.3) can be expressed in terms of these potentials. Substituting (6.4) into (6.3) and applying the vector identity (6.2) yields

$$\nabla \left[\rho \frac{\partial^2 \phi}{\partial t^2} - (\lambda + 2\mu) \nabla^2 \phi \right] + \nabla \times \left[\rho \frac{\partial^2 \psi}{\partial t^2} - \mu \nabla^2 \psi \right] = 0. \tag{6.7}$$

This equation is satisfied if each of the terms in brackets goes to zero independently. In other words, the potentials ϕ and ψ must satisfy

$$\nabla^2 \phi = \frac{1}{\alpha^2} \frac{\partial^2 \phi}{\partial t^2} \tag{6.8}$$

and

$$\nabla^2 \psi = \frac{1}{\beta^2} \frac{\partial^2 \psi}{\partial t^2} \tag{6.9}$$

where the constants α and β represent the P- and S-wave velocities respectively. These velocities are related to the elastic constants through the relations

$$\alpha = \sqrt{\frac{\lambda + 2\mu}{\rho}} \tag{6.10}$$

and

$$\beta = \sqrt{\frac{\mu}{\rho}}. \tag{6.11}$$

Consider a plane wave traveling along the surface of an isotropic, homogeneous half-space in the x direction with the properties that the disturbance is independent of the y coordinate and decreases rapidly with depth z. The property of zero Rayleigh wave particle motion in the y direction allows the vector

potential $\boldsymbol{\psi}$ to be reduced to a scalar equal to the y component of the vector potential which will be written as ψ (recall that particle motion due to the vector potential is equal to $\nabla \times \boldsymbol{\psi}$). Solutions to (6.8) and (6.9) for the wave potentials ϕ and ψ that satisfy these conditions can be written as (Ewing et al., 1957)

$$\phi = Ae^{-kz\sqrt{1-\frac{c^2}{\alpha^2}}}e^{ik(ct-x)} \tag{6.12}$$

$$\psi = Be^{-kz\sqrt{1-\frac{c^2}{\beta^2}}}e^{ik(ct-x)} \tag{6.13}$$

where α and β are the P- and S-wave velocities respectively, c is the Rayleigh wave phase velocity, k is the wavenumber and A and B are constants that can be determined from the boundary conditions. This equation is valid over the region $0 \leq z < \infty$. The signs have been chosen so that the potentials approach zero as z approaches ∞ under the condition that $c < \beta < \alpha$.

The free surface boundary conditions require that the stresses vanish at the interface $z = 0$. This can be formally expressed as

$$[\tau_{zz}]_{z=0} = \left[\lambda\nabla^2\phi + 2\mu\frac{\partial^2\phi}{\partial z^2} + 2\mu\frac{\partial^2\psi}{\partial x \partial z}\right]_{z=0} = 0 \tag{6.14}$$

$$[\tau_{xz}]_{z=0} = \left[\mu\left(2\frac{\partial^2\phi}{\partial x \partial z} + \frac{\partial^2\psi}{\partial x^2} - \frac{\partial^2\psi}{\partial z^2}\right)\right]_{z=0} = 0 \tag{6.15}$$

where τ_{zz} and τ_{xz} are the normal and tangential stresses respectively. Evaluating the boundary conditions at $z = 0$ and expressing the results in terms of the velocities α and β yields the following two expressions

$$\left(2 - \frac{c^2}{\beta^2}\right)A - 2\sqrt{\frac{c^2}{\beta^2} - 1}B = 0 \tag{6.16}$$

$$2\sqrt{\frac{c^2}{\alpha^2} - 1}A + \left(2 - \frac{c^2}{\beta^2}\right)B = 0. \tag{6.17}$$

In order to obtain a non-trivial solution, the determinant of these equations must vanish. This results in the equation

$$\left(2 - \frac{c^2}{\beta^2}\right)^2 = 4\left(1 - \frac{c^2}{\alpha^2}\right)^{\frac{1}{2}}\left(1 - \frac{c^2}{\beta^2}\right)^{\frac{1}{2}}. \tag{6.18}$$

Rationalization of this expression combined with factoring out the quantity c/β yields

$$\frac{c^2}{\beta^2}\left[\frac{c^6}{\beta^6} - 8\frac{c^4}{\beta^4} + c^2\left(\frac{24}{\beta^2} - \frac{16}{\alpha^2}\right) - 16\left(1 - \frac{\beta^2}{\alpha^2}\right)\right] = 0. \tag{6.19}$$

The solution for $c = 0$ results in zero particle motion and is not of interest. The solution for the second factor is the one related to the propagation of a Rayleigh wave. As an example, this factor will be evaluated for a Poisson solid, which is defined as a material with a Poisson's ratio $\nu = \lambda/[2(\lambda + \mu)] = 0.25$. This corresponds to a solid with $\alpha = \sqrt{3}\beta$ which is equivalent to having $\lambda = \mu$. Using the relationship between α and β for a Poisson solid, the second factor in equation (6.19) reduces to

$$\frac{c^6}{\beta^6} - 8\frac{c^4}{\beta^4} + \frac{56}{3}\frac{c^2}{\beta^2} - \frac{32}{3} = 0. \tag{6.20}$$

Three real roots can be found that satisfy this equation: $c^2/\beta^2 = 4, 2+2/\sqrt{3}, 2-2/\sqrt{3}$. This last root provides the only solution that satisfies the condition that particle motion must decay as z approaches ∞. This root results in a Rayleigh wave phase velocity of

$$c_R = 0.9194\beta. \tag{6.21}$$

It is interesting to note that the phase velocity has no frequency dependence in this case. In a homogeneous half-space, Rayleigh waves are non-dispersive whereas in a layered medium they are always dispersive.

The particle motion of the Rayleigh wave in a Poisson solid can be obtained from the wave potentials. The particle motion u in the x direction and w in the z direction can be reduced to the following expressions

$$\begin{aligned} u &= D\left(e^{-0.8475kz} - 0.5773e^{-0.3933kz}\right)\sin k(0.9194\beta t - x) \\ w &= D\left(-0.8475e^{-0.8475kz} + 1.4679e^{-0.3933kz}\right)\cos k(0.9194\beta t - x) \end{aligned} \tag{6.22}$$

where D is a function of k. Figure 6.1 illustrates the particle motion of a Rayleigh wave in a Poisson solid.

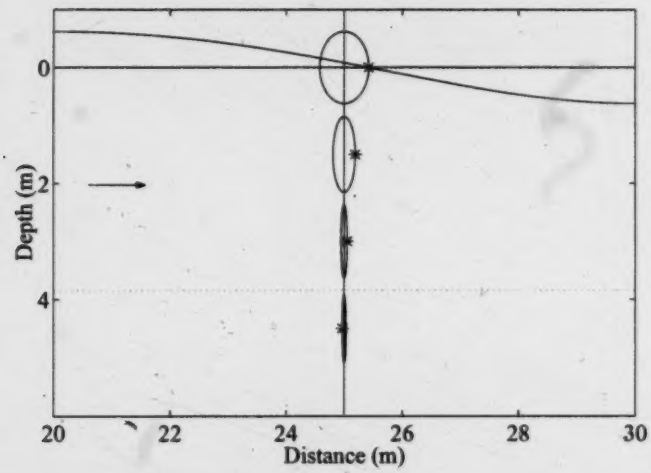

Figure 6.1: Particle motion of a Rayleigh wave with a wavelength of 20 m in an infinite half space for a Poisson solid ($\alpha = \sqrt{3}\beta$; $\lambda = \mu$; $\nu = 0.25$ where ν is Poisson's ratio). Wave propagation is to the right. Particle motion is elliptical with amplitude decreasing exponentially with depth. Asterisks mark displaced particle locations. In all cases the marked particles are moving in the upward direction, resulting in retrograde motion above the dotted line and prograde below.

6.1.2 Rayleigh waves in a layered medium

Only a very few simple cases such as the homogeneous half-space and a single layer overlying a half-space have analytic solutions that are easily obtained. In reality, however, geology is rarely that simple and numerical methods for determining Rayleigh wave dispersion curves for more complex geological models must be explored. Matrix methods are often used to determine the eigenvalues and eigenfunctions for the case of a vertically varying medium consisting of a set of n homogeneous layers overlying a homogeneous half space.

Thomson (1950) developed the original matrix method for solving this boundary value problem. He made the mistake, however, of assuming that the shear strain τ_{xz}/μ should be held constant across a given boundary rather than the shear stress τ or a constant multiple thereof. This mistake was corrected by Haskell (1953). The downfall of this technique is that numerical stability problems arise when the product of the depth to the homogeneous half space and the wavenumber is large (at high frequencies). Most of the ideas behind Haskell's derivation have been maintained in subsequent formulations of the problem. The main difference between Haskell's method and the methods of others lies in the algebraic manipulation of the matrices to find ways of expressing the problem that are computationally more stable.

Subsequent researchers reformulated the problem using global matrices in such a way that numerical stability was improved and solutions could be obtained for much higher frequencies than previously possible (Knopoff, 1964; Schwab and Knopoff, 1972). The global matrix formulation involves constructing a matrix of size $(n \times 4) \times (n \times 4)$ to represent all 4 of the equations in this boundary value problem for each of the n layers with a single matrix. Reduced-δ-matrix formulations have also been derived (Watson, 1970) but can be shown to be identical to Knopoff's method (Schwab, 1970). The key to the success of these later methods was the algebraic elimination of terms that involved the square of an exponential. These terms are the primary source of numerical instability. Schwab and Knopoff (1970) also suggested several other implementations that can help to reduce computational error. One suggestion was to approximate the higher frequency solutions by using a layer-reduction method where the lower part of the medium is replaced with a homogeneous half space at increasingly shallower depths. A normalization step was also suggested to avoid numerical overflow when exponential terms become large. Computer code, thought to be

the fastest at the time (Schwab, 1970), is included in Schwab and Knopoff (1972).

Abo-Zena (1979) claims to have further improved upon the method described in Schwab and Knopoff (1972) in terms of the ability of the method to handle high frequencies. This method has the advantage that the transfer matrices are formed independent of the layer thickness and frequency, which helps to improve the numerical stability. Menke (1979) noticed that the method of Abo-Zena (1979) could be simplified for programming purposes by reformulating the problem originally involving 4×4 matrices into one that only computes the five independent elements of these matrices resulting in improvements in both speed and accuracy. Menke's version was chosen for forward modelling for this study. The paper provides clear definitions of the matrix elements and the method of propagation so that it can be easily translated into a computer algorithm.

It should be mentioned that other techniques have been used to solve for Rayleigh wave dispersion curves in layered media. Numerical methods for solving ordinary differential equations such as the Runge Kutta method or the Rayleigh-Ritz variational procedure have been used (Takeuchi and Saito, 1972; Wiggins, 1976). These methods have all been developed with earthquake seismology applications in mind but they scale to any size problem.

All of the matrix methods mentioned above set out to determine Rayleigh wave dispersion curves in a set of homogeneous, isotropic elastic layers underlain by an infinite half-space (figure 6.2). For a layered media, Rayleigh waves arise from the interference of P and SV waves (vertically polarized shear waves) with the free surface. The propagation of SH waves is considered an independent problem that leads to Love waves, which will not be treated here. Thus the particle motion in the y direction for a Rayleigh wave traveling along the free surface in the x direction will be zero. Within a homogeneous medium, particle displacements in the horizontal and vertical directions, u and w, as well as the

normal stress, τ_{zz}, and the tangential stress, τ_{xz}, can all be derived from a scalar potential ϕ and a vector potential ψ (Ewing et al., 1957) that satisfy

$$\nabla^2\phi = \frac{1}{\alpha^2}\frac{\partial^2\phi}{\partial t^2} \tag{6.23}$$

and

$$\nabla^2\psi = \frac{1}{\beta^2}\frac{\partial^2\psi}{\partial t^2} \tag{6.24}$$

where α and β are the P- and S-wave velocities respectively and ϕ and ψ are subject to boundary conditions at the surface of each layer. Here ψ actually reduces to a scalar in order to satisfy the condition that particle motion for a Rayleigh wave in the y direction must be zero. Formulating the problem in terms of potentials rather than displacements is more convenient because displacements u and w are coupled whereas the potentials are not.

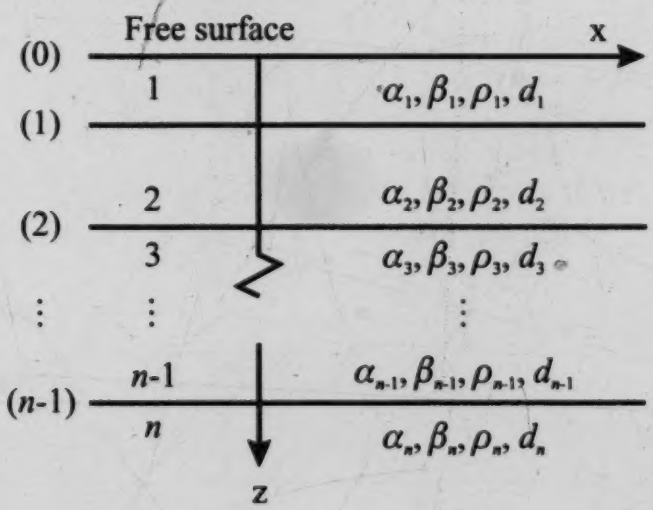

Figure 6.2: Diagram showing layered structure with n layers. Layers and interfaces are numbered. Each layer has P- and S-wave velocities (α and β) as well as density (ρ) and thickness (d).

Plane wave solutions for the potentials in (6.8) and (6.9) can be taken as

$$\phi = \phi_o(z)e^{i(\omega t - kx)} \tag{6.25}$$

$$\psi = \psi_o(z)e^{i(\omega t - kx)}. \tag{6.26}$$

Substituting (6.25) and (6.26) into (6.8) and (6.9) respectively yields

$$\frac{d^2\phi_o}{dz^2} = k^2(1 - c^2/\alpha^2)\phi_o \tag{6.27}$$

$$\frac{d^2\psi_o}{dz^2} = k^2(1 - c^2/\beta^2)\psi_o. \tag{6.28}$$

The solutions to equations (6.27) and (6.28), in the notation of Abo-Zena (1979), can be expressed as

$$\phi_o = b_1 \cosh(r_\alpha kz) + b_2 \sinh(r_\alpha kz) \tag{6.29}$$

$$\psi_o = b_3 \cosh(r_\beta kz) + b_4 \sinh(r_\beta kz) \tag{6.30}$$

or in exponential form as

$$\phi_o = B_1 \exp(r_\alpha kz) + B_2 \exp(-r_\alpha kz) \tag{6.31}$$

$$\psi_o = B_3 \exp(r_\beta kz) + B_4 \exp(-r_\beta kz) \tag{6.32}$$

where $r_\alpha = (1 - (c/\alpha)^2)^{1/2}$ and $r_\beta = (1 - (c/\beta)^2)^{1/2}$ can be imaginary if $c > \alpha$ or $c > \beta$ respectively. The constants b_i (or B_i for the exponential case) depend on boundary conditions imposed at the boundaries of each layer. For this derivation the trigonometric forms will be used.

In this problem, it is assumed that the interface between each layer is a welded contact. The boundary conditions consequently require that the displacements and stresses be continuous across each interface, except at the free surface where the stresses cannot exist and are set to zero. The boundary conditions at an

interface m between layers m and $m+1$ can be expressed as

$$\begin{aligned} u_m(d_m) &= u_{m+1}(0) \\ w_m(d_m) &= w_{m+1}(0) \\ \tau_{zz,m}(d_m) &= \tau_{zz,m+1}(0) \\ \tau_{xz,m}(d_m) &= \tau_{xz,m+1}(0) \end{aligned} \tag{6.33}$$

where d_m is the thickness of layer m. Haskell (1953) used continuity of velocities in the x and z directions in place of continuity of particle displacements as boundary conditions which ultimately achieves the same dispersion solution. The displacements u and w and the normal stress τ_{zz} and tangential stress τ_{xz} can be related to the potentials ϕ and ψ as follows:

$$u = \frac{\partial \phi}{\partial x} - \frac{\partial \psi}{\partial z} \tag{6.34}$$

$$w = \frac{\partial \phi}{\partial z} + \frac{\partial \psi}{\partial x} \tag{6.35}$$

$$\tau_{zz} = \lambda \nabla^2 \phi + 2\mu \frac{\partial^2 \phi}{\partial z^2} + 2\mu \frac{\partial^2 \psi}{\partial x \partial z} \tag{6.36}$$

$$\tau_{xz} = \mu \left(2\frac{\partial^2 \phi}{\partial x \partial z} + \frac{\partial^2 \psi}{\partial x^2} - \frac{\partial^2 \psi}{\partial z^2} \right) \tag{6.37}$$

where λ and μ are the Lame parameters. The relationships for the particle displacements (6.34) and (6.35) come from the definition of the scalar and vector potentials coupled with the condition that particle motion in the y direction is equal to zero for Rayleigh waves in an isotropic medium. The equations for the stresses (6.36) and (6.37) subsequently follow from Hooke's law (Shearer, 1999).

The stresses and displacements can be related to the constants b_i by substituting solutions (6.29) and (6.30) into equations (6.34) to (6.37), yielding

$$\begin{aligned} u &= -ikb_1 \cosh(r_\alpha kz) - ikb_2 \sinh(r_\alpha kz) \\ &\quad -r_\beta kb_3 \sinh(r_\beta kz) - r_\beta kb_4 \cosh(r_\beta kz) \end{aligned} \tag{6.38}$$

$$\begin{aligned} w &= r_\alpha k b_1 \sinh(r_\alpha kz) + r_\alpha k b_2 \cosh(r_\alpha kz) \\ &\quad -ikb_3 \cosh(r_\beta kz) - ikb_4 \sinh(r_\beta kz) \end{aligned} \tag{6.39}$$

$$\begin{aligned} \tau_{zz} &= \rho(\gamma-1)k^2c^2 b_1 \cosh(r_\alpha kz) + \rho(\gamma-1)k^2c^2 b_2 \sinh(r_\alpha kz) \\ &\quad -ik^2 r_\beta 2\rho\beta^2 b_3 \sinh(r_\beta kz) - ik^2 r_\beta 2\rho\beta^2 b_4 \cosh(r_\beta kz) \end{aligned} \tag{6.40}$$

$$\begin{aligned} \tau_{xz} &= -ik^2 r_\alpha 2\rho\beta^2 b_1 \sinh(r_\alpha kz) - ik^2 r_\alpha 2\rho\beta^2 b_2 \cosh(r_\alpha kz) \\ &\quad -\rho(\gamma-1)k^2c^2 b_3 \cosh(r_\beta kz) - \rho(\gamma-1)k^2c^2 b_4 \sinh(r_\beta kz) \end{aligned} \tag{6.41}$$

where $\gamma = 2(\beta/c)^2$ and the factor of $\exp(i(\omega t - kx))$ has been suppressed. This is a set of four equations and four unknowns that can be expressed in matrix form:

$$\mathbf{W} = \underset{\sim}{\mathbf{U}}_m(z)\mathbf{B}, \tag{6.42}$$

where

$$\mathbf{W}^T = [iu/k, w/k, \tau_{zz}/k^2c^2, i\tau_{xz}/k^2c^2] \tag{6.43}$$

is know as the motion-stress vector,

$$\mathbf{B}^T = [b_1, b_2, -ib_3, -ib_4] \tag{6.44}$$

is a vector of as yet undetermined constants, and $\underset{\sim}{\mathbf{U}}_m(z)$ is a 4×4 matrix relating $\mathbf{W}$ to $\mathbf{B}$ which can be defined as (Abo-Zena, 1979)

$$\underset{\sim}{\mathbf{U}}_m(z) = \begin{bmatrix} 1 & 1 & r_\beta & r_\beta \\ r_\alpha & r_\alpha & 1 & 1 \\ \rho(\gamma-1) & \rho(\gamma-1) & \rho\gamma r_\beta & \rho\gamma r_\beta \\ \rho\gamma r_\alpha & \rho\gamma r_\alpha & \rho(\gamma-1) & \rho(\gamma-1) \end{bmatrix}$$

$$\begin{bmatrix} \exp(r_\alpha kz) & 0 & 0 & 0 \\ 0 & \exp(r_\alpha kz) & 0 & 0 \\ 0 & 0 & \exp(r_\beta kz) & 0 \\ 0 & 0 & 0 & \exp(r_\beta kz) \end{bmatrix}$$

$$+ \begin{bmatrix} 1 & -1 & -r_\beta & r_\beta \\ -r_\alpha & r_\alpha & 1 & -1 \\ \rho(\gamma-1) & -\rho(\gamma-1) & -\rho\gamma r_\beta & \rho\gamma r_\beta \\ -\rho\gamma r_\alpha & \rho\gamma r_\alpha & \rho(\gamma-1) & -\rho(\gamma-1) \end{bmatrix}$$

$$\begin{bmatrix} \exp(-r_\alpha kz) & 0 & 0 & 0 \\ 0 & \exp(-r_\alpha kz) & 0 & 0 \\ 0 & 0 & \exp(-r_\beta kz) & 0 \\ 0 & 0 & 0 & \exp(-r_\beta kz) \end{bmatrix} \tag{6.45}$$

The displacements and stresses at the boundary (m) between layers m and $m+1$ can then be propagated to those at the boundary $(m-1)$ through the relation

$$\mathbf{W}_{(m)} = \underline{\mathbf{A}}_m \mathbf{W}_{(m-1)} \tag{6.46}$$

where

$$\underline{\mathbf{A}}_m = \underline{\mathbf{U}}_m(d_m)\underline{\mathbf{U}}_m(0)^{-1} \tag{6.47}$$

and d_m is the thickness of layer m and $\underline{\mathbf{U}}_m(0)^{-1}$ is the inverse of the matrix $\underline{\mathbf{U}}_m(z)$ evaluated at $z = 0$.

The expression (6.46) can be applied repeatedly, yielding

$$\mathbf{W}_{(n-1)} = \underline{\mathbf{A}}_{n-1} \cdots \underline{\mathbf{A}}_2 \underline{\mathbf{A}}_1 \mathbf{W}_{(0)} \tag{6.48}$$

$$= \underline{\mathbf{T}} \mathbf{W}_{(0)}. \tag{6.49}$$

The reduced matrix $\underline{\mathbf{T}}$ is known as a propagator matrix. Now if the inverse of equation (6.42) is applied with $z = 0$, this becomes

$$\begin{aligned} \mathbf{B}_n &= \underline{\mathbf{U}}_n(0)^{-1}\mathbf{W}_{(n-1)} \\ \mathbf{B}_n &= \underline{\mathbf{U}}_n(0)^{-1}\underline{\mathbf{T}}\mathbf{W}_{(0)} \\ &= \underline{\mathbf{J}}\mathbf{W}_{(0)}. \end{aligned} \tag{6.50}$$

This can alternately be expressed as

$$\begin{bmatrix} b_1 \\ -b_1 \\ -ib_3 \\ ib_3 \end{bmatrix}_n = \begin{bmatrix} J_{11} & J_{12} \\ J_{21} & J_{22} \\ J_{31} & J_{32} \\ J_{41} & J_{42} \end{bmatrix} \cdot \begin{bmatrix} iu/k \\ w/k \end{bmatrix}_{(0)} \tag{6.51}$$

where the stresses at the free surface have been set to zero and the relations $b_1 = -b_2$ and $b_3 = -b_4$ for layer n have been applied to ensure that particle motion approaches zero at infinity.

Equation (6.51) can be simplified by combining the expressions for b_1 and b_3 that can be obtained from this matrix yielding

$$\begin{bmatrix} 0 \\ 0 \end{bmatrix} = \begin{bmatrix} J_{11} + J_{21} & J_{12} + J_{22} \\ J_{31} + J_{41} & J_{32} + J_{42} \end{bmatrix} \cdot \begin{bmatrix} iu/k \\ w/k \end{bmatrix}_{(0)} . \tag{6.52}$$

In general the particle motion in the x and z directions is non-zero so it follows that there are only valid solutions to (6.52) when the determinant of the 2×2 matrix vanishes. A dispersion function can be defined as

$$D(\omega, c) = (J_{11} + J_{21})(J_{32} + J_{42}) - (J_{31} + J_{41})(J_{12} + J_{22}) = 0. \tag{6.53}$$

The roots of this dispersion function are the dispersion curves corresponding to the layered model of figure 6.2.

Up to this point the problem has been formulated in terms of downward propagation of the motion-stress vector. Abo-Zena (1979) goes on to show that a matrix $\underline{\mathbf{Y}}$ can be defined in such a way that it can be propagated upwards using the relation

$$\underline{\mathbf{Y}}_m = \underline{\mathbf{A}}_m^T \underline{\mathbf{Y}}_{m+1} \underline{\mathbf{A}}_m \tag{6.54}$$

with the result that $D(\omega, c) = \underline{\mathbf{Y}}_0(1,2)$ is the value of the dispersion function for a given angular frequency and phase velocity. The main advantage of the

formulation used by Abo-Zena (1979) is that a factored form of $\underset{\sim}{\mathbf{A}}_m$ is used which allows terms involving the square of an exponential to cancel analytically. The elimination of these terms coupled with the fact that matrix multiplications are carried out separately from multiplication by exponential factors improves the numerical stability and allows dispersion function to be calculated at high frequencies.

Menke (1979) shows how the problem can be approached from the beginning using upward propagator matrices which leads to a physical interpretation of the elements of the resultant matrix. One offshoot of this physical interpretation is that it makes it possible to extend the method to construct synthetic seismograms containing both surface and body waves when the properties of a source wavelet are incorporated. Menke (1979) offers a simplification of the matrix formulation of Abo-Zena (1979) based on the observation that only five of the matrix elements of $\underset{\sim}{\mathbf{Y}}_m$ are independent (Takeuchi and Saito, 1972). It follows that a new type of propagator $\underset{\sim}{\mathbf{F}}_m$, now a 5×5 matrix, can be defined such that

$$\mathbf{E}_{m-1} = \underset{\sim}{\mathbf{F}}_m \mathbf{E}_m \tag{6.55}$$

where $\mathbf{E}_m$ are column vectors containing the five independent elements of $\underset{\sim}{\mathbf{Y}}_m$. The same procedure as used by Abo-Zena (1979) can be employed to separate the exponential factors out from the matrix multiplications. This method was adopted for this study. For details on the implementation of this method, please refer to Menke (1979).

As and example, figure 6.3 shows the dispersion function found using this method for a simple three layer geology:

Layer	α (km/s)	β (km/s)	ρ (g/cm^3)	d (km)
1	6.14	3.39	2.70	13.60
2	5.50	3.18	2.70	11.85
3	8.26	4.65	3.00	∞

where α is the P-wave velocity, β is the S-wave velocity, ρ is the density, and d is the thickness of the each layer. This model is representative of an Earth model with a low velocity layer. The dispersion curves for each mode were determined by finding the roots of the dispersion function $D(\omega, c)$ using the bisection method which is a standard root finding algorithm (Press et al., 1997). The black circles and line in figure 6.3 show the theoretical dispersion curve found by Haskell (1953) for the same set of parameters. This solution lies directly over the first root of the dispersion function found using the method of Menke (1979), showing excellent agreement between the two theoretical formulations at low frequencies.

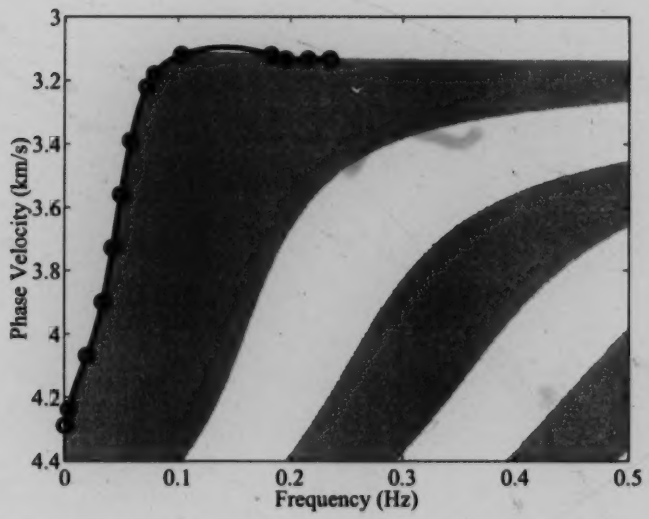

Figure 6.3: Dispersion function calculated using the matrix method of Menke (1979). White and gray bands represent positive and negative values of the dispersion function, respectively. The black circles, connected by a cubic spline, represent the dispersion curve for the fundamental Rayleigh mode found using the method of Haskell (1953) for the same set of model parameters.

6.1.3 The inversion of Rayleigh wave dispersion curves

A simulated annealing algorithm will be used to perform the inversion of the Rayleigh wave dispersion curves in order to determine the velocity structure of the earth. Simulated annealing, like other geophysical inversion procedures, seeks to minimize an error function $E(\mathbf{m})$ where $\mathbf{m}$ is the model vector. The advantage of this technique is that it is not limited to linear problems and will seek to find the global rather than a local minimum in the error function. The definitions of the error function and the forward model are independent of the inversion algorithm so there is freedom to define both of these functions in whatever way best suits the problem. It is a directed Monte Carlo method that has its roots in statistical mechanics that has been used to solve many optimization problems (Kirkpatrick et al., 1983; Chunduru et al., 1996). The disadvantage of this technique is that it can be computationally more expensive than linearized methods.

Simulated annealing does not appear to have been used to before for the inversion of surface wave dispersion curves. Most researchers have employed linearized methods (Ganji et al., 1998; Aki and Richards, 1980) or else a combination of linear and nonlinear methods (Xia et al., 1999b). Roth and Holliger (1999), however, used a genetic algorithm, which is another example of a directed Monte Carlo inversion technique. They were able to obtain both P- and S-wave velocity profiles by inverting dispersion curves from both Rayleigh and guided waves and comparing to theoretical curves found using a matrix method. Density was held constant as the phase velocities of both of these wave types are relatively insensitive to this parameter. Simulated annealing will be applied to Rayleigh wave dispersion curves in this study in a similar fashion.

To understand the concept of simulated annealing an analogy can be drawn between the model parameters of an optimization problem and particles in a

physical system. Physical annealing occurs when a solid is heated up until all the particles are randomly distributed in the liquid phase. When the material is cooled, if it is cooled in a slow, controlled manner then the particles will settle into their low energy ground state and the result will be a crystalline solid. If the material is cooled too quickly then the material will freeze into a local minimum and an amorphous glass will be formed. The probability at each temperature T that the system will be in state i with energy E_i is

$$P(E_i) = \frac{\exp\left(-\frac{E_i}{k_B T}\right)}{\sum_{j \in S} \exp\left(-\frac{E_j}{k_B T}\right)} \tag{6.56}$$

where S contains all possible particle configurations and k_B is Boltzmann's constant. For geophysical inversions, k_B is set to 1 and instead of energy the probability distribution function becomes a function of possible sets of model parameters $\mathbf{m}_i$. The 'temperature' T takes on the dimensions of the error and can be looked upon as a control parameter. Sen and Stoffa (1995) provide a good basic overview of simulated annealing as applied to complex geophysical data sets. A more detailed review with a complete list of references can be found in Ingber (1989).

One well known simulated annealing algorithm is the Metropolis algorithm (Metropolis et al., 1953). An outline of the basic algorithm is provided in Sen and Stoffa (1995). A flow diagram of the algorithm is shown in figure 6.4. By semi-randomly accepting some models that actually increase the error, the algorithm attempts to avoid becoming trapped in local minima. At low temperatures this reduces to a greedy algorithm, meaning that it only accepts models that decrease the error function. Convergence is achieved when the error or energy remains the same for several iterations.

The Metropolis algorithm can be modeled using finite Markov chains (Sen and Stoffa, 1995). A Markov chain is a sequence of trials in which the probability

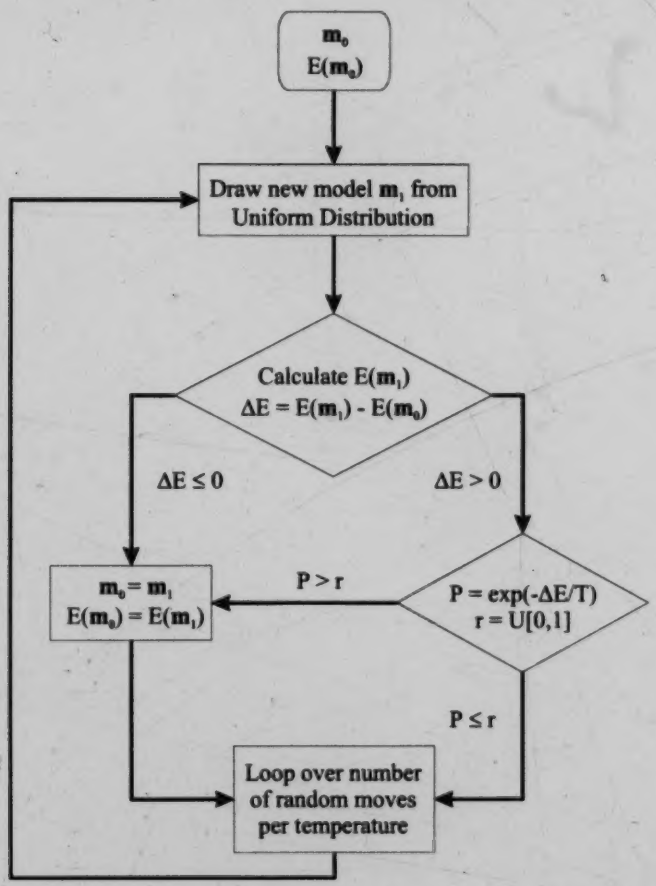

Figure 6.4: Flow chart of the operations carried out at each temperature for the Metropolis simulated annealing algorithm.

of the outcome of a trial depends only on the outcome of the previous trial, not on any other. It can be shown, based on the acceptance and generation probabilities for Metropolis simulated annealing, that the Markov chain is irreducible and aperiodic. It then follows that there exists a unique stationary distribution such that the probability of the occurrence of a model is independent of the starting model. This distribution is the Gibbs' probability density function. In

the limit when the temperature goes to zero there is a probability of 1 that the global minimum will be reached as long as the temperature is reduced at a slow enough rate. The necessary and sufficient condition for convergence to the global minimum is given by the cooling schedule

$$T(i) = \frac{T_0}{\ln i} \tag{6.57}$$

where i is the iteration number and T_0 is a sufficiently high initial temperature (Geman and Geman, 1984).

Fast simulated annealing (FSA), a variant of the Metropolis algorithm, was proposed by Szu and Hartley (1987). This algorithm is identical to the Metropolis algorithm with the exception that model parameters are drawn from a Cauchy-like distribution instead of a uniform distribution. A Cauchy-like distribution is given by

$$P(\Delta \mathbf{m}) \propto \frac{T}{\sqrt{\Delta \mathbf{m}^2 + T^2}}. \tag{6.58}$$

At high temperature the distribution approaches uniformity while at lower temperatures it favours smaller perturbations (figure 6.5). For FSA the cooling schedule should not exceed

$$T(i) = \frac{T_0}{i} \tag{6.59}$$

which is much faster than for conventional simulated annealing.

The forward model being used in this study (Menke, 1979) represents the earth in terms of a discrete set of layers overlying a homogeneous half space. Each layer has its own density, P-wave velocity, and S-wave velocity. Density and P-wave velocity both have very little impact on the dispersion curves so they can be taken as a fixed parameters. This still leaves n parameters that need to be inverted for, where n is the number of layers. To save on computational time, if a smooth velocity profile is expected, then $\alpha(z)$ and $\beta(z)$ can be alternatively represented using a sum of Chebyshev polynomials (see Appendix

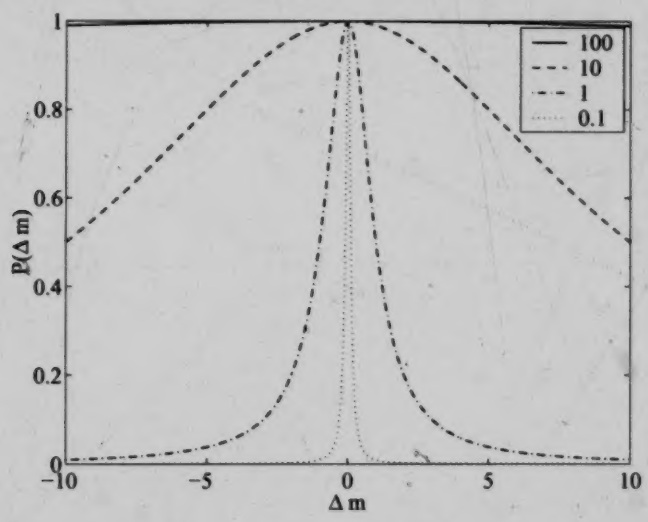

Figure 6.5: Diagram showing the shape of a Cauchy-like probability distribution for temperatures of 0.1, 1, 10, and 100.

A for an overview of Chebyshev polynomials). The inverse problem can then be structured to solve for the coefficients of this series instead of the velocities for each layer. Now instead of inverting for a large number of velocity parameters to approximate a continuous medium, $\alpha(z)$ can be represented by only four or five coefficients. The forward model can still be expressed in terms of discrete layers; after each step in the inversion, the velocity of layer z can be taken as the value of the polynomial series at the layer's center. Grechka et al. (1996) discuss the use of Chebyshev polynomials for other 1-D geophysical inverse problems and Chunduru et al. (1996) use spline parameterization instead of Chebyshev polynomials to represent their model in a simulated annealing inversion.

A reasonable initial model can be determined using bulk density data gathered from soil coring and velocities determined from the vertical seismic profile or else from average values tabulated for the geomaterials found to be present via

coring (Kearney and Brooks, 1995). According to the results of Xia et al. (1999b), a 25% error in both the P-wave velocity profile and the density profile will result in an error of only 7% in the S-wave profile. Good estimates of values for P-wave and density profiles should be sufficient to obtain a reasonable S-wave profile.

The inverse procedure will set out to find the global minimum of the objective function

$$E = \sum_f (d_{obs} - d_{pred})^2 \tag{6.60}$$

for each mode where d_{obs} is the dispersion curve determined from the observed data, d_{pred} is the dispersion curve predicted by the forward model, and the sum is over all frequencies. The fundamental mode can be inverted for separately or else the objective function can be represented by a weighted sum of residuals from all modes present in the data.

For this survey the misfit function was defined as the weighted sum of the error functions (6.60) for each mode. The weighted sum was achieved by first dividing the error function for each mode by the number of data points in that mode. Then the fundamental mode was assigned a weight of 0.5 and the two higher modes were assigned weights of 0.25 each. In these data there is some ambiguity as to whether the second and third modes obtained from the $f-p$ sections are really the second and third Rayleigh modes. It is possible that they may represent the third and fourth modes. To account for this ambiguity the misfit functions were calculated under both of these assumptions and the minimum misfit was used in the inversion at each iteration.

For this survey the misfit function was defined as the weighted sum of the error functions (6.60) for each mode. The weighted sum was achieved by first dividing the error function for each mode by the number of data points in that mode. Then the fundamental mode was arbitrarily assigned a weight of 0.5 and the two higher modes were assigned weights of 0.25 each. The rationale behind

this choice was that the fundamental mode tended to contain more energy and was easier to pick out than the two higher modes. With these data there is some ambiguity as to whether the second and third modes obtained from the $f-p$ sections are really the second and third Rayleigh modes. In some of the $f-p$ images there is a faint curve in between the fundamental and what has been deemed the second mode so it is possible that the curves that have been labeled as the second and third modes might actually represent the third and fourth modes. This faint curve that is present in only some of the images could also be related to noise in the data. To account for this ambiguity the misfit functions were calculated under both of these assumptions and the minimum misfit was used in the inversion at each iteration.

6.1.4 Uncertainty estimation

As previously mentioned, Metropolis simulated annealing can be modeled as a finite Markov chain which can be shown to be irreducible and aperiodic (Sen and Stoffa, 1995). As a result, after a large number of iterations at a constant temperature an equilibrium distribution will be attained independent of the starting model. This equilibrium distribution is given by the Gibbs' probability density function

$$p(\mathbf{m}) = \frac{\exp\left(-\frac{E(\mathbf{m})}{T}\right)}{\sum \exp\left(-\frac{E(\mathbf{m})}{T}\right)} \tag{6.61}$$

where $E(\mathbf{m})$ is the value of the error function for the model $\mathbf{m}$ and the temperature T controls the width of the distribution.

Bayes' rules, a powerful tool in statistics, states that the conditional probability $\sigma(\mathbf{m}|\mathbf{d})$ of a model $\mathbf{m}$ given the data $\mathbf{d}$ can be expressed as

$$\sigma(\mathbf{m}|\mathbf{d}) = \frac{p(\mathbf{d}|\mathbf{m})p(\mathbf{m})}{p(\mathbf{d})}. \tag{6.62}$$

The probability density function $p(\mathbf{m})$ is the probability of the model $\mathbf{m}$ independent of the data. This is related to the information available on the model before any data is obtained. The denominator in this equation is the probability density function of the data $p(\mathbf{d})$ and in geophysical inversion applications is taken as a constant as it is independent of the model. The conditional probability $p(\mathbf{d}|\mathbf{m})$ is called the likelihood function when the observed data are substituted into the function. If the error in theory and data are assumed to be Gaussian then the posterior probability density of model $\mathbf{m}$ given the observed data $\mathbf{d}_{obs}$ can be reduced to the following equation

$$\sigma(\mathbf{m}|\mathbf{d}_{obs}) \propto \exp(-E(\mathbf{m}))p(\mathbf{m}) \tag{6.63}$$

Comparison of this expression with equation (6.61) shows that it is essentially the Gibbs' probability density function at temperature $T = 1$ if the prior distribution is uniform.

Locating the global minimum of an error function corresponds to searching out the maximum of the posterior probability density function (PPD). An algorithm that searched for the maximum in the PPD is known as a maximum a posterior or MAP estimation algorithm and this is actually what Metropolis simulated annealing was originally designed to do.

Determination of the mean and covariance requires the evaluation of multidimensional integrals. For complicated functions it is sometimes necessary to resort to Monte Carlo methods of integration where the integral

$$I = \int_{x_{min}}^{x_{max}} f(x)\,dx \tag{6.64}$$

is replaced by the following sum

$$I = \frac{1}{n}\sum_{i=1}^{n} f(X_i) \tag{6.65}$$

where X_i is a random sample drawn from a uniform distribution over the interval (x_{min}, x_{max}) and n is a very large number. A Monte Carlo importance sampling

technique can be used if there is some information available on the relative contributions of different regions of the interval. Importance sampling attempts to concentrate the values of the random samples over the regions that have larger contributions to the integral so that the integral can be approximated using fewer random samples.

Metropolis simulated annealing, when it is run for a large number of iterations, is also referred to as a Gibbs' sampler. If it is run at a temperature T of 1 it may be used as a Monte Carlo importance sampling technique to evaluate quantities such as the marginal posterior probability density function, mean and covariance. The marginal posterior probability density function can be found directly from the frequency distribution of the model parameters. The mean can be approximated by the following equation

$$< \mathbf{m} > \cong \frac{1}{NM} \sum_{j=1}^{NM} \mathbf{m}_j \tag{6.66}$$

where $\mathbf{m}_1, \mathbf{m}_2, \ldots, \mathbf{m}_{NM}$ are column vectors of model parameters chosen by the Gibbs' sampler and NM is the total number of models used. The covariance will be given by

$$\underline{\mathbf{C}}_M \cong \frac{1}{NM} \sum_{j=1}^{NM} (\mathbf{m}_j - < \mathbf{m} >)(\mathbf{m}_j - < \mathbf{m} >)^T. \tag{6.67}$$

The standard deviations in the individual model parameters are given by the square root of the diagonal of the posterior covariance matrix. The mean and standard deviation values for the model parameters will give an estimate of the uncertainty in the inverted profile.

6.1.5 Testing the algorithms

A simple function was used to test out the fast simulated annealing routine. The function used in these initial tests is the same as used in Sen and Stoffa (1995):

$$f(x,y) = \mathrm{sgn}\left(\frac{\sin x}{x}\right)\left|\frac{\sin x}{x}\right|^{1/4} \mathrm{sgn}\left(\frac{\sin y}{y}\right)\left|\frac{\sin y}{y}\right|^{1/4}. \qquad (6.68)$$

The function sgn(x) returns a value of 1 for $x \geq 0$ and -1 for $x < 0$. Figure 6.6 shows a colour density plot of this function over a range of -10 to 10 in both x and y. The function has a global maximum at (0,0) and several local maxima; hence it ideally tests the capability of the inversion routine to find the global extremum value. Finding the global maximum of this function can be achieved by minimizing the following error function

$$E(x,y) = (1 - f(x,y))^2. \qquad (6.69)$$

This error function has a global minimum at (0,0) which can be found using simulated annealing.

A series of inversions on this function were performed using 16 different random seeds starting from the location (-8,6). An initial temperature T_0 of 20 was chosen by running a series of tests at different temperatures. For a good choice of initial temperature, the ratio of accepted models to rejected models after a large number of iterations at a constant temperature should be greater than 50% but less than 100%. If the ratio is less than 50% then the temperature may not be high enough to escape local minima and if the initial temperature is too high then it will take a much larger number of iterations than necessary for the algorithm to converge. The cooling schedule used was that described in equation (6.59) and two iterations of the inner loop were performed at each temperature. The misfit curves for these inversions are shown in figure 6.7. The mean and standard deviation of the results of these inversions give values of

$x = 0.0 \pm 0.6$ and $y = 0.0 \pm 0.5$ for the location of the global minimum in the error function. Similar results were obtained when the random seed was held constant and a number of runs were performed using random initial values for x and y.

Uncertainty analysis using Metropolis SA as an importance sampling algorithm gives a larger margin of error of ± 2 to each of these values. Histograms for y are shown in figure 6.8. The histograms for x look almost identical so they have not been included. Even though a large number of iterations is necessary to ensure a stable histogram it may be possible to obtain a useful estimate of the mean and standard deviation with less iterations. Figure 6.9 shows that the mean and standard deviations are relatively stable after considerably less iterations than needed to obtain stable histograms. As few as 2000 iterations may give a reasonable estimate, which is close to the practical limit of number of iterations for the forward model being used for the dispersion curve inversions.

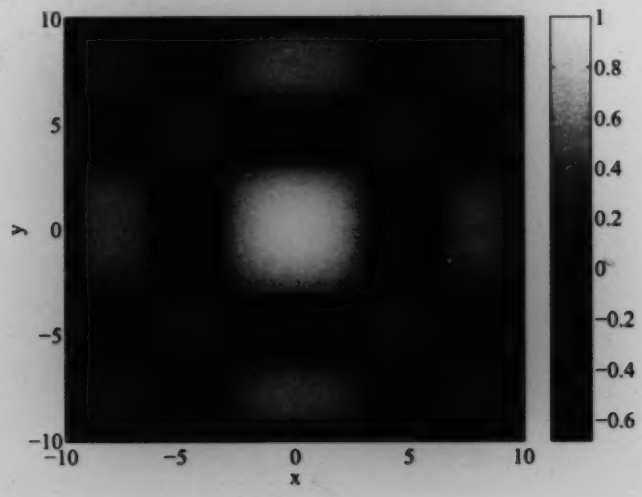

Figure 6.6: Simple example function defined in equation (6.68) used to test simulated annealing routine.

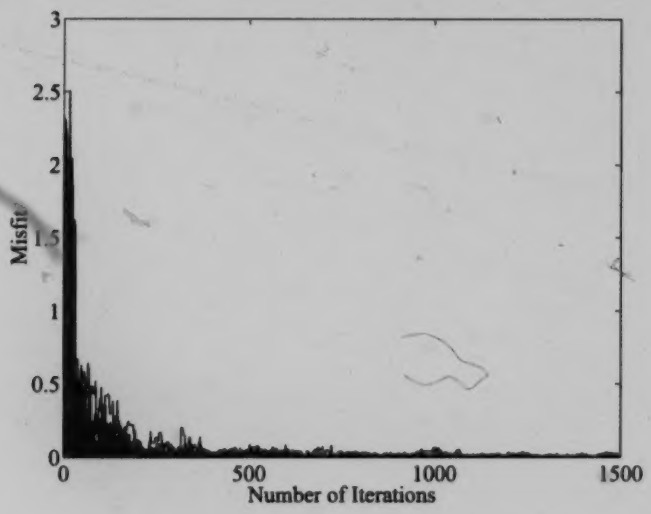

Figure 6.7: Misfit curves for 16 simulated annealing inversions of the example function using different random seeds. The starting temperature used was $T_0 = 20$.

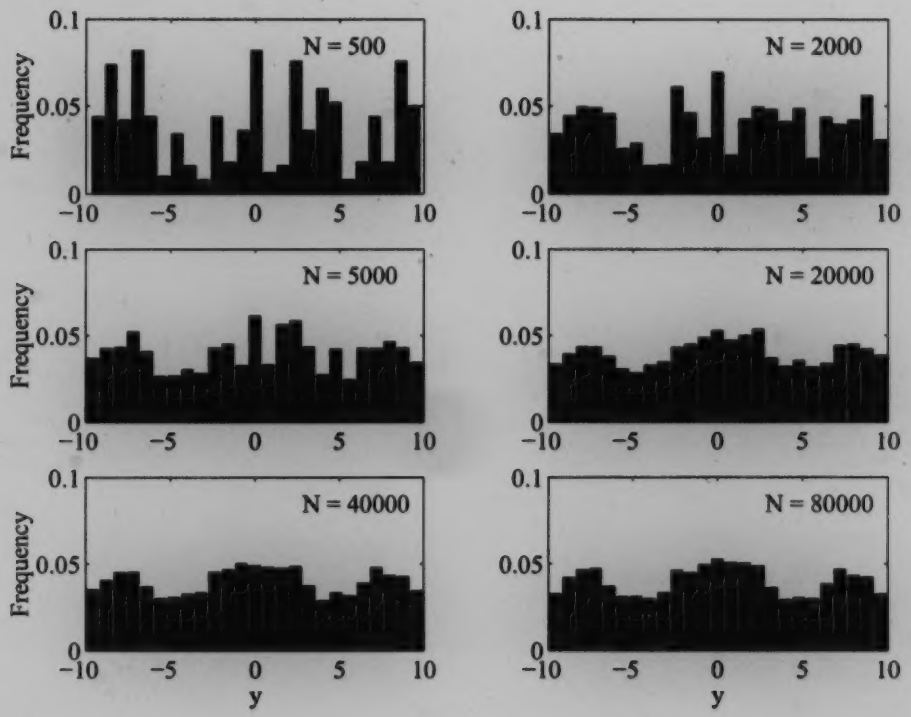

Figure 6.8: Histograms created using the Metropolis SA method for estimating uncertainty. The number of iterations used is shown in the top right corner of each plot.

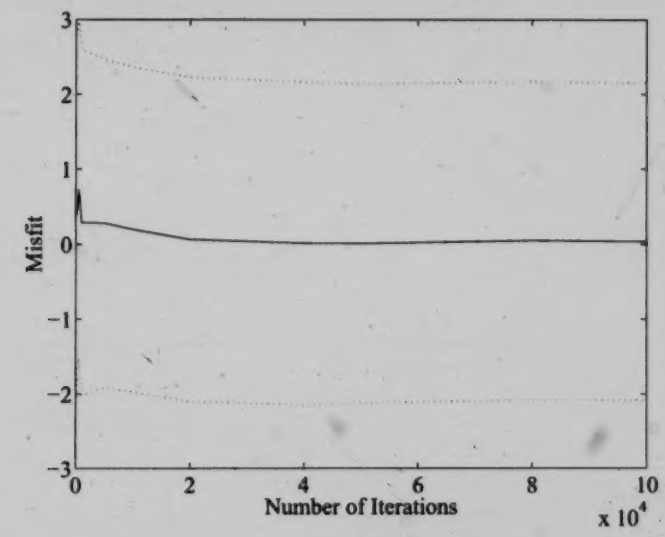

Figure 6.9: Mean (solid line) plus or minus one standard deviation (dotted lines) for the inversion results for the example function versus number of iterations of Metropolis SA used in estimating the mean and standard deviation.

6.2 Inversion results

Inversions were carried out first on a set of synthetic data generated using a simple layered profile that was loosely based on the velocity and density information for the Edmonton Research station obtained from the VSP profile and soil core measurements. The object of this inversion of synthetic dispersion curves was to determine the accuracy with which the shear-wave profile could be determined with depth and to test out the discretization scheme. This resolution information can later be related to the expected resolution of the inversion profiles from the observed dispersion curves.

Given the similarity in phase velocities between all of the survey dates and the

computational requirements of simulated annealing, the inversions of observed dispersion data were only performed on a single data set. The dispersion curve data obtained on September 9, 1999 were chosen because this data set was of high quality and dispersion information was available over a wider range of frequencies than most of the other data sets. Inversions on the real data were carried out using several different means of parameterizing the shear-wave velocity model. Sums of both 5 and 7 Chebyshev polynomials were employed to represent the velocity model as a smooth profile and the inversion was also performed where the velocities of each layer were sought.

Geotechnical engineering studies typically use 60-70 dispersion points from a single mode to invert for 10-15 layers. The number of points available for the September 9 fundamental mode dispersion curve falls within this range but the total number of points used in these inversions is greater as the additional phase velocities from the second and third modes are also employed.

A maximum depth of resolution for a Rayleigh wave dispersion survey is typically estimated as 0.5 to 1 times the maximum wavelength as a rule of thumb (Rix and Leipski, 1991). The September 9 data have a maximum wavelength of 40 m at a frequency of just below 10 Hz but preliminary inversion results show instability in resolving depths greater than about 12 m so this was chosen as the top of the infinite half-space for this study even though according to the rule of thumb it may be possible to image layers down to 20 m. Clearly there are limitations to this simple generalization but it is a useful first approximation.

Conversely, the minimum thickness that can be resolved immediately at the surface is expected to be half of the minimum wavelength recorded (Stokoe et al., 1994). This corresponds to a layer thickness of about 0.7 m for this survey. Thinner layers, however, will be used in the discretization of the profile because these rules of thumb were developed for surveys where only one mode was con-

sidered whereas in this study all three modes will be used in the inversions. The discretization of the model parameters was chosen as follows: thicknesses of 0.25 m down to 1.5 m, then 0.5 m thicknesses down to 5 m and 1 m down to 12 m for a total of 21 layers. This last layer is taken as an infinite half-space extending downwards from 12 m. This discretization scheme was adopted for the inversion of the synthetic as well as the experimental data.

6.2.1 Synthetic example

Inversions were carried out first on a simple test profile with a velocity and density structure (figure 6.10) similar to that of the Edmonton Research Station site as determined by the VSP profile and the soil bulk density measurements. Synthetic dispersion curves (figure 6.11) were calculated from the profiles and the inversion was carried out by inverting for the shear-wave velocities for each of the 21 layers used in the discretization scheme.

The theoretical dispersion curves found through the inversion match very closely, but not exactly, with the synthetic dispersion curves (figure 6.11). Certainly the theoretical curves are within the experimental error of the observed data at the Edmonton Research Station. The dispersion curves are calculated to a specified tolerance which has been set to ± 1 m/s, also within the experimental error of the surveys. The velocity profile found through inversion, however, does not match very well with the true profile below a depth of about 7 m (figure 6.10). Uncertainty analysis, carried out using 2480 iterations of Metropolis SA at $T = 1$, reveals that the velocities of layers at 8 m and below can only be very coarsely resolved. Standard deviations in this region are on the order of 400-500 m/s. The discrepancy between the velocity of the layer between 7 and 8 m found through inversion and that of the true profile is outside of the error region found through the uncertainty analysis. This is an indication that at a

depth of 7 m given a similar velocity profile, the depth to a transition can be resolved only to ± 1 m.

Agreement of the inverted parameters to the true profile is much better in the first 7 m. There are small fluctuations that are about 8 or 9 m/s from the true S-wave velocity in the topmost layer and from 3 to 42 m/s in the region from 0.75 m to 7 m. The uncertainty analysis in this region has underestimated error in most of these velocities in this region, a phenomenon which could be related to the small number of iterations used in the importance sampling. The uncertainty in depth, the lower resolution of the deeper layers, and the level of underestimation in the uncertainty of the upper layers should all be taken into consideration when interpreting the inversion profiles from the real data.

6.2.2 Inversion of experimental data

Inversions were carried out on the data obtained on September 9, 1999. This data set was of high quality and dispersion information was available over a wider range of frequencies than most of the other data sets. Given the similarity in phase velocities between all of the survey dates and the computational requirements of simulated annealing the inversions were only performed on this data set.

The starting model was chosen by fitting Chebyshev polynomials to the P- and S-wave profiles determined from the VSP survey and to the bulk density measurements made on the soil cores. The theoretical dispersion curves generated using these data provide a marginal fit to the fundamental mode (figure 6.12) but the phase velocities are too low in general and the shape of the curve is not the same in the low frequency region. The fit of the model to the second and third modes is much worse. The second and third mode data tend towards the theoretical second and third modes at low frequencies and towards the third and

fourth modes at higher frequencies. The model parameters used as the initial model are shown in figure 6.13. They have been discretized according to the 21 layer scheme mentioned earlier. Choosing an initial model that is close to the best fit solution is much more important for other inversion methods than for simulated annealing but starting close to the solution may allow the simulated annealing inversion to converge more quickly.

Several different methods of parameterizing the S-wave velocity profile were used in the inversion and compared. In several cases a sum of Chebyshev polynomials was used to represent the velocity profile and the inversion routine searched for the polynomial coefficients that corresponded to the best fit of the theoretical curve to the observed data. In another case the velocities for each layer were inverted for which is the method used in the synthetic example. The advantage of using the Chebyshev polynomials is that a smooth profile can be obtained at a much lower computational cost because fewer parameters must be resolved. The disadvantage is that sharp changes in velocity will not be imaged clearly. Inversion for a set of independent layers will be more computationally expensive and more sensitive to noise but will have the capability of imaging sharper velocity changes.

For one of the inversions, 5 Chebyshev coefficients were employed to represent the shear-wave velocity profile. The misfit curve for this inversion is shown in figure 6.14. The value of the error function changes very little after about 2000 iterations so the inversion likely could have been stopped much earlier. A very good match between the observed data and the theoretical dispersion curves is obtained (figure 6.15). Small discrepancies exist in the region between 30 and 60 Hz for the fundamental mode and at the low frequency end of the third mode (below 35 Hz). The reason for this latter discrepancy will be revisited later in this discussion.

The shear-wave velocity profile found through this inversion is displayed in figure 6.16 along with the P-wave and density profiles which were held constant. The resultant S-wave profile shows slightly higher velocities right at the surface followed by a slight decrease and then a gradual increase in velocity to a maximum of about 650 m/s.

Uncertainty runs on the Chebyshev profile yielded almost no variation in the polynomial coefficients and was thus not a good estimator of the resolution of the method with depth. Instead, uncertainty analysis as described earlier in the chapter was carried out on the discretized profiles allowing each layer to vary independently. The uncertainty analysis shows that the upper part of the profile is well resolved except for the topmost layer and the section from 4.5 to 5 m which have anomalous statistics. The mean values and standard deviations in the section from 7 to 10 m suggest that a faster transition to higher velocities than allowed by the polynomial parameterization may be favoured. Below 10 m the uncertainty increases drastically indicating a lack of resolving power of the data for these deeper layers. The depth resolution could be increased by placing more weight on the misfit of the lower frequency information but the most reliable way to deal with this problem in practice would be to use detectors sensitive to lower frequencies. The 10 Hz geophones used in this survey provide adequate amplitude only down to about 10 Hz.

A similar inversion was attempted using 7 Chebyshev coefficients to represent the S-wave velocity profile. For this inversion the P-wave velocity was also allowed to vary but it was only represented by one parameter which was the P- to S-wave velocity ratio, α/β. The use of additional polynomials in the inversion makes it possible to image features that vary more rapidly. The misfit curve for this inversion is shown in figure 6.17. The match between the observed and theoretical dispersion curves (figure 6.18) is better than in the 5 polynomial case

at the low frequency end, especially for the third mode. At the high frequency end, however, it is slightly worse for the fundamental and second modes. This may indicate that representation of the P-wave velocity profile by a single factor coupling it to the S-wave velocities may not be a good representation. The uncertainty estimates show that the resolution down to about 7 m is very good and then it abruptly deteriorates. The uncertainty in the P-wave profile shows that only a very narrow range of P-wave to S-wave velocity ratios will fit the data well for the inverted S-wave profile. The value of the α/β parameter was found to be 1.67 ± 0.04.

The inversion of the September 9 data set was also carried out by inverting directly for the shear-wave velocities for 21 layers. The match of the theoretical curve to the observed dispersion curve is closer than for either of the Chebyshev polynomial inversions (figure 6.20). The inverted shear-wave velocity profile (figure 6.21) does not show the increased velocity in the topmost layer as the Chebyshev profiles suggested. The profile is almost constant down to 4.5 m when there is a slight increase in velocity followed by a much larger jump at 8 m. The uncertainties in the velocities down to 8 m appear to be quite small. Below 8 m they increase substantially suggesting that the low velocity region observed between 10 and 11 m may not be a feature that can be resolved by the data.

To test this hypothesis the velocity profile was smoothed out below 8 m. The forward modelling using the smoothed profile (figure 6.22) is virtually identical to the one in figure 6.20 indicating that the low velocity feature is not required to describe the observed dispersion curve. The smoothed profile along with the P-wave and density profiles are shown in figure 6.23.

Further manipulation of the S-wave velocity profile showed that if the velocity was increased in the layer between 7 and 8 m then the match between the theoretical and observed dispersion curves for the third mode started to worsen

at frequencies below 35 Hz as observed in the case where 5 Chebyshev coefficients were used to represent the velocity profile. This suggests that there is a sharper increase in velocity at this point than the polynomials are capable of representing. Thus the velocity profile shown in figure 6.23 is probably the closest of all to the shape of the true profile but the exact value of the S-wave velocity below 8 m has a large error associated with it. The error in the depth to the top of this higher velocity layer could be as much as $\pm$ 1 m as indicated by the synthetic example.

This profile corresponds well with the geological profile determined from soil core analysis (table 4.1). The thin layer of top soil (0.3 m thick) is probably too thin to be resolved. The velocity profile down to about 4.5 m is close to a constant velocity. This region contains soils mixed with clay followed by clay. The slightly higher velocities from 4.5 to 7 m might be due to the increasing pressure on the clays or the presence of water but the change is very small and may not be significant. Between 7 and 8 m there is again a slight increase in velocity where the layer of wet sand was found in the soil core. Below 8 m ($\pm$1 m) there is strong evidence for a sharp velocity change corresponding to the top of the glacial tills which is at a depth of 8.5 m according to analysis of the soil core samples.

One further test was performed to attempt to find the region over which the high frequencies of the fundamental mode are important for resolution of the S-wave velocity profile. Figure 6.24 shows the the S-wave velocity profile found through the inversion for all 21 layers with the uncertainty analysis for two cases superimposed. The first case has taken all of the available data from all three modes into account. The second case represents the inclusion of only the fundamental mode dispersion curve data corresponding to frequencies greater than 30 Hz. These are the data points that are missing from the dispersion curves

obtained later in the summer of 1999. The erratic results from the uncertainty analysis in this case suggest that these data are most sensitive to the top 4 m and are much less sensitive below 4 m.

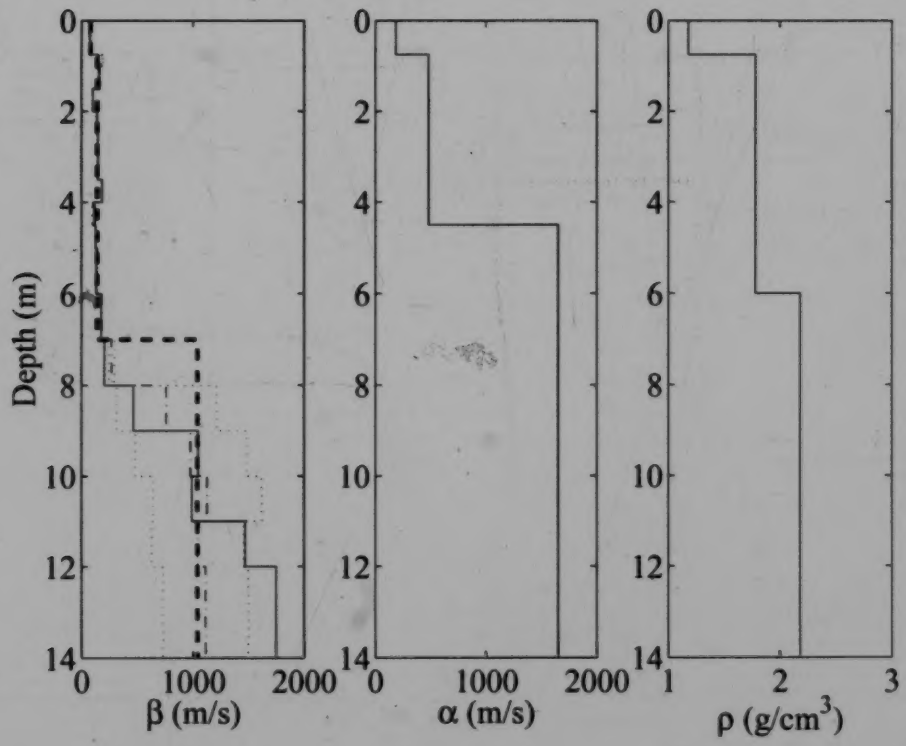

Figure 6.10: The shear-wave velocity profile (solid line) shown in the left panel is the result of an inversion where 21 independent layers were used to represent the profile. The heavy dotted line represents the shear-wave profile used to generate the synthetic data. The dash-dot curve and the dotted lines represent the mean and one standard deviation from the mean, respectively. The P-wave (middle) and density (right) profiles were held constant.

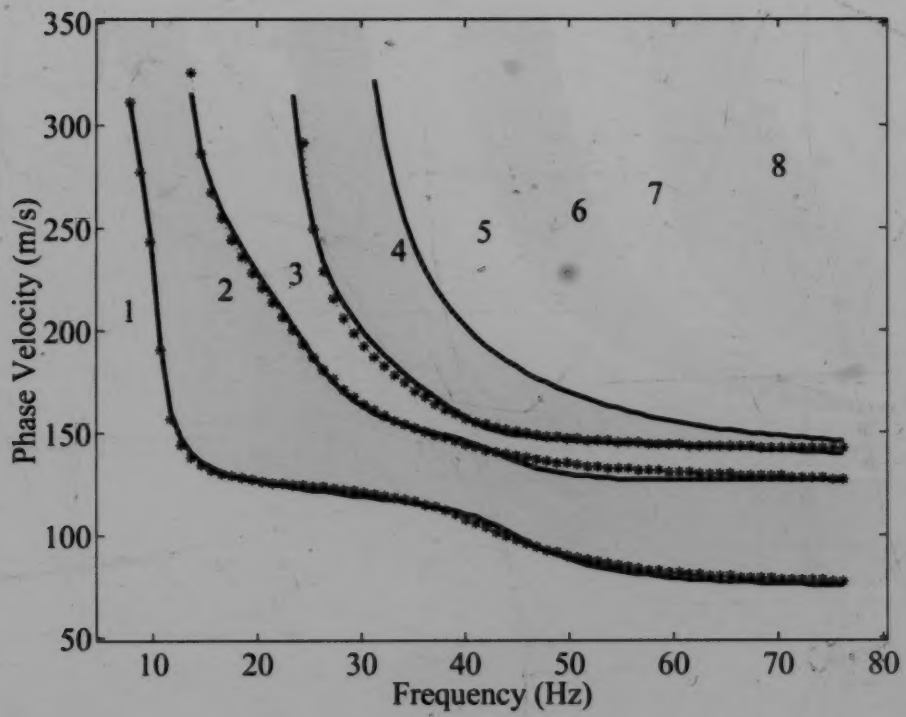

Figure 6.11: Inversion results using 21 independent layers to represent the theoretical shear-wave velocity profile of figure 6.10. White and gray bands represent positive and negative values of the dispersion function, respectively, with roots representing the various modes at the change in colour. The solid lines represent the roots of the dispersion function and the data are plotted as asterisks. The numbers on the image to the left of each mode indicate the mode order.

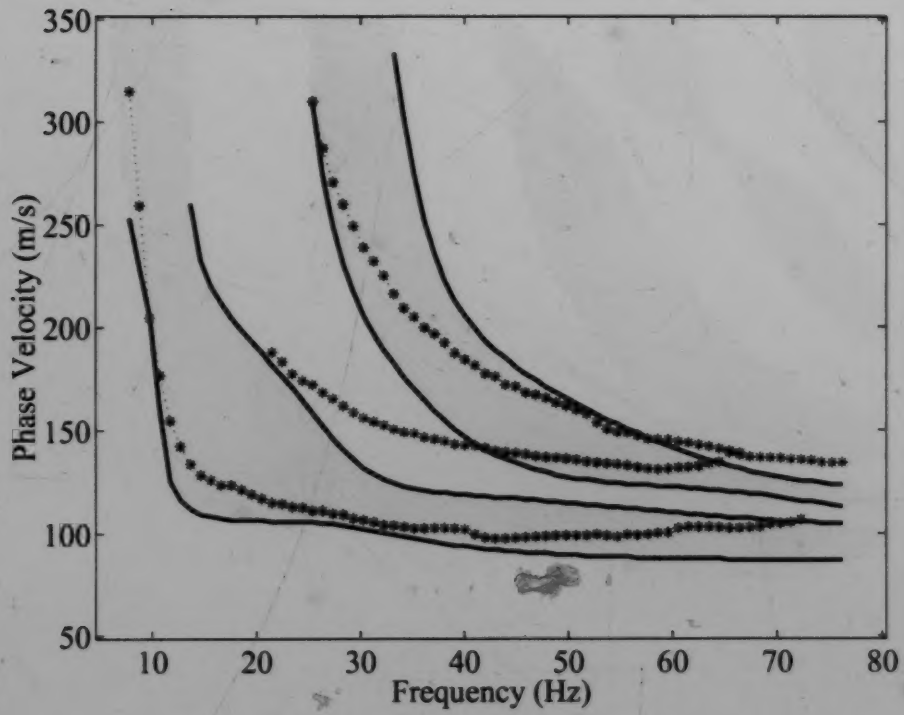

Figure 6.12: Theoretical dispersion curves corresponding to the initial model parameters used in the inversions. White and gray bands represent positive and negative values, respectively. The solid lines represent the roots of the dispersion function and the observed dispersion curves are plotted as asterisks.

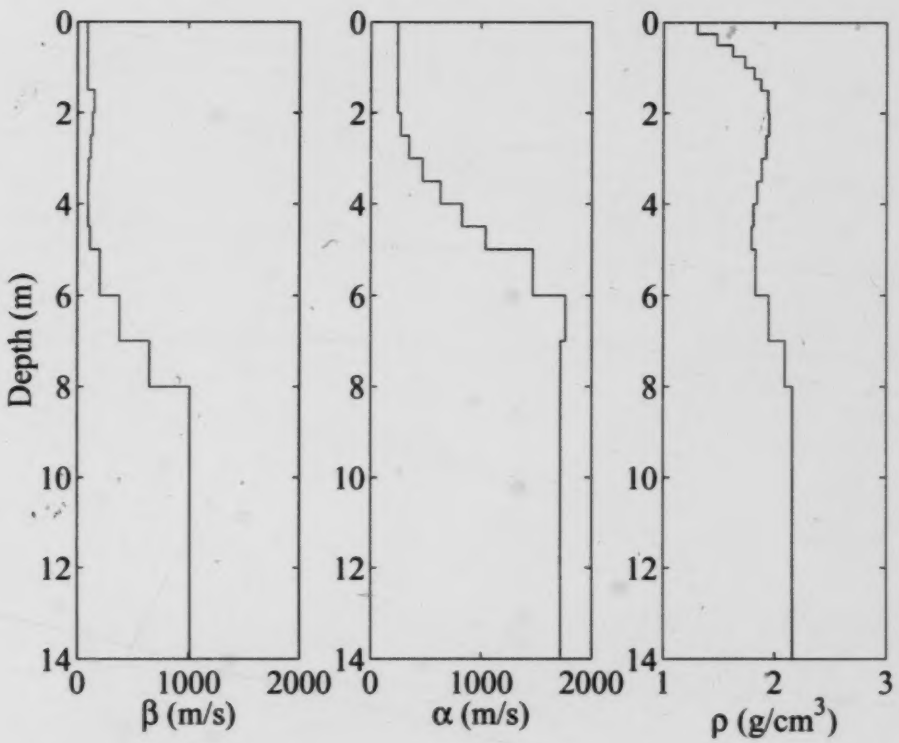

Figure 6.13: The S-wave velocity (left), P-wave velocity (middle) and density (right) profiles used as the initial model in the inversions.

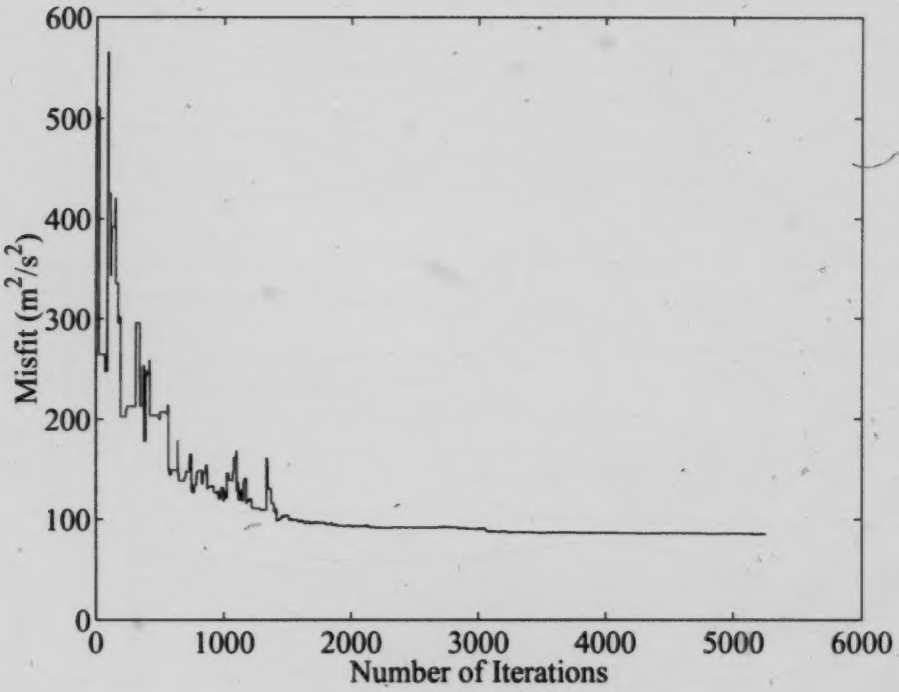

Figure 6.14: Misfit curve for the inversion performed using 5 Chebyshev polynomials to represent the shear-wave velocity profile.

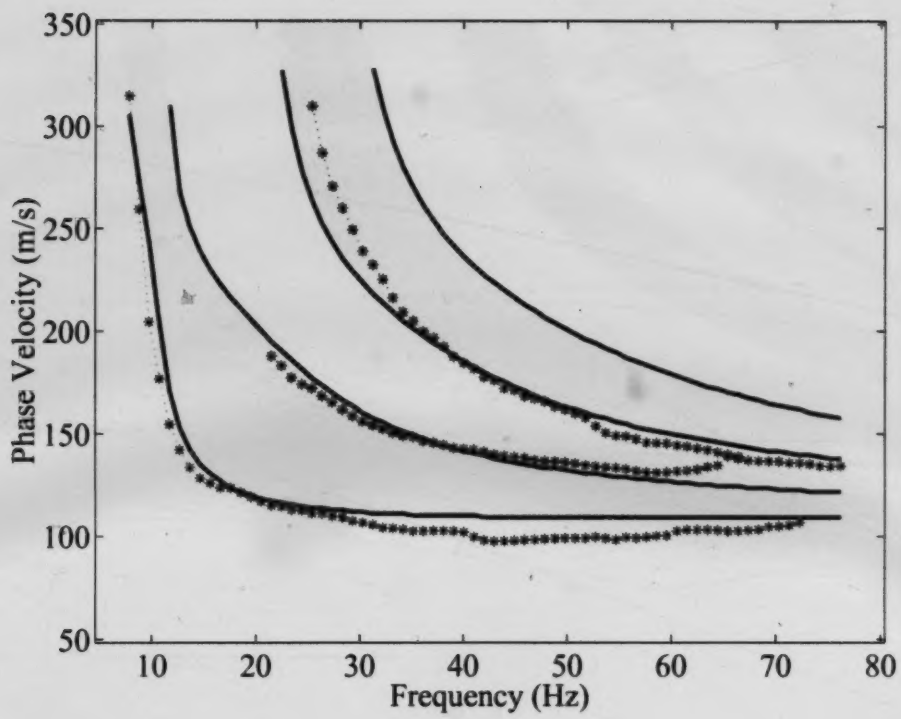

Figure 6.15: Inversion results using 5 Chebyshev polynomials to represent the shear-wave velocity profile. White and gray bands represent positive and negative values, respectively. The solid lines represent the roots of the dispersion function and the data are plotted as asterisks.

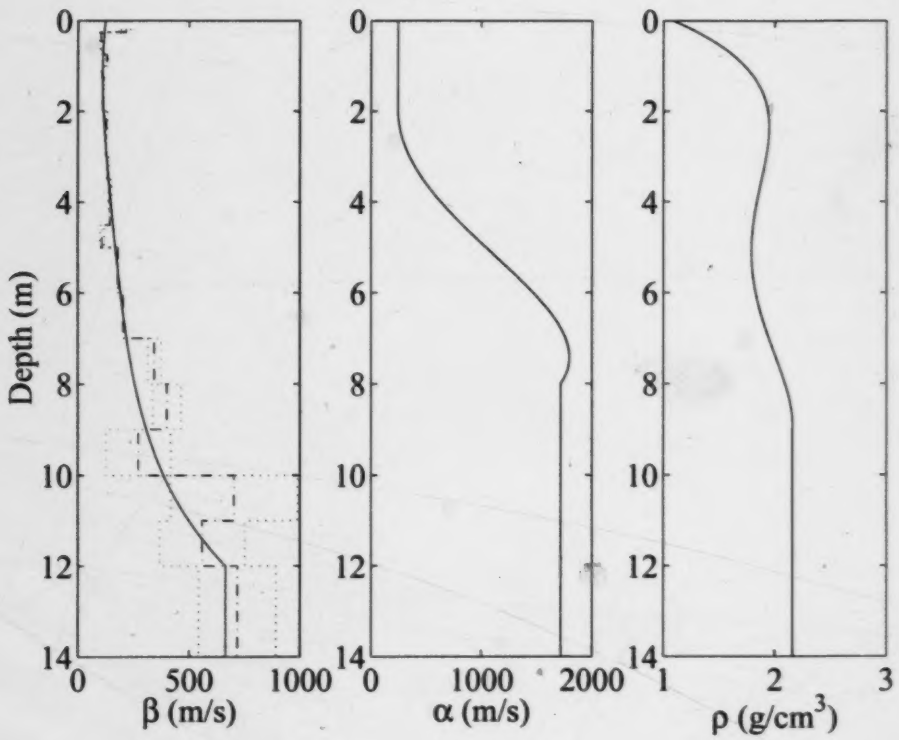

Figure 6.16: The shear-wave velocity profile shown in the left panel is the result of an inversion where 5 Chebyshev polynomials were used to represent the profile (solid line). The dash-dot curve and the dotted lines represent the mean and one standard deviation from the mean, respectively, found through the importance sampling technique. The *P*-wave (middle) and density (right) profiles were held constant.

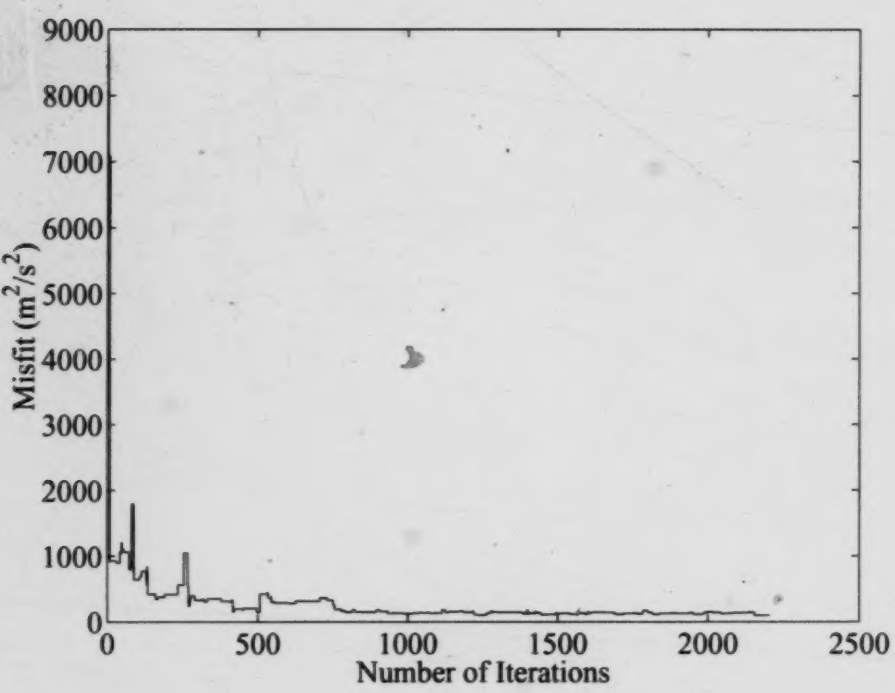

Figure 6.17: Misfit curve for the inversion performed using 7 Chebyshev polynomials to represent the shear-wave velocity profile and a multiplicative factor to represent the P-wave profile.

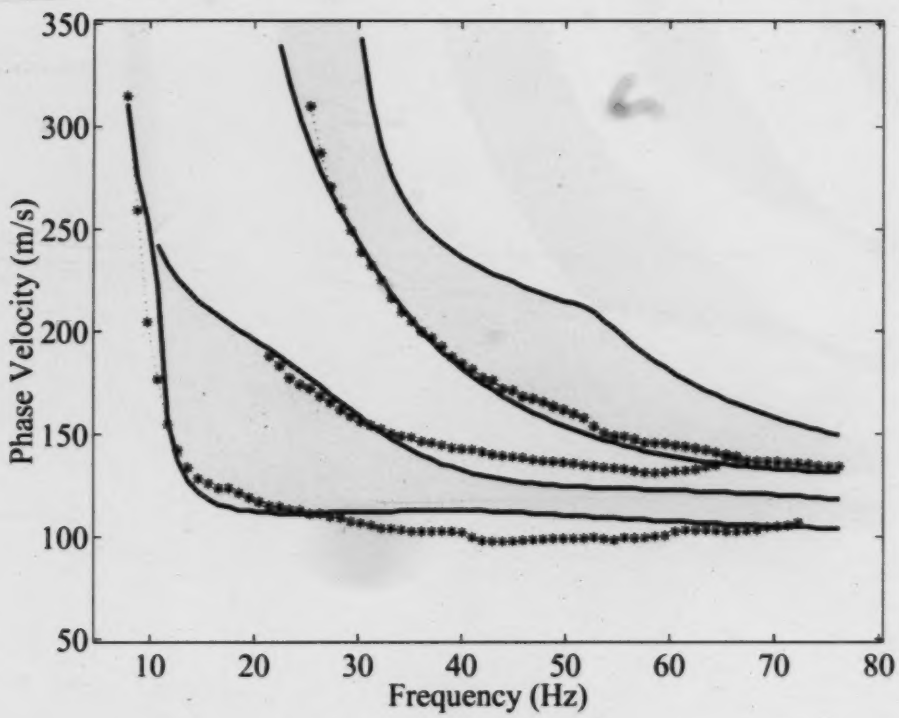

Figure 6.18: Inversion results using 7 Chebyshev polynomials to represent the shear-wave velocity profile and a multiplicative factor to represent the P-wave profile. White and gray bands represent positive and negative values, respectively. The solid lines represent the roots of the dispersion function and the data are plotted as asterisks.

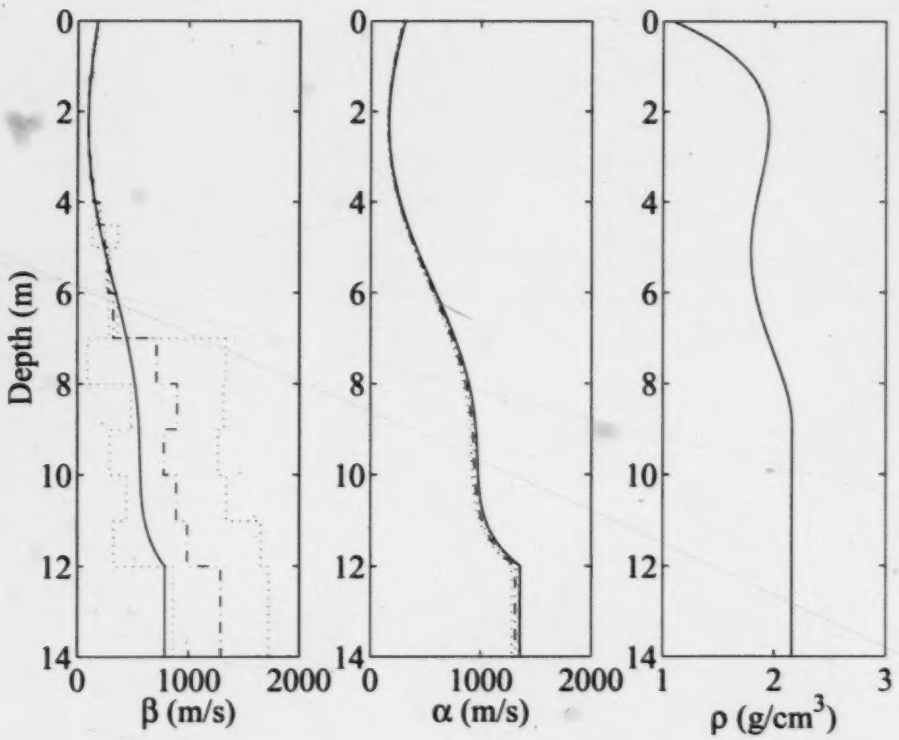

Figure 6.19: The shear-wave velocity profile shown in the left panel is the result of an inversion where 7 Chebyshev polynomials were used to represent the profile. The dash-dot curve and the dotted lines represent the mean and one standard deviation from the mean, respectively, found through the importance sampling technique. The *P*-wave profile (middle) was represented by a multiplicative factor and the density profile (right) was held constant.

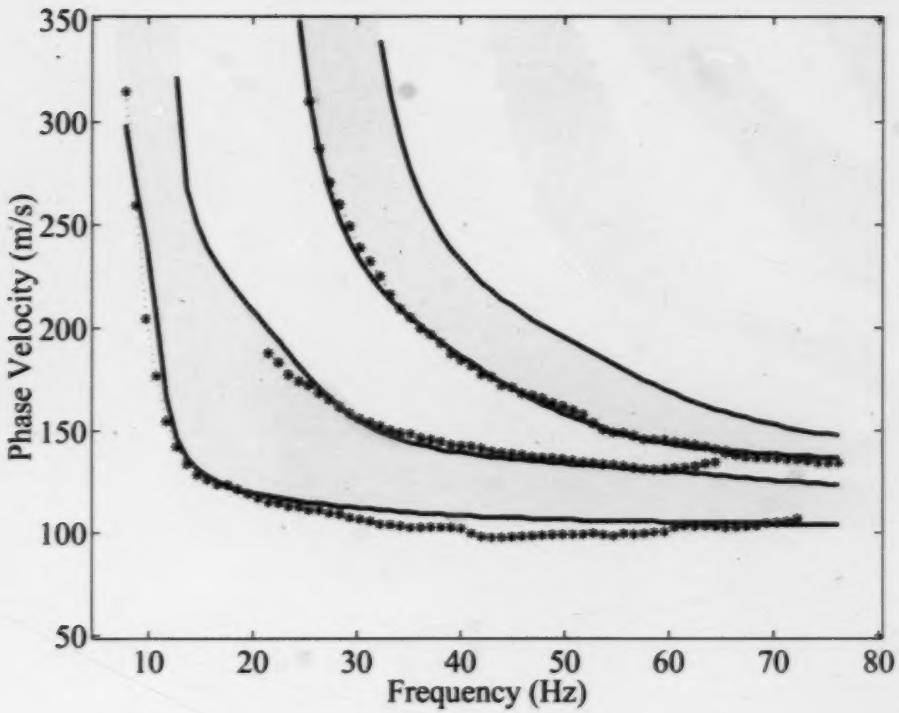

Figure 6.20: Inversion results using 21 independent layers to represent the shear-wave velocity profile. White and gray bands represent positive and negative values, respectively. The solid lines represent the roots of the dispersion function and the data are plotted as asterisks.

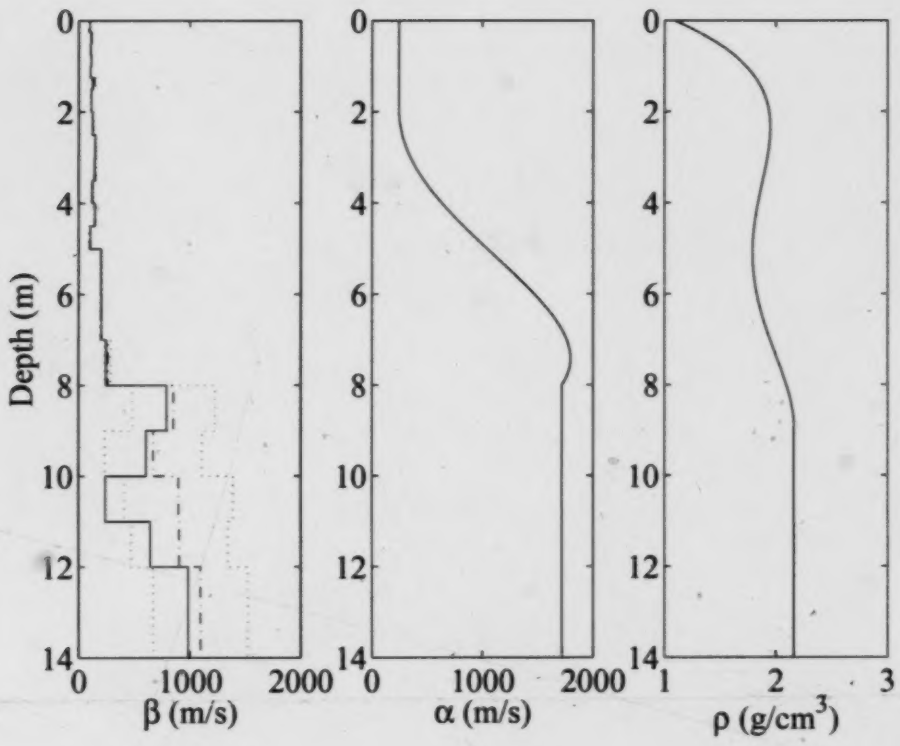

Figure 6.21: The shear-wave velocity profile shown in the left panel is the result of an inversion where 21 independent layers were used to represent the profile. The dash-dot curve and the dotted lines represent the mean and one standard deviation from the mean, respectively, found through the importance sampling technique. The *P*-wave (middle) and density (right) profiles were held constant.

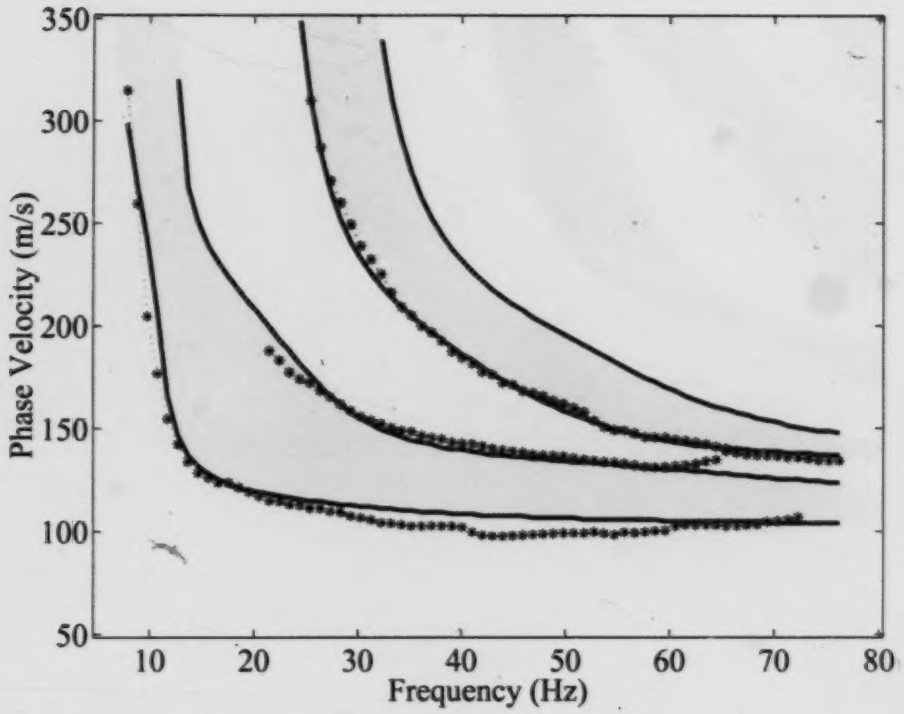

Figure 6.22: This figure shows the match of the theoretical data to the observed data when the shear-wave velocities below 8 m were perturbed in order to determine if the low velocity structure shown in figure 6.21 is required to achieve a good fit to the data. Notice that this figure looks virtually identical to figure 6.20. White and gray bands represent positive and negative values, respectively. The solid lines represent the roots of the dispersion function and the observed data are plotted as asterisks.

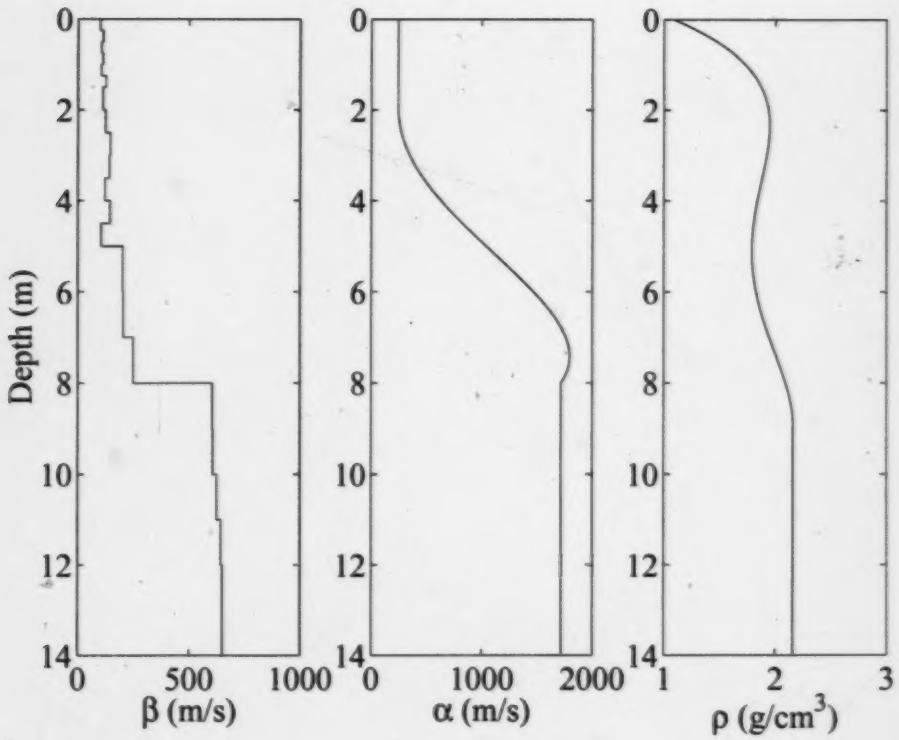

Figure 6.23: The shear-wave velocity profile shown in the left panel is the result of an inversion where 21 independent layers were used to represent the profile. The *P*-wave and density profiles were held constant. The shear-wave velocities have been perturbed at depths of greater than 8 m in order to determine if the structure found in this region by the inversion is real.

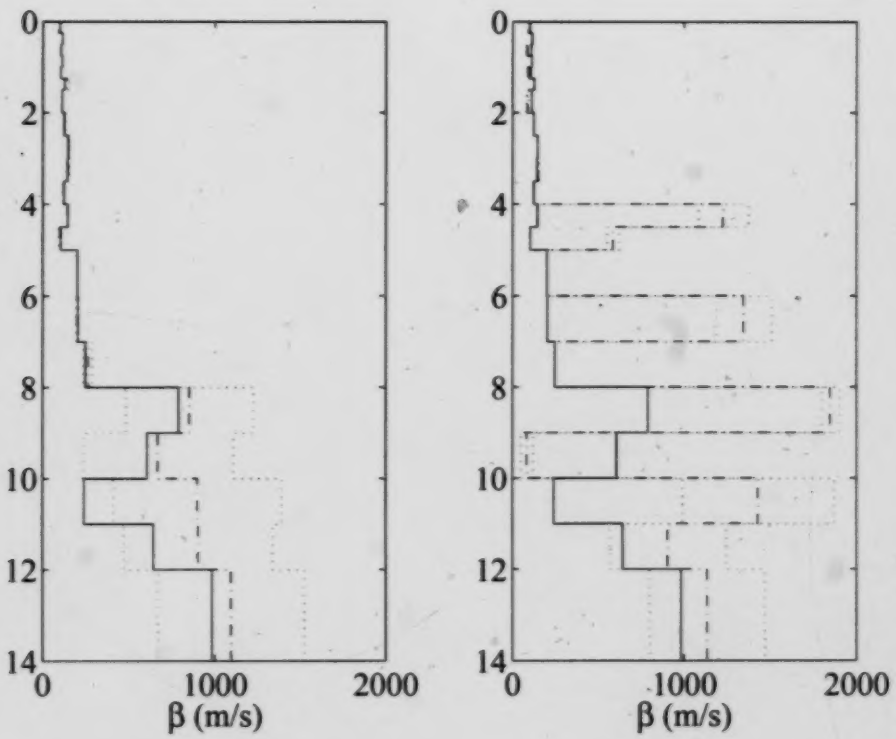

Figure 6.24: The shear-wave velocity profile shown in the left panel is the result of an inversion where 21 independent layers were used to represent the profile (previously shown in figure 6.21). The dash-dot curve and the dotted lines represent the mean and one standard deviation from the mean, respectively, found through the importance sampling technique. The profile on the right has the uncertainty analysis performed using only fundamental mode phase velocities above 30 Hz.

Chapter 7

Conclusions

In this study, Rayleigh wave dispersion was used to examine seasonal variability of the near-surface elastic properties at the Edmonton Research station throughout the summer and fall of 1999. The analysis of the data was divided up into two parts. The first step was to obtain reliable dispersion curves and the second step involved adapting a forward modelling methodology and an algorithm for the inversion of the dispersion curve data for shear-wave velocity profiles.

Before performing the dispersion analysis, two windowing techniques for isolating surface waves on a seismogram were compared and various methods for obtaining dispersion curves were tested on the surface wave data. It was determined that the time windowing method provides more reliable results overall. The $f-k$ windowing method results in an underestimation of phase velocities at low frequencies and can introduce artifacts if there are dead traces in the seismic section.

The methods for obtaining dispersion curves that were tested on the data included the phase comparison method (Dziewonski and Hales, 1972), the $f-k$ method (Gabriels et al., 1987; Nolet and Panza, 1976), and the $f-p$ method (McMechan and Yedlin, 1981; Park et al., 1998). This data set contains multiple

Rayleigh wave modes so the phase comparison method did not provide useful results. Both of the multi-channel methods yielded dispersion curves that agreed well but the $f-p$ method provided better overall resolution.

Dispersion analysis of the vertical component data indicates that there are three strong Rayleigh modes present, the phase velocities of which change very little between survey dates. Dispersion curves found using the 10 Hz and 14 Hz geophones are virtually identical except that the 10 Hz geophones provide data down to slightly lower frequencies (just below 10 Hz). The higher modes are not as clear in either of the horizontal component data sets but the fundamental mode dispersion curves show once again that the phase velocities have not changed significantly over the course of the study period. There is a general trend of decreasing phase velocity with increasing frequency for all dates examined, indicating that materials closer to the surface have slower shear-wave velocities.

The lack of change in phase velocities with time is a surprising result. Throughout the summer the near-surface materials are expected to be drying out which might suggest that the shear-wave velocities of the clays and soils might also vary substantially. It is worthwhile to note that the general consensus would assume (e. g. Gassmann) that the inclusion of a fluid might have a substantial effect on the P-wave velocity but not influence the shear-wave velocity at all, which is true for a porous medium but not necessarily for unconsolidated materials. The predominantly clay materials studied here, however, show little if any variation in Rayleigh wave phase velocity which means that there is probably very little variation in the intrinsic S-wave velocity during the summer despite the probable change in the water table levels with time. This implies that a change in the saturation state of such materials does not result in large changes in the shear properties (although it may influence the P-wave velocities but this was

not examined in this study). The standard "Gassmann" assumptions may also hold for such clay materials.

Although no variations in phase velocity were observed, there is a trend of progressively lower maximum frequencies for which fundamental mode dispersion information is available over the course of the summer, which suggests that there are changes in the attenuation properties of the near-surface materials in the top 1 - 2 m. Dispersion information is available over the widest range of frequencies at the beginning of the study period and for the very last survey (Sept. 9). There are also qualitative differences in the sharpness of the $f - p$ images and the relative amounts of energy contained in the three modes which may also be related to changes in the attenuative properties of the near-surface materials. This survey was not designed to examine attenuation effects so only qualitative observations can be made at this time. This is an area that would be interesting to examine in future studies. Careful measurements of soil moisture content should be made concurrently with any attenuation studies attempted.

Inversion of the three Rayleigh mode dispersion curves using a fast simulated annealing algorithm (Sen and Stoffa, 1995) coupled with a matrix propagator forward modelling technique (Menke, 1979) yields S-wave velocity profiles that agree well with geological information. Resolution of the inverted velocity profiles is excellent down to a depth of about 8 m after which the uncertainty increases to about 400 m/s for a velocity of slightly less than 1000 m/s.

The inversions carried out using Chebyshev polynomials to represent the velocity profiles tend to be faster and more stable than profiles represented by a set of discrete independent layers. The inversion results where each of the layers has been allowed to vary independently, however, produce a smaller misfit overall which suggests that the velocity transition at around 8 m is likely a more rapid change than that allowed by the Chebyshev profiles. This sharp change is con-

sistent with the lithological boundary between the lacustrine deposits and the underlying glacial tills. Sources of error include inaccuracies in receiver placement, in the P-wave and density profiles assumed for the inversion, and in the assumption that the geology is a set of homogeneous and isotropic layers.

Simulated annealing has proven to be quite useful for determining velocity profiles from dispersion curve data but is computationally quite expensive. There are several other methods of inversion that may be worthy of examination for future work in this area. The variational method (Takeuchi and Saito, 1972; Aki and Richards, 1980) offers a linearization of the problem that is more accurate than finding partial derivatives of the dispersion curve using numerical techniques (Novotný, 1976). Perhaps a Hedgehog type method, as suggested by Kennett (1976) would provide the best compromise between linear and nonlinear inversion techniques.*

Improvements in the understanding of seismic properties of the near surface are beneficial to environmental and geotechnical fields. In Alberta this method could be useful for mapping out the depth to the top of the glacial tills and the thickness of the clay layer which may be useful for slope stability assessment. This is also important for exploration seismology where knowing the effects of the near surface on the seismic waves would make it possible to improve static corrections and obtain clearer images of the deeper subsurface. This research will also help to ensure the validity of time-lapse seismic studies where it is important to be able to isolate the contributions of a target region to the seismogram. Methods of evaluating and accounting for changes in the effects of the near-surface on the seismograms is essential because there is no way of avoiding them unless

*For a Hedgehog type method a model is chosen through a Monte Carlo technique and then the area surrounding the model in parameter space is tested using the linearized formulation of the problem until the boundary of solutions that are compatible with the data is mapped out. A new area is chosen through Monte Carlo and the procedure is repeated.

geophones can be buried which can be quite costly.

Future areas of research that should be considered include designing a survey better able to examine attenuative properties, incorporating attenuation into the forward modelling and inversion algorithms, and expanding the knowledge base on near-surface properties with complimentary laboratory studies dealing with the effects of saturation state on materials. Also, the use of lower frequency geophones would increase the depth of investigation while a shear-wave source could be used to improve the generation of Love waves which could be used in conjunction with Rayleigh waves to improve the reliability of the inverted shear wave velocity profiles.

References

Abo-Zena, A., 1979, Dispersion function computations for unlimited frequency values: Geophys. J. Roy. Astr. Soc., **58**, 91–105.

Aki, K., and Richards, P. G., 1980, Quantitative seismology: W. H. Freeman and Co.

Arfken, G. B., and Weber, H. J., 1995, Mathematical methods for physicists, forth edition: Academic Press Inc.

Bachrach, R., and Nur, A., 1998, High-resolution shallow-seismic experiments in sand, part i: Water table, fluid flow, and saturation: Geophysics, **63**, 1225–1233.

Bolt, B. A., 1976, Nuclear explosions and earthquakes: The parted veil: W. H. Freeman and Co.

Burger, H. R., 1992, Exploration geophysics of the shallow subsurface: Prentice-Hall, Inc.

Chernick, M. R., 1999, Bootstrap methods; A practitioner's guide: John Wiley & Sons, Inc.

Chunduru, R. K., Sen, M. K., and Stoffa, P. L., 1996, 2-D resistivity inversion using spline parameterization and simulated annealing: Geophysics, **61**, 151–161.

Dahlen, F. A., and Tromp, J., 1998, Theoretical global seismology: Princeton Univ. Press.

Deans, S. R., 1983, The Radon transformation and its applications: John Wiley & Sons, Inc.

Dobrin, M. B., 1951, Dispersion in seismic surface waves: Geophysics, **16**, 63–80.

Dziewonski, A. M., and Hales, A. L., 1972, Numerical analysis of dispersed seismic waves: Methods in Computational Physics, **11**, 39–85.

Dziewonski, A. M., and Steim, J. M., 1982, Dispersion and attenuation of mantle waves through waveform inversion: Geophys. J. Roy. Astr. Soc., **70**, 503–527.

Dziewonski, A. M., Landisman, M., Bloch, S., Satô, Y., and Asano, S., 1968, Progress report on recent improvements in the analysis of surface wave observations: J. Phys. Earth, **16**, 1–26.

Dziewonski, A. M., 1970, Dispersion of mantle Rayleigh waves: Geophys. J. Roy. Astr. Soc., **22**, 289–325.

Dziewonski, A. M., 1971, Upper mantle models from "pure-path" dispersion data: J. Geophys. Res., **76**, 2587–2601.

Edmonton Geological Society, 1993, Edmonton beneath our feet: Edmonton Geol. Soc.

Efron, B., and Tibishirani, R., 1993, An introduction to the bootstrap: Chapman and Hall.

Ewing, W. M., Jardetzky, W. S., and Press, F., 1957, Elastic waves in layered media: McGraw-Hill Book Co.

Forsyth, D., Webb, S. C., Dorman, L. M., and Shen, Y., 1998, Phase velocities of Rayleigh waves on the East Pacific Rise: Science, **280**, 1235–1238.

Fowler, C. M. R., 1990, The solid earth: Cambridge Univ. Press.

Gabriels, P., Snieder, R., and Nolet, G., 1987, In situ measurement of shear-wave velocity in sediments with higher-mode Rayleigh waves: Geophys. Prosp., **35**, 187–196.

Ganji, V., Gucunski, N., and Nazarian, S., 1998, Automated inversion procedure for spectral analysis of surface waves: J. Geotech. Geoenv. Eng., **124**, 757–770.

Gardner, G. F., and Lu, L., 1991, Slant-stack processing: Soc. Expl. Geophys.

Geman, S., and Geman, D., 1984, Stochastic relaxation, Gibb's distribution and Bayesian restoration of images: IEEE Trans., **PAMI-6**, 721–741.

Ghosh, D. P., 1971, Inverse filter coefficients for the computation of apparent resistivity standard curves for a horizontally stratified earth: Geophys. Prosp., **19**, 769–775.

Gould, H., and Tobochnik, J., 1996, An introduction to computer simulation methods; Applications to physical systems: Addison-Wesley Publ. Co.

Grechka, V. Y., McMechan, G. A., and Volovodenko, V. A., 1996, Solving 1-d inverse problems by Chebyshev polynomial expansion: Geophysics, **61**, 1758–1768.

Gucunski, N., and Woods, R. D., 1991, Instrumentation for SASW testing, *in* Bhatia, S. K., and Blaney, G. W., Eds., Recent advances in instrumentation, data acquisition and testing in soil dynamics: Am. Soc. Civ. Eng., 1–16.

Haskell, N. A., 1953, The dispersion of surface waves on multilayered media: Bull., Seis. Soc. Am., **43**, 17–24.

Head, K. H., 1980, Manual of soil laboratory testing: Pentech Press.

Hiltunen, D. R., and Gucunski, N., 1994, Annotated bibliography of SASW method, *in* Woods, R. D., Ed., Technical review: Geophysical characterization of sites: Oxford Publishers, 27–34.

Hunter, J. A., Pullan, S. E., R.A.Burns, R. A., Good, R. L., Harris, J. B., Pugin, A., Skvortsov, A., and Goriainov, N. N., 1998, Downhole seismic logging for high-resolution reflection surveying in unconsolidated overburden: Geophysics, **63**, 1371–1384.

Ingber, L., 1989, Very fast simulated re-annealing: Mathl. Comput. Modeling, **12**, 967–993.

Jefferson, R. D., Steeples, D. W., Black, R. A., and Carr, T., 1998, Effects of soil-moisture content on shallow-seismic data: Geophysics, **63**, 1357–1362.

Kathol, C. P., and McPherson, R. A., 1975, Urban geology in Edmonton, bulletin 32: Alberta Research Council.

Kausel, E., and Peek, R., 1982, Dynamic loads in the interior of a layered stratum: An explicit solution: Bull., Seis. Soc. Am., **72**, 1459–1481.

Kausel, E., and Roesset, J. M., 1981, Stiffness matrices for layered soils: Bull., Seis. Soc. Am., **71**, 1743–1761.

Kearney, P., and Brooks, M., 1995, An introduction to geophysical exploration: Blackwell Scientific Publications, Inc.

Kennett, B. L. N., 1976, The inversion of surface wave data: Pure Appl. Geophysics, **114**, 747–751.

Kirkpatrick, S., Gelatt Jr., C. D., and Vecchi, M. P., 1983, Optimization by simulated annealing: Science, **220**, 671–680.

Knopoff, L., 1964, A matrix method for elastic wave propagation: Bull., Seis. Soc. Am., **54**, 431–438.

Koefoed, O., 1979, Geosounding principles, 1: Resistivity sounding measurements: Elsevier Science Publ. Co., Inc.

Kostov, C., 1990, Toeplitz structure in slant-stack inversion: 60th Ann. Internat. Mtg., Soc. Expl. Geophys., Expanded Abstracts, 1618–1621.

Laske, G., and Masters, G., 1996, Constraints on global phase velocity maps by long-period polarization data: J. Geophys. Res., **101**, 16,059–16,075.

Lay, T., and Wallace, T. C., 1995, Modern global seismology: Academic Press Inc.

Lizarralde, D., and Swift, S., 1999, Smooth inversion of VSP traveltime data: Geophysics, **64**, 659–661.

Long, L., Chen, X., Doll, W., Kocaoglu, A., and Martin, J., 1999, Surface-wave group-velocity tomography applied to shallow structures at a waste site: 69th Ann. Internat. Mtg., Soc. Expl. Geophys., Expanded Abstracts, 496–499.

Mavko, G., Mukerji, T., and Dvorkin, J., 1998, The rock physics handbook: Tools for seismic analysis in porous media: Cambridge Univ. Press.

McCormick, G. P., 1983, Nonlinear programming: John Wiley & Sons, Inc.

McMechan, G. A., and Yedlin, M. J., 1981, Analysis of dispersive waves by wave-field transformation: Geophysics, **46**, 869–874.

Menke, W., 1979, Comment on 'Dispersion function computations for unlimited frequency values' by Anas Abo-Zena: Geophys. J. Roy. Astr. Soc., **59**, 315–323.

Menke, W., 1984, Geophysical data analysis: Discrete inverse theory, revised edition: Academic Press Inc.

Metropolis, N., Rosenbluth, A., Rosenbluth, M., Teller, A., and Teller, E., 1953, Equation of state calculations by fast computing machines: J. Chem. Phys., **21**, 1087–1092.

Miller, R., Xia, J., Park, C., Ivanov, J., and Williams, E., 1999a, Using MASW to map bedrock in olathe, kansas: 69th Ann. Internat. Mtg., Soc. Expl. Geophys., Expanded Abstracts, 433–436.

——— 1999b, Seismic techniques to delineate dissolution features in the upper 1000 ft at a power plant site: 69th Ann. Internat. Mtg., Soc. Expl. Geophys., Expanded Abstracts, 492–495.

——— 1999c, Multichannel analysis of surface waves to map bedrock: The Leading Edge, **18**, no. 12, 1392–1396.

Molyneux, J., and Schmitt, D. R., 2000, Travel-time determination in attenuative media: A physical modeling study: Geophysics, **in press**.

Nazarian, S., and Stokoe, K. H., 1985, In-situ stiffnesses of pavement systems by surface wave method: 53rd Ann. Internat. Mtg., Soc. Expl. Geophys., Expanded Abstracts, 140–142.

Nazarian, S., and Stokoe, K. H., 1986, Use of surface waves in pavement evaluation: Transportation Research Record, **1070**, 132–144.

Nazarian, S., Stokoe, K. H., and Hudson, W. R., 1983, Use of spectral analysis of surface waves method for determination of moduli and thicknesses of pavement systems: Transportation Research Record, **930**, 38–45.

Nishimura, C. E., and Forsyth, D. W., 1989, The anisotropic structure of the upper mantle in the Pacific: Geophys. J., **96**, 203–229.

Nolet, G., and Panza, G. F., 1976, Array analysis of seismic surface waves: Limits and possibilities: Pure Appl. Geophysics, **114**, 775–790.

Novotný, O., 1976, Methods of computing the partial derivatives of dispersion curves: Pure Appl. Geophysics, **114**, 765–773.

Park, C. B., Miller, R. D., and Xia, J., 1998, Imaging dispersion curves of surface waves on multi-channel record: 68th Ann. Internat. Mtg., Society Of Exploration Geophysicists, Expanded Abstracts, 1377–1380.

Park, C., Miller, R., Hunter, J., Xia, J., and Harris, J., 1999a, Higher mode observation by the MASW method: 69th Ann. Internat. Mtg., Soc. Expl. Geophys., Expanded Abstracts, 524–527.

—— 1999b, Multichannel analysis of surface waves: Geophysics, **64**, 800–808.

Press, W. H., Teukolsky, S. A., Vetterling, W. T., and Flannery, B. P., 1997, Numerical recipes in C: The art of scientific computing: Cambridge Univ. Press.

Radon, J., 1917, Uber die Bestimmung von Funktionen durch ihre Integralwerte langs gewisser Manningfaltigkeiten: Berichte der Sachischen Akedemie der Wissenschaften, **69**, 262–277.

Rix, G. J., and Leipski, E. A., 1991, Accuracy and resolution of surface wave inversion, *in* Bhatia, S. K., and Blaney, G. W., Eds., Recent advances in instrumentation, data acquisition and testing in soil dynamics: Am. Soc. Civ. Eng., 17–32.

Robertson, P. K., and Fear, C. E., 1994, Borehole geophysics: basic concepts and geotechnical engineering applications, *in* Woods, R. D., Ed., Technical review: Geophysical characterization of sites: Oxford Publishers, 63–68.

Roth, M., and Holliger, K., 1999, Inversion of source-generated noise in high-resolution seismic data: The Leading Edge, **18**, 1402–1404, 1406.

Schwab, F. A., and Knopoff, L., 1970, Surface-wave dispersion computations: Bull., Seis. Soc. Am., **60**, 321–344.

Schwab, F. A., and Knopoff, L., 1972, Fast surface wave and free mode computations: Methods in Computational Physics, **11**, 87–180.

Schwab, F. A., 1970, Surface-wave dispersion computations: Knopoff's method: Bull., Seis. Soc. Am., **60**, 1491–1520.

Sen, M., and Stoffa, P. L., 1995, Global optimization methods in geophysical inversion: Elsevier Science Publ. Co., Inc.

Sharma, P. V., 1997, Environmental and engineering geophysics: Cambridge Univ. Press.

Shearer, P. M., 1999, Introduction to seismology: Cambridge Univ. Press.

Stokoe, K. H., and Nazarian, S., 1985, Use of Rayleigh waves in liquefaction studies, *in* Woods, R. D., Ed., Measurement and use of shear wave velocity for evaluating dynamic soil properties: Am. Soc. Civ. Eng., 1–17.

Stokoe, K. H., Wright, S. G., Bay, J. A., and Roësset, J. M., 1994, Characterization of geotechnical sites by SASW, *in* Woods, R. D., Ed., Technical review: Geophysical characterization of sites: Oxford Publishers, 15–26.

Szu, H., and Hartley, R., 1987, Fast simulated annealing: Phys. Lett. A, **122**, 157–162.

Takeuchi, H., and Saito, M., 1972, Seismic surface waves: Methods in Computational Physics, **11**, 217–295.

Telford, W. M., Geldart, L. P., Sherrif, R. E., and Keys, D. A., 1976, Applied geophysics: Cambridge Univ. Press.

The MELT Seismic Team, 1998, Imaging the deep seismic structure beneath a mid-ocean ridge: the MELT experiment: Science, **280**, 1215–1217.

Thomson, W. T., 1950, Transmission of elastic waves through a stratified solid medium: J. Appl. Phys., **21**, 89–93.

Tokimatsu, K., Tamura, S., and Kojima, H., 1992, Effects of multiple modes on Rayleigh wave dispersion characteristics: J. Geotech. Eng., **118**, 1529–1543.

Toksöz, M. N., and Anderson, D. L., 1966, Phase velocities of long-period surface waves and structure of the upper mantle; 1. Great-circle Love and Rayleigh wave data: J. Geophys. Res., **71**, 1649–1658.

Turner, G., 1990, Aliasing in the tau-p transform and the removal of spatial aliased coherent noise: Geophysics, **55**, 1496–1503.

Watson, T. H., 1970, A note on fast computation of Rayleigh wave dispersion in the multilayered elastic half-space: Bull., Seis. Soc. Am., **60**, 161–166.

Wiggins, R. A., 1972, The general linear inverse problem: Implication of surface waves and free oscillations for Earth structure: Rev. of Geophys. and Space Phys., **10**, 251–285.

Wiggins, R. A., 1976, A fast, new computational algorithm for free oscillations and surface waves: Geophys. J. Roy. Astr. Soc., **47**, 135–150.

Wolf, J. P., 1985, Dynamic soil-structure interaction: Prentice-Hall, Inc.

Woods, R. D., 1994, Borehole methods in shallow seismic exploration, *in* Woods, R. D., Ed., Technical review: Geophysical characterization of sites: Oxford Publishers, 91–100.

Xia, J., Miller, R., Hunter, J., Park, C., and Harris, J., 1999a, Evaluation of the MASW technique in unconsolidated sediments: 69th Ann. Internat. Mtg., Soc. Expl. Geophys., Expanded Abstracts, 437–440.

—— 1999b, Estimation of near-surface shear-wave velocity by inversion of Rayleigh waves: Geophysics, **64**, 691–700.

Yang, S. Y., Castagna, J. P., Black, R. A., and Knapp, R. W., 1989, Sensitivity of near-surface shear-wave velocity determination from Rayleigh and Love waves: 59th Ann. Internat. Mtg., Soc. Expl. Geophys., Expanded Abstracts, 509–512.

Appendix A

Chebyshev Polynomials

Chebyshev polynomials (type 1) are primarily important for numerical analysis (Arfken and Weber, 1995). In geophysics they have been used to reduce the number of parameters needed to represent a resistivity profile (Grechka et al., 1996) or a velocity profile in an inversion (see Chapter 2). They combine the useful features of Fourier series and orthogonal polynomials allowing for a larger average squared error than a least-squares approximation combined with better avoidance of extreme errors. Chebyshev polynomials are solutions to Chebyshev's differential equation

$$(1-x^2)\frac{d^2f}{dx^2} - x\frac{df}{dx} + n^2 f = 0 \tag{A.1}$$

where $n = 1, 2, 3, \cdots$. The general solution is given by

$$f = c_1 T_n(x) + c_2\sqrt{1-x^2}U_{n-1}(x) \tag{A.2}$$

where c_i are constants and T_n and U_{n-1} are Chebyshev polynomials of types 1 and 2 respectively. Chebyshev polynomials of type 1 can be generated using the following recursion relation

$$T_{n+1}(x) - 2xT_n(x) + T_{n-1}(x) = 0 \tag{A.3}$$

along with the known values

$$T_0(x) = 1 \tag{A.4}$$

and

$$T_1(x) = x \tag{A.5}$$

These polynomials are valid in the range $-1 \leq x \leq 1$ with $-1 \leq T_n(x) \leq 1$.

For geophysical applications, shifted Chebyshev polynomials $T_n^*(z)$, with $0 \leq z \leq 1$, are often more convenient for representing the variation of a parameter with depth. The set of shifted Chebyshev polynomials can be obtained by setting $x = 2z - 1$, which gives

$$T_{n+1}^*(z) - 2(2z-1)T_n^*(z) + T_{n-1}^*(z) = 0, \tag{A.6}$$

$$T_0^*(z) = 1 \tag{A.7}$$

and

$$T_1^*(z) = 2z - 1. \tag{A.8}$$

The solutions for $n = 1$ to 4 are shown in figure A.1. In the body of the thesis and for the remainder of this appendix shifted Chebyshev polynomials will be used so the asterisk superscript will be omitted.

A finite set of Chebyshev polynomials can be used to approximate a function $f(z)$ if the function belongs to the Hilbert space $L_w^2[0,1]$ with a real weighting function $W(z) = \sqrt{z(1-z)}$ (Grechka et al., 1996). This can be expressed as

$$f(z) = \sum_{k=1}^{N} f_k T_{k-1}, \ (0 \leq z \leq 1) \tag{A.9}$$

where f_k are the coefficients of the series and T_k are orthonormal Chebyshev polynomials (type 1). Alternately, if points at z_i on a function $f(z_i)$, $(i = 1, \cdots, N)$, are known then the coefficients f_k corresponding to a least-squares

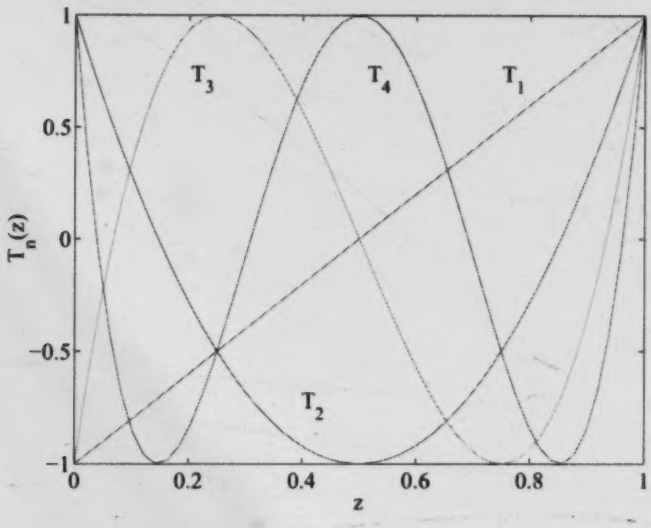

Figure A.1: Shifted Chebyshev polynomials (type I) with $n = 1$ to 4.

approximation of the function $f(z)$ can be found through the solution of the equation

$$\underline{\mathbf{A}}\mathbf{f} = \mathbf{a}, \tag{A.10}$$

where $\underline{\mathbf{A}}$ is a $n \times n$ matrix and $\mathbf{f}$ and $\mathbf{a}$ are both column vectors of length n. The vector length n corresponds to the number of polynomials used to represent $f(z)$. If $n = N$ the series is an interpolation polynomial whereas if $n < N$ then a smoothing polynomial is obtained. The elements of the matrices in (A.10) are defined as

$$\underline{\mathbf{A}}_{lk} = \sum_{i=1}^{N} T_{l-1}(z_i) T_{k-1}(z_i) \tag{A.11}$$

and

$$\mathbf{a}_l = \sum_{i=1}^{N} T_{l-1} f(z_i). \tag{A.12}$$

The coefficients can then be found using the least-squares approximation

$$\mathbf{f} = (\underline{\mathbf{A}}'\underline{\mathbf{A}})^{-1}\underline{\mathbf{A}}'\mathbf{a}. \tag{A.13}$$

Appendix B

Generating Random Numbers with a Cauchy Distribution

A Cauchy-like distribution of can be described by the function

$$P(x) \propto \frac{T}{\sqrt{x^2 + T^2}} \tag{B.1}$$

where T is the temperature parameter that controls the width of the distribution. A cumulative distribution over the interval [a,b] for any probability function can be defined as

$$C(x) = \frac{\int_a^x P(x')dx'}{\int_a^b P(x')dx'} \tag{B.2}$$

(Gould and Tobochnik, 1996). For the Cauchy-like distribution this becomes:

$$C(x) = \frac{\sinh^{-1}\left(\frac{x}{T}\right) - \sinh^{-1}\left(\frac{a}{T}\right)}{\sinh^{-1}\left(\frac{b}{T}\right) - \sinh^{-1}\left(\frac{a}{T}\right)} \tag{B.3}$$

A random number y within the interval [0,1] is chosen from a uniform distribution. This random number y can then be taken as the value of $C(x)$ and the corresponding random number from a Cauchy distribution over the interval [a,b] can be found by solving (B.3) for x. The final result is

$$x = T \sinh\left[y\left(\sinh^{-1}\left(\frac{b}{T}\right) - \sinh^{-1}\left(\frac{a}{T}\right)\right) + \sinh^{-1}\left(\frac{a}{T}\right)\right]. \tag{B.4}$$

Appendix C

Code

C.1 Forward modelling code

```
function D=abozena_mv(alphavec,betavec,rhovec,dvec,c,f)

%D=abozena_mv(alphavec,betavec,rhovec,dvec,c,f)
%
%Program to calculate a dispersion function for Rayleigh
%waves using the Abo-Zena (1979) matrix method that has
%no frequency limitations.  Dispersion curves can be found
%through the roots of the dispersion function.
%This version incorporates the ideas of Menke, 1979
%
%A geology of homogeneous, isotropic flat layers is assumed.
%
%INPUT
%alphavec = vector of P-wave velocities
%betavec = vector of S-wave velocities
%rhovec = vector of densities
%dvec = vector of layer thicknesses - last element is Inf
%c = Rayleigh wave phase velocity
%f = frequency (Hz) (may be a vector)
```

```
%
%OUTPUT
%D = dispersion function value at (c,f) (will be a vector if f is)
%
%Based on: Abo-Zena, A. (1979) Dispersion function computations
%for unlimited frequency values. Geophysical Journal of the
%Royal Astronomical Society, 58: 91-105.
%
%Menke, W. (1979) Comment on 'Dispersion function computations
%for unlimited frequency values' by Anas Abo-Zena. Geophysical
%Journal of the Royal Astronomical Society. 59: 315-323.
%
%written by K.S. Beaty May 3, 2000
%last modified June 8, 2000

EPSILON=1e-12;
k=2*pi*f/c;

r_alph=sqrt(1-(c./alphavec).^2); %complex vector
r_beta=sqrt(1-(c./betavec).^2); %complex vector
ub=find(abs(r_beta)==0); %to avoid divide by zero errors
ua=find(abs(r_alph)==0);
if ~isempty(ua) | ~isempty(ub)
 c=c-EPSILON;
 r_alph=sqrt(1-(c./alphavec).^2); %complex vector
 r_beta=sqrt(1-(c./betavec).^2); %complex vector
end
gamma=2*(betavec./c).^2; %vector
n=length(betavec); %number of layers where layer n is a half-space

%E value for the nth layer
E=setup_En(gamma(n),rhovec(n),r_alph(n),r_beta(n),length(f));
```

```
for m=n-1:-1:1
 %obtain E_n-1 from (41) ...
 E=setup_Em(E,gamma(m),rhovec(m),r_alph(m),r_beta(m),k,dvec(m));
end %for

%last E value from this loop is E_1
%dispersion function value is element 5 of E

D=E(5,:); %value of dispersion function for (c,f)

%%%%%%%%%%%%%%%%%%%%%%%%%%%%%%%%%%%%%%%%%%%%%%%%%%%%%%%%%%%%%%%%%%%%%%%
function En=setup_En(gamma,rho,r_a,r_b,nfreq)

%function to set up the value of E in the nth layer (infinite half-space)
%all input parameters are single values
%r_a and r_b may be complex

En=zeros(5,nfreq);
En(5,:)=gamma^2-((gamma-1)^2)/(r_a*r_b);
En(4,:)=-1/(rho*r_b);
En(3,:)=-(gamma-1)/(rho*r_a*r_b)+gamma/rho;
En(2,:)=1/(rho*r_a);
En(1,:)=1/rho^2-1/(rho^2*r_a*r_b);

%%%%%%%%%%%%%%%%%%%%%%%%%%%%%%%%%%%%%%%%%%%%%%%%%%%%%%%%%%%%%%%%%%%%%%%
function Em=setup_Em(Elast,gamma,rho,r_a,r_b,k,d)

%function to set up the value of E in the mth layer where m not= n
%all input parameters are single values
%r_a and r_b may be complex
%Em coming in is the E value for the layer below the mth layer (m+1)
%all matrices defined herein are 5x5
%E itself is 5x1
```

```
%k may be a vector
%all other input parameters are scalars

P=exp(r_a*k*d);
P=[P;P;P;P;P];
Q=exp(r_b*k*d);
Q=[Q;Q;Q;Q;Q];

%matrices needed as defined in appendix of paper by Menke
g=gamma*(gamma-1);
h=(gamma-1)/rho;
m=gamma/rho;
n=1/rho^2;
p=(2*gamma-1);
s=rho*gamma*(gamma-1)^2;
t=rho*gamma^2*(gamma-1);

M1=4*[-2*g,0,2*h+2*m,0,-2*n;...
      0,0,0,0,0;...
      -s-t,0,p^2,0,-h-m;...
      0,0,0,0,0;...
      -2*g^2/n,0,2*s+2*t,0,-2*g];

a1=(gamma-1)/r_a;
a2=(gamma-1)/r_b;
b1=gamma*r_a;
b2=gamma*r_b;
c1=r_a/rho;
c2=r_b/rho;
d1=1/(rho*r_a);
d2=1/(rho*r_b);
e1=rho*gamma^2*r_a;
e2=rho*gamma^2*r_b;
```

```
f1=rho*(gamma-1)^2/r_a;
f2=rho*(gamma-1)^2/r_b;

M2=zeros(5,5); M3=M2; M4=M2; M5=M2;

%define M2
M2(1,1)=1-(-a1+b2)*(+b1-a2);
M2(1,2)=(-c1+d2);
M2(1,3)=-(+b1-a2)*(+d1-c2)-(-a1+b2)*(-c1+d2);
M2(1,4)=-(+d1-c2);
M2(1,5)=-(-c1+d2)*(+d1-c2);

M2(2,1)=(-f1+e2);
M2(2,2)=1;
M2(2,3)=2*(+a1-b2);
M2(2,4)=-(+a1-b2)^2-(-f1+e2)*(+d1-c2);
M2(2,5)=-(+d1-c2);

M2(3,1)=-(+e1-f2)*(-a1+b2);
M2(3,2)=(-b1+a2);
M2(3,3)=1-(+e1-f2)*(+d1-c2)-(-a1+b2)*(-b1+a2);
M2(3,4)=(-a1+b2);
M2(3,5)=-(-b1+a2)*(+d1-c2);

M2(4,1)=-(+e1-f2);
M2(4,2)=-(+b1-a2)^2-(+e1-f2)*(-c1+d2);
M2(4,3)=2*(+b1-a2);
M2(4,4)=1;
M2(4,5)=(-c1+d2);

M2(5,1)=-(+e1-f2)*(-f1+e2);
M2(5,2)=-(+e1-f2);
M2(5,3)=-(+e1-f2)*(+a1-b2)-(-f1+e2)*(-b1+a2);
```

```
M2(5,4)=(-f1+e2);
M2(5,5)=1-(-b1+a2)*(+a1-b2);

%define M3
M3(1,1)=1-(-a1-b2)*(+b1+a2);
M3(1,2)=(-c1-d2);
M3(1,3)=-(+b1+a2)*(+d1+c2)-(-a1-b2)*(-c1-d2);
M3(1,4)=-(+d1+c2);
M3(1,5)=-(-c1-d2)*(+d1+c2);

M3(2,1)=(-f1-e2);
M3(2,2)=1;
M3(2,3)=2*(+a1+b2);
M3(2,4)=-(+a1+b2)^2-(-f1-e2)*(+d1+c2);
M3(2,5)=-(+d1+c2);

M3(3,1)=-(+e1+f2)*(-a1-b2);
M3(3,2)=(-b1-a2);
M3(3,3)=1-(+e1+f2)*(+d1+c2)-(-a1-b2)*(-b1-a2);
M3(3,4)=(-a1-b2);
M3(3,5)=-(-b1-a2)*(+d1+c2);

M3(4,1)=-(+e1+f2);
M3(4,2)=-(+b1+a2)^2-(+e1+f2)*(-c1-d2);
M3(4,3)=2*(+b1+a2);
M3(4,4)=1;
M3(4,5)=(-c1-d2);

M3(5,1)=-(+e1+f2)*(-f1-e2);
M3(5,2)=-(+e1+f2);
M3(5,3)=-(+e1+f2)*(+a1+b2)-(-f1-e2)*(-b1-a2);
M3(5,4)=(-f1-e2);
M3(5,5)=1-(-b1-a2)*(+a1+b2);
```

```
%define M4
M4(1,1)=1-(+a1+b2)*(-b1-a2);
M4(1,2)=(+c1+d2);
M4(1,3)=-(-b1-a2)*(-d1-c2)-(+a1+b2)*(+c1+d2);
M4(1,4)=-(-d1-c2);
M4(1,5)=-(+c1+d2)*(-d1-c2);

M4(2,1)=(+f1+e2);
M4(2,2)=1;
M4(2,3)=2*(-a1-b2);
M4(2,4)=-(+a1+b2)^2-(+f1+e2)*(-d1-c2);
M4(2,5)=-(-d1-c2);

M4(3,1)=-(-e1-f2)*(+a1+b2);
M4(3,2)=(+b1+a2);
M4(3,3)=1-(-e1-f2)*(-d1-c2)-(+a1+b2)*(+b1+a2);
M4(3,4)=(+a1+b2);
M4(3,5)=-(+b1+a2)*(-d1-c2);

M4(4,1)=-(-e1-f2);
M4(4,2)=-(+b1+a2)^2-(-e1-f2)*(+c1+d2);
M4(4,3)=2*(-b1-a2);
M4(4,4)=1;
M4(4,5)=(+c1+d2);

M4(5,1)=-(-e1-f2)*(+f1+e2);
M4(5,2)=-(-e1-f2);
M4(5,3)=-(-e1-f2)*(-a1-b2)-(+f1+e2)*(+b1+a2);
M4(5,4)=(+f1+e2);
M4(5,5)=1-(+b1+a2)*(-a1-b2);

%define M5
```

```
M5(1,1)=1-(+a1-b2)*(-b1+a2);
M5(1,2)=(+c1-d2);
M5(1,3)=-(-b1+a2)*(-d1+c2)-(+a1-b2)*(+c1-d2);
M5(1,4)=-(-d1+c2);
M5(1,5)=-(+c1-d2)*(-d1+c2);

M5(2,1)=(+f1-e2);
M5(2,2)=1;
M5(2,3)=2*(-a1+b2);
M5(2,4)=-(+a1-b2)^2-(+f1-e2)*(-d1+c2);
M5(2,5)=-(-d1+c2);

M5(3,1)=-(-e1+f2)*(+a1-b2);
M5(3,2)=(+b1-a2);
M5(3,3)=1-(-e1+f2)*(-d1+c2)-(+a1-b2)*(+b1-a2);
M5(3,4)=(+a1-b2);
M5(3,5)=-(+b1-a2)*(-d1+c2);

M5(4,1)=-(-e1+f2);
M5(4,2)=-(+b1-a2)^2-(-e1+f2)*(+c1-d2);
M5(4,3)=2*(-b1+a2);
M5(4,4)=1;
M5(4,5)=(+c1-d2);

M5(5,1)=-(-e1+f2)*(+f1-e2);
M5(5,2)=-(-e1+f2);
M5(5,3)=-(-e1+f2)*(-a1+b2)-(+f1-e2)*(+b1-a2);
M5(5,4)=(+f1-e2);
M5(5,5)=1-(+b1-a2)*(-a1+b2);

Em=M1*Elast + (1./(P.*Q)).*(M2*Elast) + (Q./P).*(M3*Elast) + ...
   (P./Q).*(M4*Elast) + (P.*Q).*(M5*Elast);
Em=Em/4; %now this matches Em from equation (A3)
```

```
return
%%%%%%%%%%%%%%%%%%%%%%%%%%%%%%%%%%%%%%%%%%%%%%%%%%%%%%%%%%%%%%%%%%%%%%%%
```

C.2 Simulated annealing algorithm

```
function sa_inv(m_0,outfile,get_misfit,choose_model,T_schedule,converge,seed)

%sa_inv(m_0,outfile,get_misfit,choose_model,T_schedule,converge)
%sa_inv(m_0,outfile,get_misfit,choose_model,T_schedule,converge,seed)
%
%This function performs an iversion using a simulated anealing
%method (Sen and Stoffa, 1995).  This code follows the Metropolis
%algorithm but can be used to perform fast simulated annealing if
%the model paramters are chosen from random numbers following a
%Cauchy-like distribution instead of a uniform distribution.
%
%This function is flexible in that it can be used with any
%forward model with any number of arbitrary parameters.  The
%content of the model, m, does not matter at all to the main
%program as long as it is compatable with both the function
%that determines the misfit and the function that is used to
%choose new models.
%
%
%INPUT
%m_0 - variable containing initial choices for all model parameters
%get_misfit - name of function that will evaluate the forward model
%            for model parameters, m, and return the model misfit
%choose_model - function that chooses the model from a Cauchy distribution
%              given the previous model and the temperatur, T, and
%              returns a new model, m_new
%T_schedule - cooling schedule; column 1 is temperature, 2 is number of
%            iterations to stay at that temperature for.
```

```
%              If models are taken from a uniform distribution then
%              the cooling rate should not exceed To/ln(k) where
%              To is the initial temperature and k is the number of
%              iterations.  For fast simulated annealin the cooling rate
%              should not exceed To/k.
%converge - number of iterations misfit should stay the same for convergence
%seed - optional variable to set seed of random number generator
%       the default if a seed is not specified is to reset the generator
%       to its initial state (rand('state',0);)
%
%OUTPUT
%everything is written to file OUTFILE
%every 1000 iterations the current model will be saved in a
%file OUTFILE_nk where n is the number of thousands of iterations
%
%written by K.S. Beaty May 14, 2000
%last modified July 12, 2000

%%%%%%%%%%%%%%%%%%%%%%%% Main program %%%%%%%%%%%%%%%%%%%%%%%%%%%%
rand('state',0); %reset random number generator
if nargin==7,
 %set random number generator state to specified SEED
 rand('state',seed); %uses Matlab5 random number generator
end
count=0; tic;
acc_count=0;
rej_count=0; %count number of accepted and rejected models
stop_count=0; %counter to monitor when dE has stopped changing

[E,m_0]=feval(get_misfit,m_0);
m=m_0;
m_min=m_0;
E_vec=E;
```

```
min_E=E;

for t_ind=1:size(T_schedule,1)
  T=T_schedule(t_ind,1);
  for iter=1:T_schedule(t_ind,2)
    count=count+1;
    [m_new]=feval(choose_model,m,T); %evaluate function that chooses model
    [E_new,m_new]=feval(get_misfit,m_new); %evaluate function that gets misfit
    dE=E_new-E_vec(count);
    if dE<=0 %acccept models that improve misfit
       m=m_new;
       E_vec=[E_vec;E_new];
       acc_count=acc_count+1;
       if E_new<min_E
          min_E=E_new;
          m_min=m_new;
       end
    else %acccept models that worsen misfit with temperature-dependent prob.
       P=exp(-dE/T);
       r=rand(1);
       if P>r %accept model
        m=m_new;
        E_vec=[E_vec;E_new];
        acc_count=acc_count+1;
       else %reject model
          E_vec=[E_vec;E_vec(count)];
          rej_count=rej_count+1;
       end %if/else
    end %if/else
    dE=E_vec(count+1)-E_vec(count);
    if (abs(dE)<eps) & (E_vec(count+1)<=min_E)
       stop_count=stop_count+1;
       if stop_count==converge
```

```
            break;
          end %if
        else
          stop_count=0;
        end %if/else
        if rem(count,1000)==0 %save parameters after 1000, 2000, etc. iter.
         eval(['save ',outfile,'_',num2str(round(count/1000)),'k']);
        end %if
        etime=toc;
      end %loop over iterations
      eval(['save ',outfile]);
      if stop_count==converge
        break;
      end %if
    end %loop over temperatures

%%%%%%%%%%%%%%%%%%%%%%%% Summarize results %%%%%%%%%%%%%%%%%%%%%%%%%%%%%%%%

disp(['Total number of iterations: ',num2str(count)]);
disp(['Number of models accepted: ',num2str(acc_count)]);
disp(['Number of models rejected: ',num2str(rej_count)]);
disp(['Number of consecutive matched misifts: ',num2str(stop_count)]);
disp(['Elapse time: ',num2str(etime),' seconds']);
disp(['Final model misfit: ',num2str(E_vec(length(E_vec)))]);
plot(E_vec); title('Model Misfit vs. Number of Iterations');

%%%%%%%%%%%%%%%%%%%%%%%%%%%%%%%%%%%%%%%%%%%%%%%%%%%%%%%%%%%%%%%%%%%%%%%%%%%
```

C.3 Chebyshev polynomials

Generate velocity profile from Chebyshev polynomials:

```
function [v]=cheb_for(z,coef)
```

```
%[v]=cheb_for(z,coef)
%
%function to generate v(z) profile from Chebyshev polynomials
%
%INPUT
%z = depth vector, normalized by the deepest depth (0<=z<=1)
%coef = coeficients of the polynomials
%
%OUTPUT
%v = velocity values corresponding to depth, z
%
%written by K.S. Beaty May 14, 2000
%last modified May 14, 2000

npts=length(z);
Lv=length(coef);
T=zeros(npts,Lv);
T(:,1)=1;
T(:,2)=2*(z-1/2);
for i=2:Lv-1
 T(:,i+1)=4*(z-1/2).*T(:,i)-T(:,i-1);
end
v=zeros(npts,1);
for k=1:Lv
 v=v+coef(k)*T(:,k);
end
```

Fit Chebyshev polynomials to data:

```
function [coef,T]=cheb_inv(z,v,Lv,mu)

%[coef,T]=cheb_inv(z,v,Lv,mu)
%
%function to generate chebyshev polynomials from a v(z) profile
```

```
%
%INPUT
%z = depth vector, normalized by the deepest depth (0<=z<=1)
%v = velocity values corresponding to depth, z
%Lv = number of polynomials to use
%mu = pre-whitening factor (e.g. 0.0001)
%
%OUTPUT
%coef = coeficients of the polynomials
%T = matrix of polynomials.  Columns hold T_{l-1} and rows correspond to z_i
%
%written by K.S. Beaty May 14, 2000
%last modified May 14, 2000

nlayers=length(v);
z=z(:);

T=zeros(nlayers,Lv);
T(:,1)=1;
T(:,2)=2*(z-1/2);
for i=2:Lv-1
 T(:,i+1)=4*(z-1/2).*T(:,i)-T(:,i-1);
end

A=zeros(Lv,Lv);
a=zeros(Lv,1);
for l=1:Lv
 for k=1:Lv
  A(l,k)=sum(T(:,l).*T(:,k));
 end
end
for l=1:Lv
 a(l)=sum(T(:,l).*v(:));
```

```
end
MATRIX=A*A'; %'
coef=inv(MATRIX+mu*trace(MATRIX)*eye(Lv))*A'*a; %'
```